Achieving Energy Self-Sufficiency for the Oostbrug

Integrating Renewable Sources with Thermal Storage for a Balanced Grid

Master Thesis

Annemijn van Schooneveld

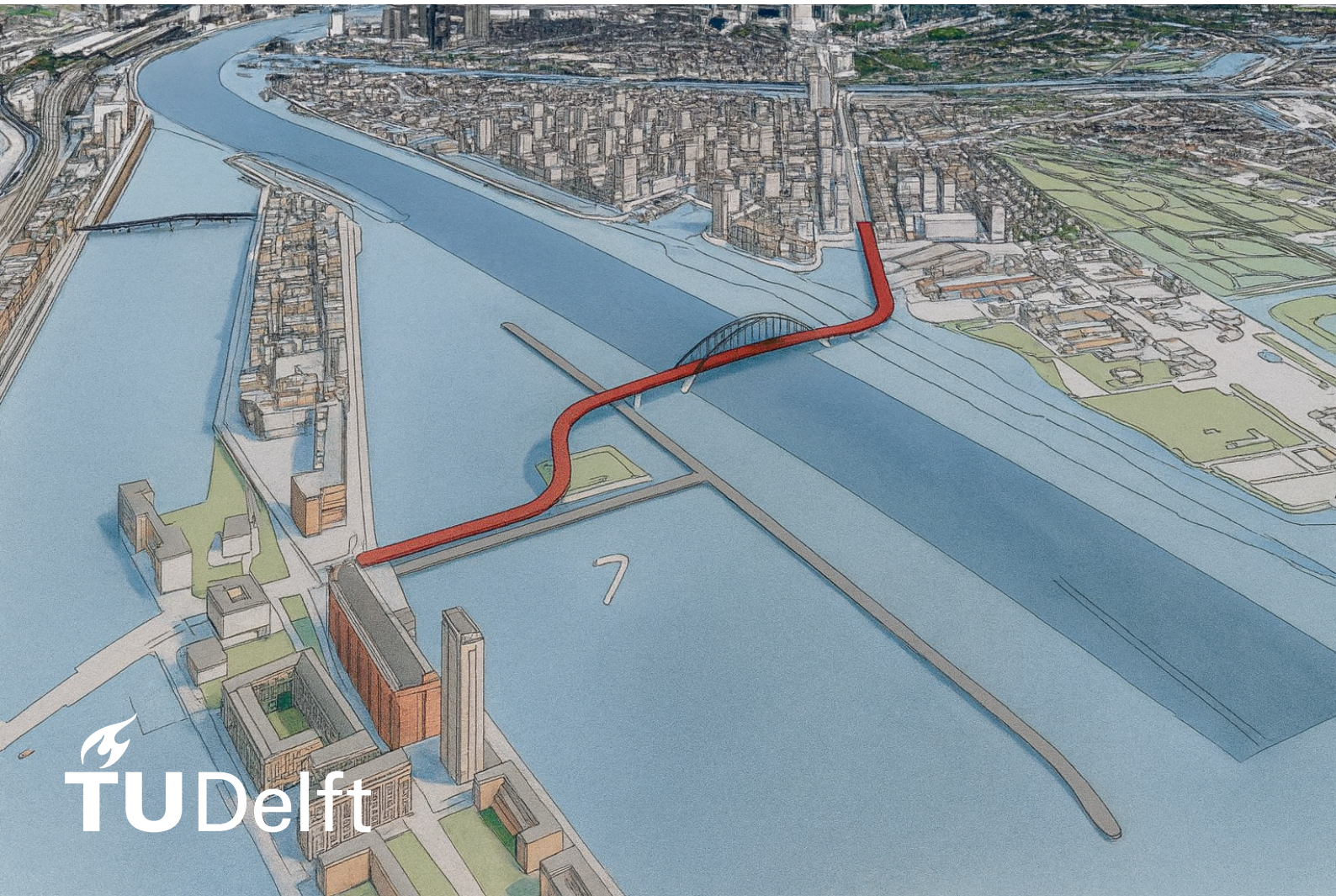

TU Delft

Achieving Energy Self-Sufficiency for the Oostbrug

Integrating Renewable Sources with Thermal Storage for a Balanced Grid

by

Annemijn van Schooneveld

Student Number:	4884477	
Supervisors:	Dr.ir. JM (Martin) Bloemendal	TU Delft
	Prof.dr. PJ (Phil) Vardon	TU Delft
	Paul Geerts	Gemeente Amsterdam
	Victor Nugter	Gemeente Amsterdam
Project Duration:	March, 2025 - November, 2025	
Faculty:	Faculty of Electrical Engineering, Mathematics and Computer Science	Delft, The Netherlands
Master:	Sustainable Energy Technology	
Track:	Heating and Cooling	

Cover:	The Oostbrug by Royal Haskoning
Style:	TU Delft Report Style

TU Delft

Preface

This thesis is written for the Technical University of Delft, the municipality of Amsterdam, and is my academic achievement to fulfill my master's thesis requirements. Back in 2024 Mimi Eelman from the City of Amsterdam sparked my interest during a lecture while she was talking about Amsterdam's energy transition plans. She mentioned the plans for the Oostbrug over the IJ river in Amsterdam Noord and the possible sustainable integrations for this future iconic infrastructural project. This large-scale project gained my interest, combining two backgrounds, since my bachelor's degree is in Civil Engineering, and my current track for my master's is in the heating and cooling department of Sustainable Energy Technology from the TU Delft.

While this bridge is of considerable size, it was sometimes challenging; however, overall it kept me motivated to think outside the box. Due to its size, I was eager to create momentum for the development of sustainable energy sources on the bridge itself, which will be explained in this report.

I would like to thank my supervisors, Martin Bloemendal and Phil Vardon, for their professional and kind supervision. Your skilled expertise in this field, including underground thermal energy storage and geothermal energy applications, greatly contributed to the success of this study. Your great knowledge kept me critical and motivated. From the City of Amsterdam I would like to thank Paul Geerts, who is my first supervisor from the municipality, and my team member from the department 'Energie voor in de Stad'. Victor Nugter, sustainable contract manager from the Oostbrug team, was able to keep me in the loop on all the progress phases from the Oostbrug. Both made me feel very welcome in Amsterdam.

Writing my thesis not only helped me to gather and process information, but also showed me that I can keep going and do more than I first thought possible.

Annemijn van Schooneveld
Delft, October 2025

Abstract

As Amsterdam moves toward its 2040 carbon-neutral and 2050 renewable-heating targets, infrastructure must increasingly support the city's energy transition. The Oostbrug, a planned cycling and pedestrian bridge across the IJ River, provides an opportunity to demonstrate an energy-autonomous bridge concept. Its combined electrical and thermal loads for lighting, operation, and winter de-icing are traditionally supplied by grid electricity and salt spreading. Integrating renewable energy sources with hydronic bridge-deck heating can reduce grid dependence, eliminate salt use, and enhance the bridge's sustainability.

This thesis investigates the feasibility of a self-sufficient bridge energy system combining solar, wind, and thermal sources with on-site battery storage. Five configurations were modeled: three direct heating systems using energy piles or aquathermal heat pumps, and two indirect systems with Aquifer Thermal Energy Storage (ATES). A MATLAB-based hourly simulation using KNMI 2024 weather data and modeled IJ-water temperatures evaluated energy and peak coverage, embodied CO_2, and battery requirements.

Among the direct systems, only the aquathermal heat-pump configuration (System 3) meets both annual and peak de-icing demands, though it requires substantial battery capacity and is sensitive to cold conditions. ATES-based systems (Systems 4 and 5) achieve full annual coverage with strong winter resilience. System 4, combining aquathermal recharge with ATES, provides the highest energy surplus of 2373 MWh yr^{-1} but with greater complexity and embodied emissions, while System 5, using bridge-deck regeneration, offers a simpler, more material-efficient solution with 1048 MWh yr^{-1} surplus and higher robustness. Both storage-led systems eliminate salt-based de-icing, avoiding 7.9 t CO_2 yr^{-1}, salinization in the IJ river, and deterioration of the bridge construction.

System 5 is identified as the preferred option for full-deck, energy-autonomous operation. The Oostbrug demonstrates how bridges can serve as energy-positive infrastructure, integrating structural, thermal, and electrical systems. Future work should extend model validation across multiple climate years and explore integration with Amsterdam's district heating network.

Contents

List of Figures

List of Tables

Nomenclature

Abbreviations

Abbreviation	Definition
ATES	Aquifer Thermal Energy Storage
COP	Coefficient of Performance
FRPH	Fibre-Reinforced Polymer Honeycomb
GSHP	Ground-Source Heat Pump
HDPE	High-Density Polyethylene
HVAC	Heating, Ventilation and Air Conditioning
IJ	IJ River, Amsterdam
KNMI	Royal Netherlands Meteorological Institute
NAP	Normaal Amsterdams Peil
PV	Photovoltaic
PVNB	Photovoltaic Noise Barrier
RVS	Roestvast Staal (Stainless Steel)
SO	Structuur Ontwerp (Preliminary Design)
VFD	Variable-Frequency Drive
WSHP	Water-Source Heat Pump
GHG	Greenhouse Gas

Symbols

Symbol	Definition	Unit
A	Area	[m^2]
A/V	Area-to-volume ratio	[–]
c	Specific heat capacity of fluid	[J/(kg·K)]
c_a	Volumetric heat capacity of aquifer material	[J/(m^3·K)]
c_w	Volumetric heat capacity of water	[J/(m^3·K)]
D	Diameter	[m]
h	Aquifer layer thickness	[m]
k	Thermal conductivity	[W/(m·K)]
k_c	Thermal conductivity of concrete	[W/(m·K)]
k_s	Thermal conductivity of soil	[W/(m·K)]
L	Well screen length of perforated section	[m]
$\dot{m}$	Mass flow rate	[kg/s]
P	Power	[W]
Q	Energy	[Wh]
R_{th}	Thermal radius of ATES storage	[m]
r_p	Radius of pile	[m]
r_t	Radius of circulation tube	[m]
S	Cross-sectional area of tube	[m^2]
T	Temperature	[°C]
T_{h}	Hot well temperature	[°C]
T_{w}	Warm (colder) well temperature	[°C]
ΔT	Temperature difference (inlet–outlet)	[K]
U	Overall heat transfer coefficient	[W/(m^2·K)]
u	Flow velocity	[m/s]
$u_{\max}$	Maximum permissible flow velocity in aquifer	[m/s]
V	Volume	[m^3]
$\dot{V}$	Volumetric flow rate	[m^3/s]
V_{ATES}	ATES storage volume	[m^3]
ρ	Density	[kg/m^3]
η	Efficiency	[–]

Part I – Context and Literature

1

Introduction

1.1. Case Context: The Oostbrug Project

As Amsterdam transitions to a renewable, gas-free energy system by 2040 and a fully sustainable system for heating and cooling by 2050 [4], aiming for a reduction in dependence on the electrical grid and easing pressure on the local energy network. At the same time, Amsterdam Noord has transformed from an industrial hub into a dynamic urban district. With increasing energy demands and limited space for renewable generation, integrating sustainable practices into infrastructure is crucial, as urban areas offer little available ground for new energy installations, making existing infrastructures valuable sites for sustainable integrations [20]. The Oostbrug, a planned bicycle and pedestrian bridge across the IJ, will extend Amsterdam's cycling ring, linking northern and central districts and, together with the West Bridge, complementing the existing ferry as shown in Figure 1.1. This bridge presents an opportunity to enhance connectivity while exploring how infrastructure can be designed to minimize the bridge's operational energy dependence on grid electricity, an important step given that bridges rely on power for their essential systems during operation.

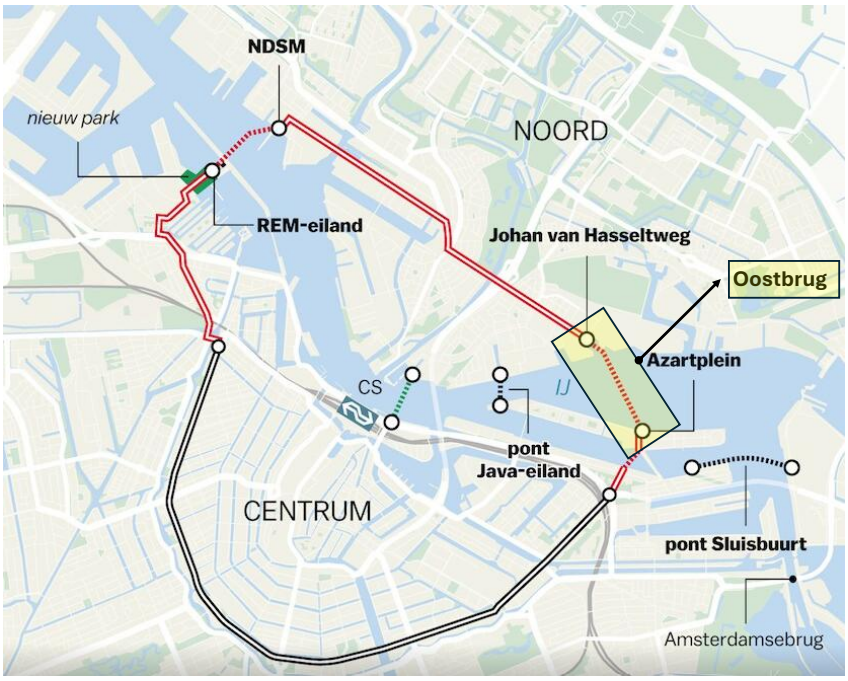

Figure 1.1: Existing ring (black), cycling ring (red), ferries (black dots), bridges (red dots), tunnel (green dots) [2]

Despite Amsterdam's progress toward renewable energy targets, bridges remain largely absent from the city's sustainability agenda [64]. They consume energy for lighting, control systems, and winter operations such as de-icing the bridge deck, yet their potential to generate, store, or exchange renewable energy is underexplored [58]. Most studies [60, 59] focus on indirect geothermal systems (using heat stored seasonally in the ground) for bridge de-icing or direct aquathermal systems (using heat from surface water) for buildings [49]. Meanwhile, direct heating for movable bridges remain scarcely studied. Direct methods require continuous energy without storage, whereas indirect systems offer seasonal flexibility with storage and higher efficiency when paired with renewable energy sources.

Winter maintenance practices further highlight the sustainability challenges of bridge operations. According to the City of Amsterdam, during the winter of 2024–2025, approximately 30 salt-spreading operations were carried out on cycle paths and bridges. Preventive spreading, typically 10–12 g/m² of salt mixed with calcium, is applied under conditions near the dew point to prevent slipperiness. While effective for safety, these practices entail environmental and socio-economic costs, including the embodied CO_2 of salt production (1.53 kg CO_2/kg $CaCl_2$ for processing and transport during the product stage [9]) and the salination risks to the IJ and nearby ecosystems [52]. Besides, the construction's lifetimes will deteriorate under salty conditions. This underlines the need for sustainable, energy-based de-icing alternatives that reduce environmental, ecological, and construction impact.

The goal is to assess the feasibility of a self-sufficient renewable energy system for the Oostbrug, integrating thermal and electrical solutions, which are the primary means of providing heating and power for bridge operation to meet de-icing and operational demands. The study treats the bridge as an integrated energy system, advancing replicable heating and energy concepts for urban crossings.

1.2. Current Sustainable Energy Concepts

A key challenge is the seasonal mismatch between heating and cooling demand, combined with electrical peak demands during operation. This becomes particularly critical for bridge structures, as ice formation during winter can compromise both safety and functionality if not properly managed. The issue is even more pronounced for large structures such as the Oostbrug, where extensive surface areas and exposed components require significant energy input to maintain ice-free conditions.

Salciarini, Lupattelli, and Capati [60] and Revels [59] showed that indirect geothermal systems can de-ice bridges efficiently with minimal structural impact. In summer, asphalt collectors capture solar heat from pavement surfaces, helping to regulate pavement temperature and efficiently extract heat, with performance largely dependent on local weather and system design [13]. This heat can be stored in the ground via the foundation piles by circulating through the bridge deck via fluid-filled loops, reducing dependence on conventional energy sources. Thus, asphalt collectors can be considered both for temperature regulation and energy harvesting. For both electrical and thermal demand, the current understanding suggests that solar panels, as seen in the design of the Cruquius Bridge [56] for bridge operations and geothermal systems utilizing fluid loops in the foundation piles for heating, can provide sustainable energy to meet part of a bridge's energy demand.

While direct aquathermal systems, which use heat directly from surface waters, are rarely applied in bridges, they have proven successful in building applications [39]. The Maastoren in Rotterdam utilizes thermal energy from the Maas River for direct heating and cooling [49]. Besides, the system incorporates a heat storage system and heat pumps to optimize seasonal energy use, serving also as an indirect heating system. This is also seen for the heating network that is under construction on the Ketelhuis WG terrain in Amsterdam. Indirect aquathermal energy will be used, sourcing heat from the nearby canal, combined with storage. In summer, solar-heated surface water is pumped into an aquifer thermal energy storage (ATES) system, where heat is stored in a warm groundwater well approximately 100 metres deep and later recovered during winter through a corresponding cold well. The warm well is heated during wintertime up to 70 degrees with heating pumps [31]. Amsterdam's energy quay wall system, which harvests heat from the city's canals, further illustrates the role of urban water bodies in sustainable energy solutions [12].

1.3. Knowledge Gaps & Scientific Relevance

While this study begins with the integration of thermal energy sources into the Oostbrug's infrastructure, it also considers electrical energy solutions to address the bridge's full energy demand. This research contributes to the existing body of knowledge by assessing how a combination of sustainable energy sources can enhance the year-round energy efficiency of bridge infrastructure, advancing the integration of renewable technologies in urban development.

Most prior work focuses on geothermal energy-pile de-icing on generic bridges or aquathermal energy combined with ATES in buildings. This thesis addresses the fact that bridges remain scarcely evaluated by comparing direct and indirect heating systems supply combined with renewable electricity for the bridge's operational energy demand. It treats the Oostbrug as a single, integrated energy system and compares multiple renewable pathways, leveraging city assets as the IJ river and the subsurface.

This thesis contributes to the field by testing five architectures on a double bascule bridge with consistent hydraulics and operation, generating system-level energy and peak-coverage metrics alongside an embodied CO_2 assessment of heat exchange components. The results inform procurement toward lower-impact options, directly supporting Amsterdam's decarbonisation goals. At the same time, ensuring smoother winter operations improves safety, reduces disruption, and structures' lifetime.

1.4. Aim, Objectives, and Research Questions

The research specifically focuses on direct and indirect, with storage, heat-supply strategies for bridge de-icing. De-icing refers to the process of preventing or removing ice accumulation on bridge surfaces to ensure safe operation. Aiming to evaluate the feasibility of a self-sufficient energy system for the Oostbrug, this study focuses not only on thermal energy and storage but also on integrating renewable electricity to cover de-icing and operational bridge loads. Its objective was to determine whether such a system could reliably reduce dependence on the grid, the central electricity network that supplies power from national or regional utilities, while ensuring operational resilience.

Each of the sub-questions is addressed within the respective chapters of this report, with the answers feeding directly into the overall conclusion on year-round self-sufficiency of the Oostbrug.

Research Question

How can renewable energy sources (solar, wind, and thermal) and storage be combined to achieve year-round self-sufficiency for Oostbrug, balancing intermittent electrical and thermal demand, with the potential to integrate for other bridge infrastructures?

Sub-questions

1. What is the Oostbrug's operational electricity demand?
2. What is the Oostbrug's thermal energy demand profile?
3. How much usable thermal energy can be extracted from the IJ River under seasonal temperature variations?
4. Which renewable electricity sources (solar and wind) are feasible on the bridge based solely on energetic potential?
5. What are the Oostbrug's heating supply, thermal operational electricity load, and required battery storage for a direct heating system?
6. What are the Oostbrug's heating supply, heat storage capacity, thermal operational electricity load, and required battery storage for an indirect heating system?
7. Which system setup and control strategy ensures full energy and peak coverage, and what embodied emissions result from its construction?

1.5. Scope and Structure

The scope of this thesis is limited to renewable energy technologies for meeting the operational bridge and heating loads, with realistic potential for integration at the Oostbrug site itself. The study did not assess the potential for energy generation beyond the bridge's own consumption or contribution to external systems such as the Amsterdam district heating network, which distributes centrally generated heat to buildings for space heating and hot water. Further details on the Amsterdam district heating network are provided in Appendix A. However, if certain systems were to produce a surplus of energy on an annual basis, this surplus could potentially be integrated into district heating networks.

A central theme of this thesis is the distinction between thermal systems delivering heat directly when needed and indirect heating systems, which are storage-based. These systems are compared under common climatic and operational conditions, evaluated for their ability to meet yearly de-icing demands. Deep geothermal energy is excluded, as its heating capacity scale and costs exceed the needs of a single bridge and are more suited for district-level applications. Moreover, long-term management and costs of the systems are also not part of this study

The thesis is structured in three main parts outlined in Figure 1.2 below. Part I establishes the context, identifies knowledge gaps, and reviews theoretical foundations for thermal and electrical energy with Oostbrug's boundary conditions and operational electricity load. Part II opens with Chapter 2, the general methodology, which explains the framework used for the system assessment. The chapter outlines the assessment process, starting with thermal load determination, followed by system inputs and boundary conditions, and describes the assessments of the energy performance evaluations. Chapters 4 and 5, respectively, the direct and indirect heating systems, address their energy performance with corresponding electrical demand. Performance outcomes are in a comparable format for each system. Part III synthesizes these findings into an evaluation and reflection on technical feasibility, integration opportunities, and socio-economic implications, and concludes with recommendations for practice and future research.

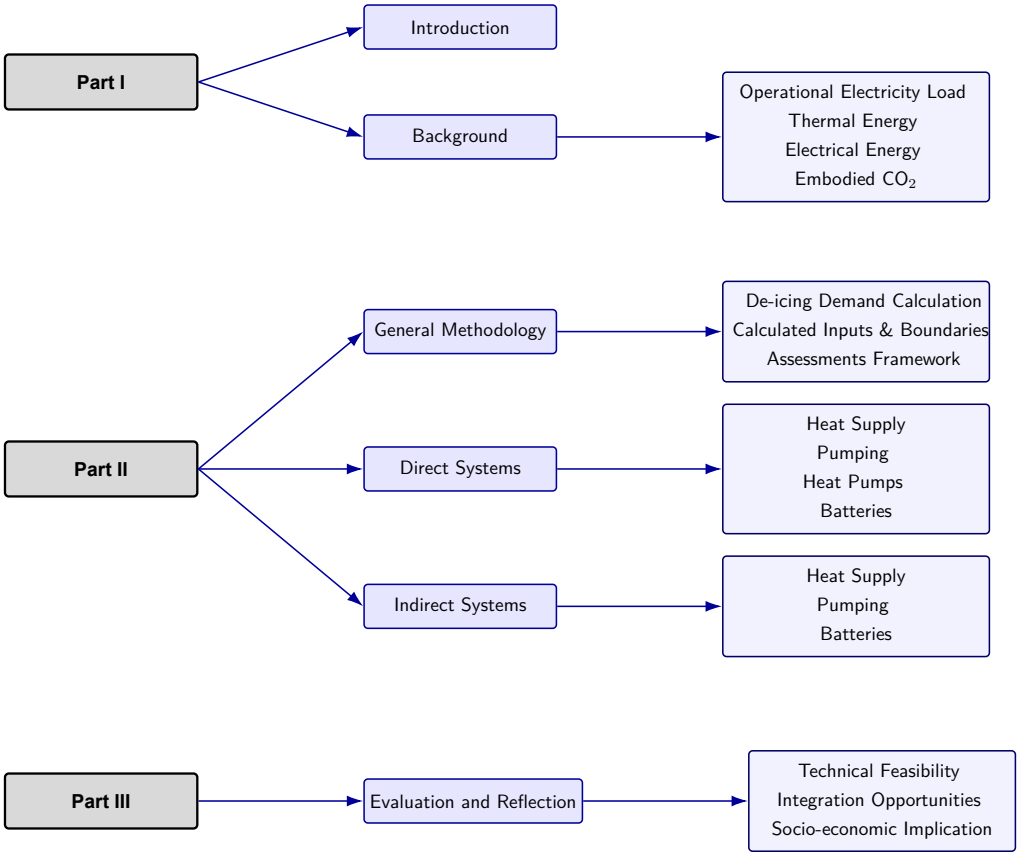

Figure 1.2: Report structure with branching subsections

2

Background

This chapter establishes the input parameters for the Oostbrug and the theoretical foundation for energy system analysis. It defines the physical input and boundary conditions, and both thermal and electrical background information on demand, supply, and storage used in subsequent design evaluations. Section 2.1 describes the bridge geometry, foundation characteristics, and operational parameters, constant throughout the report. Section 2.2 outlines the thermal energy background, including the bridge's heat demand, potential supply sources such as aquathermal and asphalt collectors, and a seasonal storage concept. Section 2.3 covers the electrical energy background, outlining common demand profiles of bridges, renewable supply options, and storage technologies. Finally, Section 2.4 addresses embodied CO_2 emissions of key system components, limited to the product stage only, to assess their environmental impact. Together, these sections define the technical and environmental context for understanding the concepts applied in later chapters. This part addresses:

- *Sub-question 1: What is the Oostbrug's operational electricity demand?*

2.1. Oostbrug Inputs and Boundary Conditions

This section contains the key input parameters and boundary conditions of the Oostbrug, as derived from the Preliminary Design (SO) of Haskoning [34], commissioned by the City of Amsterdam. The sections provide an overview of the bridge geometry and foundation configuration, motion characteristics, and associated deck motion demand, auxiliary electrical loads, and potential energy recovery during operation. Establishing these parameters is essential for the subsequent thermal and energy analyses, as they define the structural, operational, and environmental constraints that determine the feasibility and performance of integrated renewable energy systems for the Oostbrug.

Bridge Geometry and Foundation

Two bridge deck variants are considered in the design by Haskoning [34]. The concrete variant consists of a prefabricated concrete deck with a maximum thickness of 1.5 m, finished with a 5 cm cast asphalt top layer wearing course for surface protection and waterproofing, shown in Figure 2.1a. The steel variant is shown in Figure 2.1b, comprises a 1.5 m steel deck with a 1 cm thin asphalt wearing layer for skid resistance and corrosion protection. Figure 2.1 below illustrates the typical layer composition for both deck types.

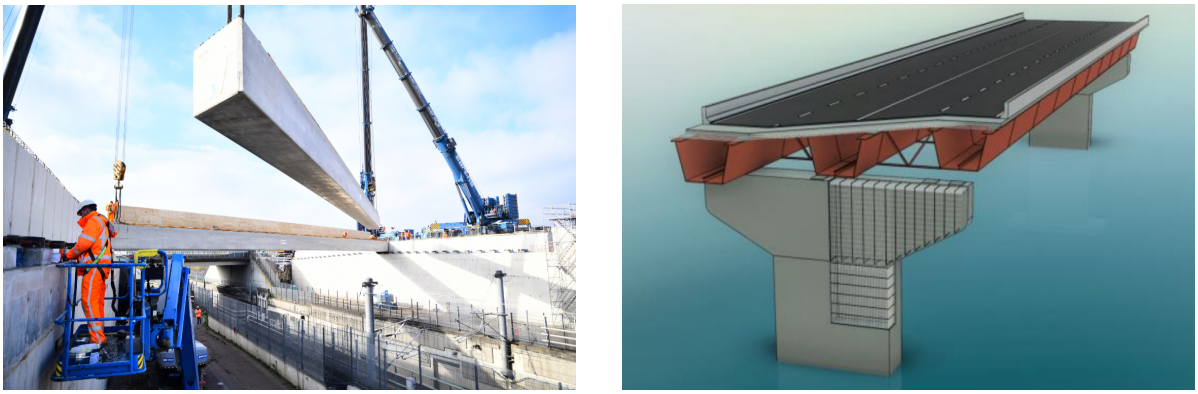

(a) Prefabricated concrete deck **(b)** Steel deck

Figure 2.1: Oostbrug deck layer composition variants [34]

In the draft SO from Haskoning [34], the Oostbrug consists of a double-leaf bascule span, with a total deck length of approximately 1.2 km and a width of 12 m. The structure will be supported by either tubex or prefabricated concrete pillar foundations, respectively, until the 3rd and 2nd sand layers. Both tubex and prefabricated concrete pillars are considered feasible options for these pillars.

The bridge foundations form a crucial part of the potential thermal system, integrating heat-exchange piping. These consist of embedded tube-shaped systems loops through which a fluid circulates to absorb or release heat, enabling thermal energy transfer between the foundation piles and their surroundings, which will be explained in subsection 2.2.2. Two principal foundation configurations are present: the cellar and main pillar groups. The main pillars support the central spans over the main waterway, while the cellar pillars are located at the northern and southern ends of the bridge, 35 meters further than the main pillars.Figure 2.2 illustrate these configurations schematically. The red box indicates the cellar pillars, and the green box shows the main pillars.

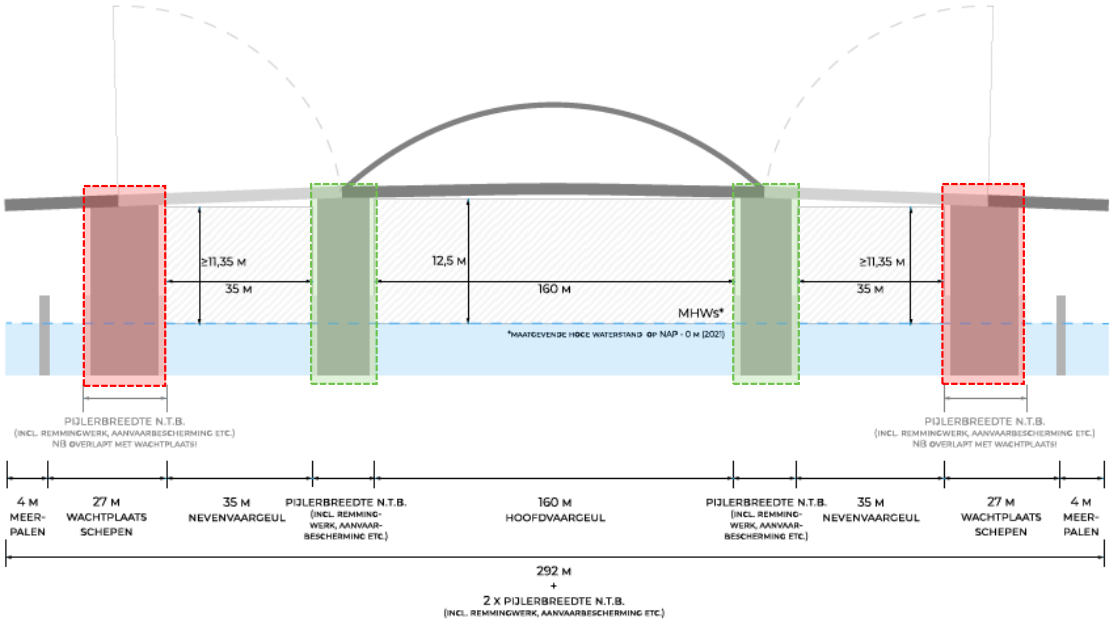

Figure 2.2: Oostbrug side view of main span with cellar (red) and main (green) piers[34]

Bridge Motion

The electricity demand of the bridge deck is determined by the number of yearly openings, the connected drive power, and the duration of movement. Based on the project assumptions, the bridge is operated approximately on an average 5,000 times per year (14 openings per day). The effective energy used during movement is estimated at 30% of the installed drive power, multiplied by the motion time. The wind isn't always strong, and the power varies throughout the movement cycle. In Figure 2.3, the single- and double-leaf bascule bridge types are considered.

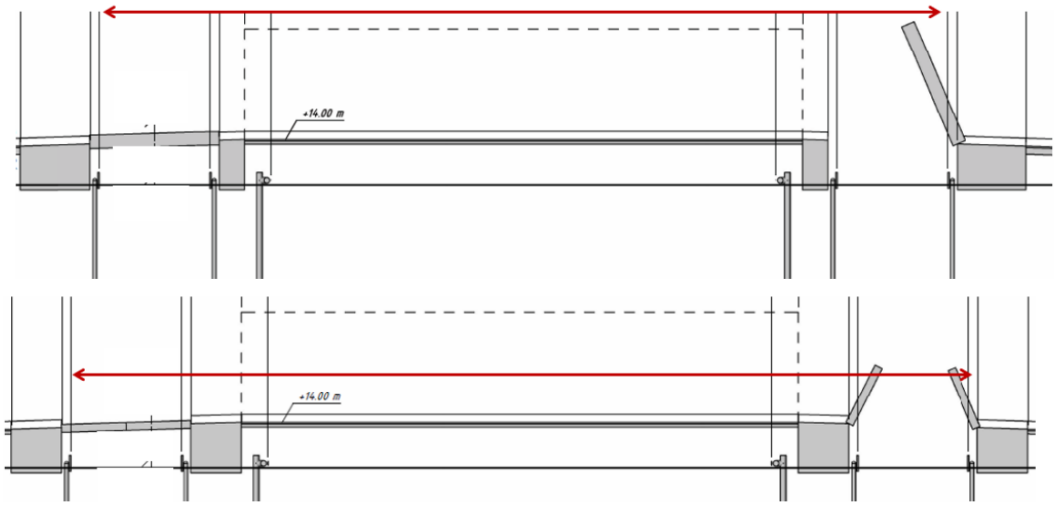

Figure 2.3: Oostbrug one vs. two bridge falls per movable bridge [34]

For a double-leaf bascule bridge (2 $\times$ 20.5 m), the connected drive power is 72 kW, with a motion time of 95 seconds. This results in an average of 0.57 kWh per opening, or about 2.9 MWh per year. For a single-leaf bascule bridge (41 m), the drive power is 135 kW and the motion time is 120 seconds, yielding 1.35 kWh per opening, or about 6.8 MWh per year.

Table 2.1: Annual electricity consumption for deck movement [34]

Bridge type	Drive power (kW)	Motion time (s)	Opening (kWh)	Openings/year	Annual energy (MWh)
Double-leaf (2 $\times$ 20.5 m)	72	95	0.57	5,000	2.9
Single-leaf (41 m)	135	120	1.35	5,000	6.8

In conclusion from Table 2.1, the energy required solely for deck movement is modest compared to total facility consumption, but it is significantly higher for the single-leaf design.

Auxiliary Loads

While the deck movement contributes a measurable share, the majority of the annual electricity consumption comes from auxiliary loads such as lighting, control systems, and heating. These loads are estimated at 50 kVA, with an average yearly duty of 50%, equating to about 219 MWh per year. Deck heating is done by renewable heating solutions, thus not included in the auxiliary electricity loads.

To obtain more precisely the amount of light consumption on the bridge deck, 50 Watts per 25-meter light in general is needed to light the streets. The municipality of Amsterdam has a guideline of requirements for decorative lighting and standard public lighting. A continuous lighting demand of approximately 4,100 operating hours per year is required, without the use of dimming. However, dimming could be preferable for the infrastructure of this scale across the IJ River, since full lighting intensity

comparable to urban street lighting is not strictly necessary. For a bridge length of 1,200 meters, the lighting requirement is 4,800 watts on each side, resulting in a total annual consumption of about 19.7 MWh.

Table 2.2: Annual electricity consumption including auxiliaries [34]

Bridge type	Lighting load (MWh)	Control system (MWh)	Deck motion (MWh)	Total demand (MWh)
Double-leaf (2 $\times$ 20.5 m)	19.7	10.9	2.9	33.5
Single-leaf (41 m)	19.7	10.9	6.8	37.4

From the 219 MWh loads, it is estimated that 5% is part of the control system. Concluding, when lighting and deck motion are added, the total consumption becomes approximately 33.5 MWh for the double-leaf bridge and 37.4 MWh for the single-leaf bridge.

In summary from Table 2.2, deck motion accounts for only about 8–18% of the total annual demand, with lighting load dominating electricity use.

Energy Recovery

During bridge operation, energy can theoretically be regenerated when the bridge is lowered or when braking occurs. However, because a bascule bridge is counterweighted, the net potential energy change over a full cycle is small, and most of the input power covers resistive losses, friction, and dynamic effects [77].

If regenerative variable-frequency drives (VFDs) are used, motor controllers that can recover braking energy and feed it back into the electrical grid when the bridge is lowered [34], and the grid allows energy backfeed, approximately 10–30% of the motion energy could be recovered. This would correspond to 0.3–0.9 MWh per year for the double-leaf bridge and 0.7–2.0 MWh per year for the single-leaf bridge.

Table 2.3: Annual potential electricity regeneration [34]

Bridge type	Motion energy (MWh)	Recoverable fraction (%)	Regeneration (MWh)
Double-leaf (2 $\times$ 20.5 m)	2.9	10–30	0.3–0.9
Single-leaf (41 m)	6.8	10–30	0.7–2.0

2.2. Thermal Energy

For the Oostbrug, thermal energy is used to keep the bridge deck safe and ice-free during winter by circulating heat through the structure. This provides a reliable alternative to salt spreading, which can harm the environment and decrease the lifetime of the bridge deck [75]. In addition, the site offers opportunities to harvest and store renewable heat, reducing dependence on grid electricity. In this context, thermal energy refers to heat that is sustainably generated, stored, and distributed within the bridge.

Amsterdam currently conducts around 30 salt-spreading operations each winter on bridges and cycle paths, a practice that ensures safety but underscores the need for more sustainable alternatives. The options outlined here are selected because they fit the bridge's local conditions: piles for ground exchange, direct access to the IJ for aquathermal use, a large deck surface for solar collection, and nearby aquifers for seasonal storage. This chapter, therefore, examines the heat demand of the deck, the renewable supply options, and the storage systems needed to bridge seasonal gaps, forming the foundation for designing and comparing thermal energy concepts tailored to the Oostbrug.

2.2.1. Demand

Bridge decks cool faster than roads and need reliable de-icing. Heat demand depends not only on weather conditions but also on design factors such as tube spacing, fluid temperature, and wind effects, which determine how much energy must be supplied. This subsection outlines these drivers and how they define the heat required to keep the deck above freezing temperature.

Bridge Deck De-icing

A bridge deck tube system with warm liquid moving through the pipes is a heating source-dependent system that can meet snow-melting requirements. The liquid in the tubes is heated by incident solar radiation, conduction via the concrete, and finally convection due to internal pipe flow as described in Figure 2.4. Spitler and Ramamoorthy [63] states that concrete's high heat capacity stores heat well, while a steel deck might be very conductive but poor in storing heat due to its low heat capacity. Besides, installing tubing on steel decks is difficult and inefficient, whereas concrete decks can easily embed the tubes during casting. This system can be constructed perpendicular to the driving direction, a horizontal layout, or in line with the driving direction, a vertical layout. Both designs are shown in Figure 2.5.

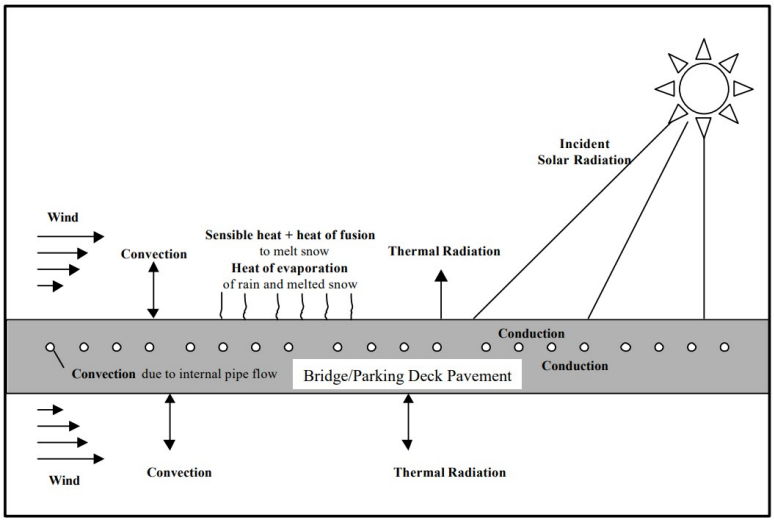

Figure 2.4: Heat-balanced bridge deck tube system [63]

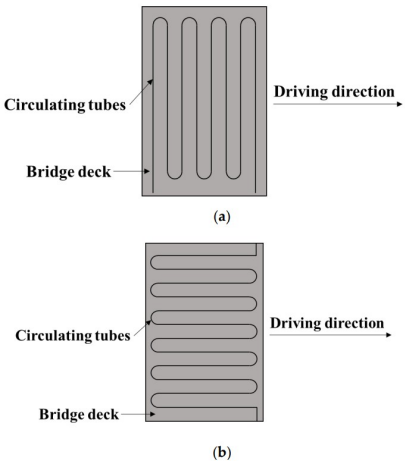

Figure 2.5: Deck tube layouts: (a) horizontal, (b) vertical [43]

The bending areas of the circulating tube perform the worst snow-melting effect. Therefore, the horizontal layout of the circulating tubes is preferred, because the bending areas of the circulating tubes are on both ends of the bridge deck width. While for the vertical layout, the bending areas occur consequently over the whole width [43]. Lyu et al. [43] also concludes that if the outside temperature is -2 °C, snow melting on the bridge deck will still occur with a tube spacing of 25 centimeters and an inlet

temperature of the fluid of 20 °C. With a higher inlet temperature, consequently, more thermal losses develop. Secondly, bigger tube spacing requires more power. The tube spacing has a more significant effect on the required inlet temperature to achieve snow melting than the outside temperature. In combination with a hot bridge deck during the summertime, the system can operate sustainably, as it can continue indefinitely and is replenished naturally with solar thermal energy. Vice versa during wintertime. Furthermore, Spitler and Ramamoorthy [63] shows that whenever a geothermal system is recharged with solar energy during the summertime via the bridge deck, this is a more cost-effective solution compared to no summer recharge.

To further improve heat transfer, conductive concrete compositions in bridge decks can be used as heating systems for de-icing bridge decks. Implementing conductive fibers and particles results in conductive concrete, with the use of electricity as a power source, making de-icing possible, tested by Yehia and Tuan [75]. Conductive concrete is a special type of concrete that can carry electricity through its steel and metallic components in the concrete top deck, allowing it to warm up (due to electrical resistance) and melt ice when power flows through it. It is known to be a cost-effective method, and the fabrication is not without disadvantages. The production comes with specific safety regulations [71]. Additionally, a fiber reinforced polymer honeycomb (FRPH) with a polymer concrete as top layer is investigated by Taylor [67]. Designed to replace the cement binder together with a sand and gravel mixture. Heat transfer occurs mainly by thermal conduction in the polymer concrete, while FRPH conducts 2.5 times slower. A cross-section of the FRPH with the polymer concrete is given in Appendix B.

However, these systems are dependent on electrical power; therefore, it is not applied in this study because the focus of this study lies on energy systems other than de-icing via electricity-powered sources. Additionally, this method can only deliver about one-quarter of the average power output (in W/m² of bridge deck) [75] [67] compared to hydronic tube systems, where warm liquid circulates through embedded pipes.

Building on this principle, hydronically heated bridge decks have been investigated by Lyu et al. [43], who examined various inlet temperatures and tube spacings 6 centimeters below the deck surface to obtain the required power for achieving 95% snow melting in three hours for a concrete bridge deck of 25 centimeters thickness. For this research, a base case parameter of zero wind speed was used; however, in reality, higher wind speeds increase the melting time. Concluding that for every 1 m/s extra wind speed, the melting time increases by approximately 1 hour. The amount of heat absorption power needed to achieve 95% snow melting is given in Equation 2.1. This formula scales linearly with the inner section of the tubes, the flow rate, and the temperature difference:

$$P = c \cdot \rho \cdot S \cdot v \cdot \Delta T \tag{2.1}$$

where c is the specific heat capacity of the heat transfer fluid (J/(kg·K)), ρ its density (kg/m^3), S the inner cross-sectional area of the tubes (m^2), v the flow velocity (m/s), and ΔT the temperature difference between inlet and outlet (K).

With a tube diameter of 0.02 meters, a flow rate of 0.6 m/s in the tubes with 42% propylene glycol, and a research unit of 1 tube per deck length, the optimal inlet temperature is determined while making sure the required absorption power is reached. Glycol lowers water's freezing point, enabling efficient heat transfer at low temperatures [43]. The optimal inlet temperature under different tube spacings and ambient outside temperatures is shown in Figure 2.6. This is for a bridge of 11.25 meters in width, which is close to the 12-meter width of the Oostbrug.

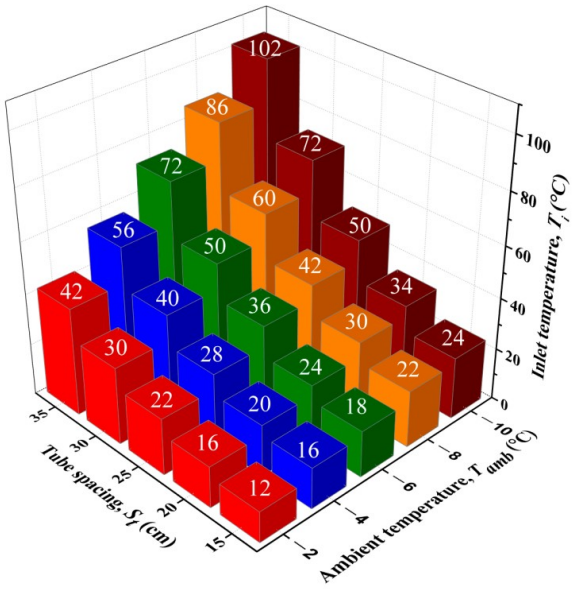

Figure 2.6: Optimal inlet temperature vs. tube spacing and ambient temperature (11.25 m bridge) [43]

During colder seasons, the heating system is fully activated whenever the outside temperature drops to 2°C [48]. While another study [13] shows that for higher outside air temperatures, the heating system is on only part of the time, to ensure the heating is done gradually. This prevents excessive peak load demand; the same total energy input is spread over a longer period, lowering the instantaneous demand on the source and avoiding capacity peaks. The latter study also confirms that while the outside temperature drops to 2°C, the system is almost on for the entire time. Thus, the heated bridge deck section will remain above its freezing point, whereas under freezing ambient conditions of -5 °C, an unheated deck section is similar to this outside air temperature [13].

2.2.2. Supply

Meeting this demand requires renewable sources that can be integrated into the bridge. Options include energy piles exchanging heat with the ground, aquathermal systems using surface water, solar deck collectors, and heat pumps. Each source works differently, with specific advantages and limitations. This subsection introduces these options. Together, these systems offer complementary ways to supply renewable thermal energy for bridge deck de-icing.

Energy Piles

Energy piles are piles equipped with embedded heat-exchange pipes through which a fluid flows, allowing them to store or extract heat from the ground, and can be combined for structural support with a shallow geothermal energy function. Three different types of tube-shaped systems will be evaluated for the energy piles to find the shape that contributes to the highest power output per meter of pile length.

The U-shape is the most straightforward. By doubling this shape, a W-shaped pile foundation is created. Because of this mirroring property, the flow rate through the U-shape is halved for the W-shape in Gao et al. Comparing the absolute flow rates, the thermal performance of the W-shape is almost one and a half times better than the U-shape [29]. However, Han & Yu (2017) considered a third shape [33]. With spiral-shaped pipes, the fluid in the pipe travels a greater distance due to the increased length of the pipe. This foundation performs approximately 2 to 3 times better than the U- and W-shapes. The longer flow path in the spiral shape allows more heat exchange with the soil. All three different shapes are shown in Figure 2.7.

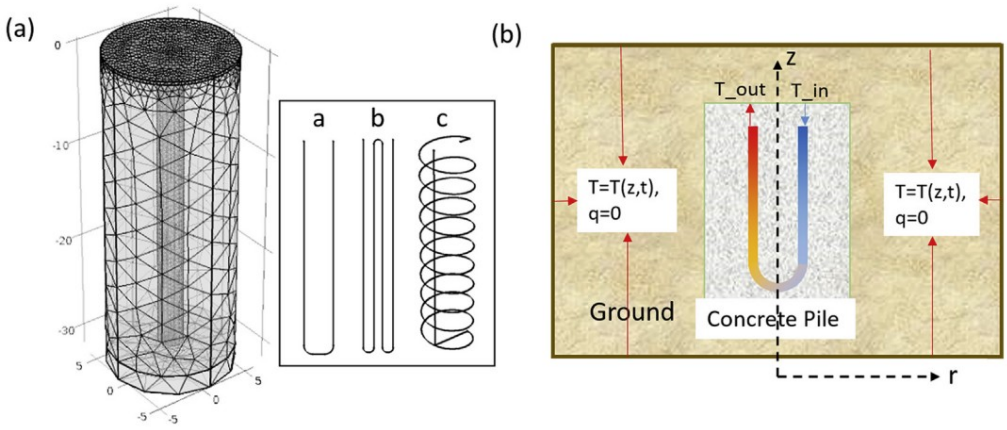

Figure 2.7: Tube geometries (a) U-, W-, spiral-shapes; (b) U-tube boundary conditions [33]

The power output per unit length of an energy pile in the subsurface is determined by soil, pile, and fluid properties. A range of these different properties is given in Figure 2.8. This is provided for a long-term energy supply of 60 days, which is suitable for meeting the required peak demands for this maximum duration. In short, the most important parameters will be named. The thermal conductivity of the soil has a significant influence, as it provides information about how easily heat can transfer through the soil and exchange heat with the fluid circulating in the pipe. On the other hand, while the thermal conductivity of the soil increases, the ability to store heat in the surrounding soil of the pile in the subsurface becomes more difficult because heat dissipates more quickly, decreasing the ground temperature increment near the pile. Secondly, if the temperature difference becomes larger, the power supplied by the energy pile increases. If the difference increases, more heat is extracted at the outlet of the tube [24]. However, it is argued that the ground temperature conditions are of greater importance than the inlet temperature [33]. Finally, another remarkable insight is the radius of the circulation tube. The minimum and maximum value range is close to one another; small changes in this parameter have a significant impact on the power output, ranging from 20 to almost 60 W/m pile length. These parameters have the most significant effect on the long-term thermal operations efficiency, while for the short-term operation, the above-mentioned order is reversed [24].

Figure 2.8 below summarizes which factors most strongly affect heat performance after 60 days of operation. In simple terms, soil properties determine how easily heat can move in and out of the ground, while the fluid and pipe characteristics control how effectively that heat is captured. It shows that soil thermal conductivity is the most influential factor. Even small changes in the tube radius can significantly alter performance, while concrete conductivity and pile radius have smaller effects. Where k_s is the thermal conductivity of the soil (W/(m·K)), $\Delta\theta$ the temperature difference between inlet and outlet (K), r_t the radius of the circulation tube (m), v the fluid circulation velocity (m/s), k_c the thermal conductivity of the concrete (W/(m·K)), and r_p the pile radius (m).

Figure 2.9 illustrates how temperature varies along the depth of one pile between summer (charging) and winter (discharging) [17]. This is shown for a period of four years, starting from May. The lines remain nearly parallel (different with varying depths from P12 to P15), indicating that depth has a minimal effect on stored temperature. This suggests consistent temperature performance over the entire pile length up to 43 meters.

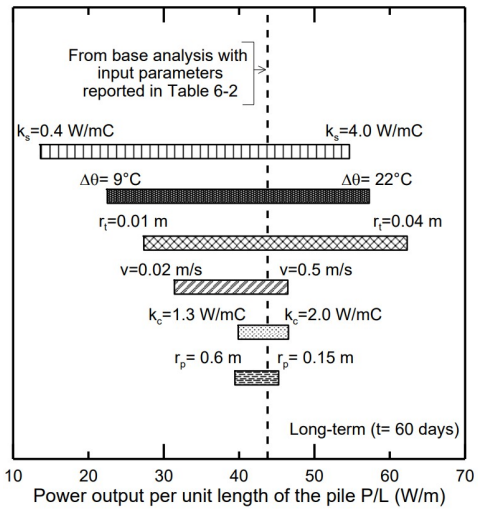

Figure 2.8: Parameter sensitivity on geothermal pile thermal efficiency after 60 days [24]

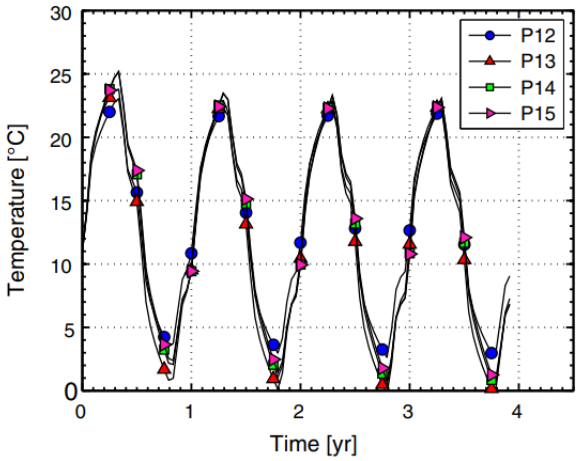

Figure 2.9: Four-year solar-rechared energy pile temperatures from May (depths P12–P15) [17]

Increasing fluid velocity supports the power output of the energy pile, as seen in Figure 2.8. Higher flow rates mean the fluid carries heat away faster, but after a certain point, the extra pumping energy outweighs the benefit. For the spiral-shaped pipes, this has a great influence on the heat exchange, while for the U- and W-shape, the effect is lower [33]. However, until a certain threshold is reached, Thereafter, it influences the heat exchange efficiency not further [29]. While a higher fluid velocity provides faster heat extraction, the heat transfer is still limited by thermal properties. Concluding that with higher flow rates, the improvement rate will flatten, and only pumping energy will increase.

Aquathermal Energy

Aquathermal energy refers to using surface water, such as rivers or canals, as a heat source or sink. Extracting thermal energy from surface water is most efficient with open aquathermal systems, as the water is in direct contact with the heat exchanger under optimal thermal conditions. In contrast, closed systems have less favorable conditions for heat transfer. This water is extracted from the surface water, filtered before it enters the heat exchanger, and thereafter injected back into the surface water. Filtering water is necessary since the water on the top surface can be contaminated with algae growth. The system is widely applicable and has great potential. In addition, thermal energy recovery from wastewater and from drinking water each depends on its respective infrastructure. Moreover, for drinking water systems, the maximum extractable temperature is strictly limited to ensure water quality. Therefore, this thesis focuses on thermal energy from surface water, where water temperature decreases occur more slowly over larger water bodies. [27].

The potential of this technology has been extensively studied in the Netherlands by Fockert and Harezlak [26]. To serve the energy demand in the Netherlands, the potential for thermal energy from surface water is three times bigger than the energy potential from wastewater. The potential from drinking water is the lowest, compared to the two systems mentioned earlier. This was researched and conducted as part of the Deltares Innovation Plan WarmingUP (2022). For that reason, the implementation of thermal energy from surface water occurs more often than in the drinking or wastewater systems.

From surface water, warm and cold thermal energy can be extracted, depending on the required demand, in combination with the surface water temperature. The system can consist of the aquathermal system with a heat exchanger, possible thermal storage, heat pumps, peak supply possibilities, and the heat distribution network. Heat pumps raise the temperature directly from the aquathermal source or storage to the desired level. Furthermore, to ensure the right timing and temperatures, storage helps to deliver the energy demand seasonally. Warm water is extracted from surface water during summer and stored in a seasonal thermal energy storage system. In winter, this stored heat is extracted and delivered to the users, after which the cooled return water is discharged into the cold well. [26]. This will be elaborated on in the next section.

Figure 2.10 compares open and closed aquathermal systems. In both cases, the heat pump upgrades the extracted heat to a usable temperature. Open aquathermal systems pump source water directly into the system, with a pre-filter to prevent fouling, thereafter a fine filter, and an open loop heat exchanger before the water is discharged back. While closed systems keep the source water separate using a closed loop heat exchanger placed in the water body [6]. Open systems are generally more efficient because the water directly contacts the heat exchanger, while closed systems are easier to maintain and avoid contamination.

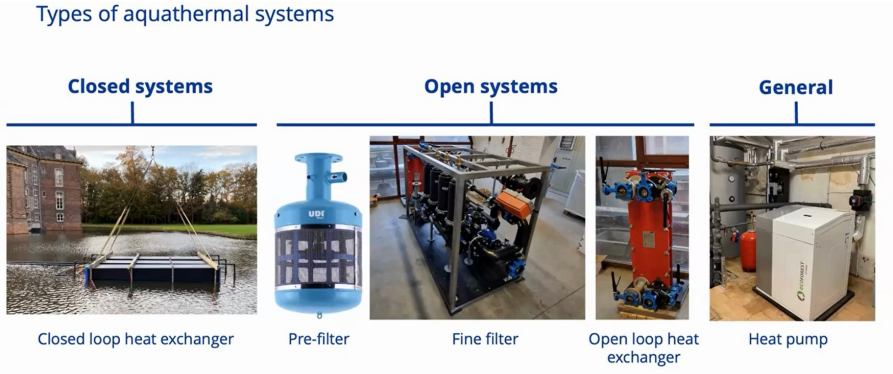

Figure 2.10: Aquathermal systems: closed vs. open configurations and components [6]

Asphalt Collector

Another renewable option is using the bridge deck itself as a solar collector. For both concrete and steel deck variants (Figure 2.1) of the Oostbrug bridge by the draft SO from Haskoning [34], an asphalt layer as a top layer is required. Pipes embedded in the asphalt absorb heat from sunlight during summer and can return it during winter. The solar energy collector efficiency of the bridge deck is approximately 26% to 47% [74]. This is confirmed by Chen et al. (2025), who report an efficiency of asphalt solar collectors of an average of 30 %. Besides, the lifetime of the asphalt can increase by 3 years by lowering the deck temperature [10]. Efficiency mainly depends on how much sunlight hits the surface and how much heat is lost to the surrounding air through wind. Higher solar radiation and lower wind speeds result in a larger temperature difference between the inlet and outlet fluid. Concluding that for these conditions with unchanged fluid properties, the absorbed power of the deck rises.

In Figure 2.11, the thermal power delivered by the asphalt collector during the summer time (energy delivered to the water) is on the positive x-axis. The negative power on the x-axis represents the energy absorbed by the water from the cooler asphalt during winter. On the Y-axis, the number of hours per year during which a certain power density occurs.

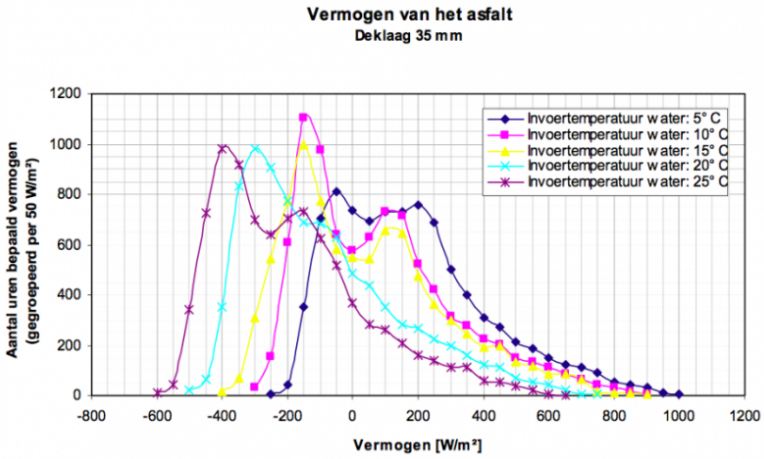

Figure 2.11: Energy balance in asphalt pipe–water exchange [66]

With an inlet temperature of 5 degrees, the curve is on the far right side of the x-axis, showing a stronger heat absorption power by the water per square meter of asphalt, peaking on the positive side of the x-axis [66]. Concluding that lower inlet fluid temperatures result in higher heat absorption from the asphalt. Consequently, pavement temperature drops, radiated heat is reduced, and the heat gain can be used for storage or energy consumption. During winter, the flow direction can be reversed to prevent icing by releasing stored heat back into the deck.

Heat Pumps

This report considers two main heat pump types: ground-source heat pumps (GSHP) and water-source heat pumps (WSHP) that supply power and a temperature increase of the source. Figure 2.12 below compares both systems and shows where the heat is extracted and released. A GSHP extracts heat from the ground through circulating fluid in the boreholes, while a WSHP takes heat from a water body through a plate heat exchanger [45].

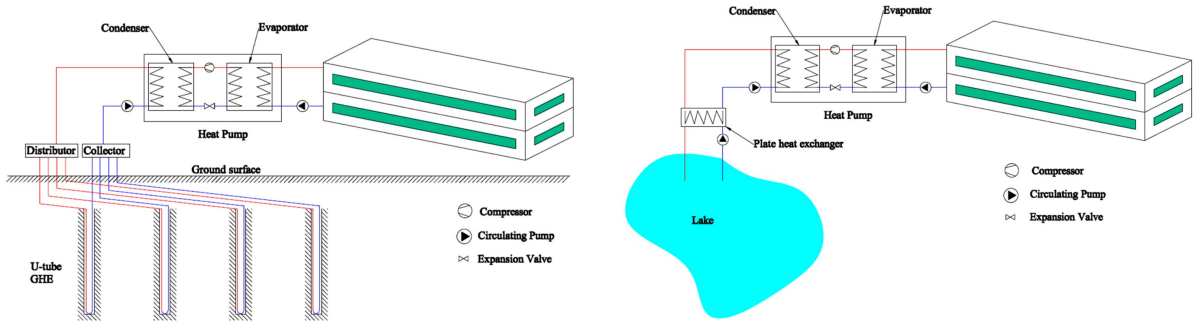

(a) Ground-source heat pump. **(b)** Water-source heat pump.

Figure 2.12: GSHP vs. WSHP from heat extraction to supply [45]

These systems illustrate how low-grade heat can be made available for bridge heating. For the Oostbrug, GSHPs are relevant in the form of energy piles, where the same fluid circulates continuously through the pipes without direct contact with the ground (closed-loop), exchanging thermal energy. Open-loop systems, such as ATES or aquathermal concepts, use groundwater or surface water directly and are often classified as WSHPs. The Coefficient of Performance (COP) describes how much heat is produced for every unit of electricity used. Because the water itself is the source, WSHPs usually achieve slightly higher COPs, providing more stable and higher source temperatures [73]. The choice between GSHP and WSHP therefore depends on site conditions.

All heat pumps operate on the same principle: the pump collects low-temperature heat (evaporator), compresses it to a higher temperature, and releases it where heating is needed (condensor). The expansion valve cools the fluid down so the cycle can start again. The COP is highest when the difference between the source temperature and the required output temperature is small [24].

Typical GSHPs and WSHPs achieve COP values of 3–5, which is considerably more efficient than conventional Heating, Ventilation, and Air Conditioning (HVAC) or air-source heat pumps. This means they can deliver three to five times more heat energy than the electrical energy they consume. For example, Yu (2024) reported that borehole fluid at 17 °C was upgraded to 43 °C to de-ice a bridge deck, achieving a heat flux of 230 W/m² for a 20 cm asphalt layer [76]. Such studies show the potential of heat pumps for infrastructure heating and highlight the need to evaluate whether temperature lift is necessary for the Oostbrug or whether a heat pump with minimal lift offers a more efficient solution.

2.2.3. Storage

Most heat can be harvested in summer but is needed in winter; therefore, storage is crucial. Seasonal systems such as ATES allow heat to be captured and reused later, though not without losses. This subsection explains the principles of thermal storage and its role in achieving year-round reliability.

An ATES stores surplus thermal energy underground to meet heating demand at a later stage. Since transport losses (heat lost while water is being moved through pipes), exchanger losses (heat lost in the

heat exchanger, the device that transfers heat between fluids), and storage losses (heat that escapes from the underground storage area) reduce recovery efficiency, the stored energy must exceed the actual demand. Reported values are around 0.25% per kilometer for transport losses [28], about 5% for heat exchangers [23], and geometry-dependent losses (Figure 2.13), heat losses that depend on the shape and size of the underground storage area [7]. These mechanisms directly influence the design parameters relevant for the bridge case.

The required storage volume (Equation 2.2) follows from the thermal demand and injection/extraction temperatures. Dividing the required flow rate by the maximum permissible flow rate of the aquifer (Equation 2.3), defines the number of doublets, pairs of wells (one warm and one cold). Finally, the thermal radius (Equation 2.4), the distance around the well that is affected by the stored or extracted heat, links storage volume to aquifer geometry and provides the basis for estimating conduction, dispersion, and buoyancy-driven flow effects. This latter is a flow caused by density differences between warm and cold water.

$$V_{\text{ATES}} = \frac{Q_{\text{th}}}{c_w \times (T_{\text{sh}} - T_{\text{sw}})} \tag{2.2}$$

$$\dot{V}_{req} = \frac{Q_{th,max}}{c_w \times (T_{sh} - T_{sw})}; \quad \dot{V}_{max} = u_{\max} \times h \times 2 \times \pi \times r_w \tag{2.3}$$

$$R_{th} = \sqrt{\frac{\rho_w \times c_w \times V_{ATES}}{\rho_a \times c_a \times \pi \times h}} \tag{2.4}$$

To capture these losses, the area-to-volume ratio (A/V) is used (Equation 2.5). A higher A/V amplifies conduction losses, while $L = 3R_{th}$ represents a balance that limits tilting effects (the sideways shifting or leaning of the warm water body underground). When the ratio L/R increases, tilting of the warm water zone occurs (plume tilting), which makes heat recovery less efficient, reducing recovery [7]. With the well screen length (L), the perforated section of the well through which groundwater can flow in or out is set equal to the aquifer thickness (h). These ratios are plotted against each other in Figure 2.13. For the bridge case, these simplified relations provide a practical framework to estimate ATES efficiency without detailed subsurface modeling.

$$\frac{A_{\text{th}}}{V_{\text{th}}} = \frac{2}{L} + \frac{2}{R_{\text{th}}}; \quad L = 3 \times R_{\text{th}} \tag{2.5}$$

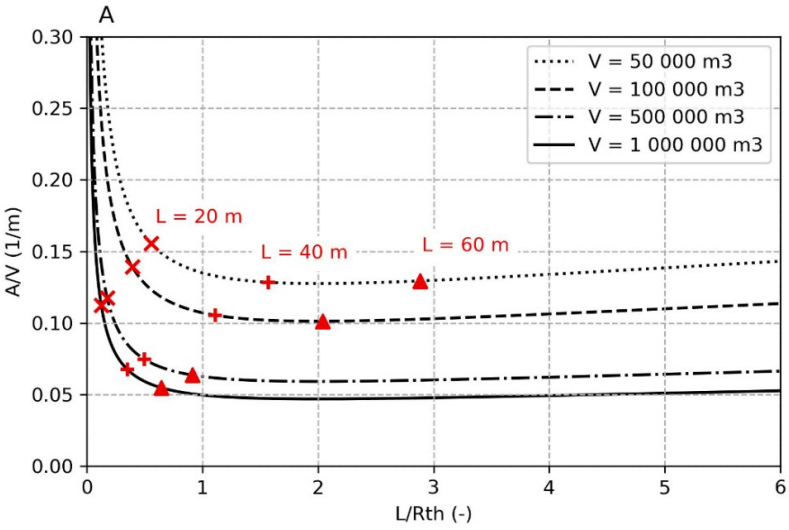

Figure 2.13: Conduction losses vs. plume tilting; lines show aquifer volumes, optimum red plus [7]

2.3. Electrical Energy

For the Oostbrug, electrical energy is needed to operate the bascule mechanisms (the moving bridge sections), auxiliary systems, and lighting. Demand is characterized by short but high peaks during bridge movements, alongside a continuous low baseline for monitoring and illumination. Local renewable generation, mainly through solar panels on walls and small wind turbines along the IJ, can offset this demand. However, temporal mismatches between peak loads and renewable supply require on-site storage, such as batteries, to ensure reliable operation and reduce dependence on the grid. This chapter outlines the bridge's electrical demand profile, feasible supply options, and storage systems as the basis for integrated design.

2.3.1. Demand

For the Oostbrug, both one or two movable arms (called leaves) for the bascule bridge designs are under consideration. The leaves can either pivot around a fixed horizontal axis (Figure 2.14 a, b, d) or roll backward on a curved track (Figure 2.14 c) [22]. Although the large counterweights of the "Dutch" drawbridge or a deep pier minimize the effort required to move the bridge, hydraulic or electrical power is still needed to drive the mechanism [77]. Counterweights are heavy masses that balance the bridge leaf to reduce lifting effort. A comparable reference is the Erasmus Bridge in Rotterdam, which features a single bascule span of similar scale and demonstrates the feasibility of such a design. Only for this design, the movable span pivots upward around a fixed horizontal axis (Figure 2.14 b) and the counterweight is integrated into the structure, below deck level, balancing the lifting leaf.

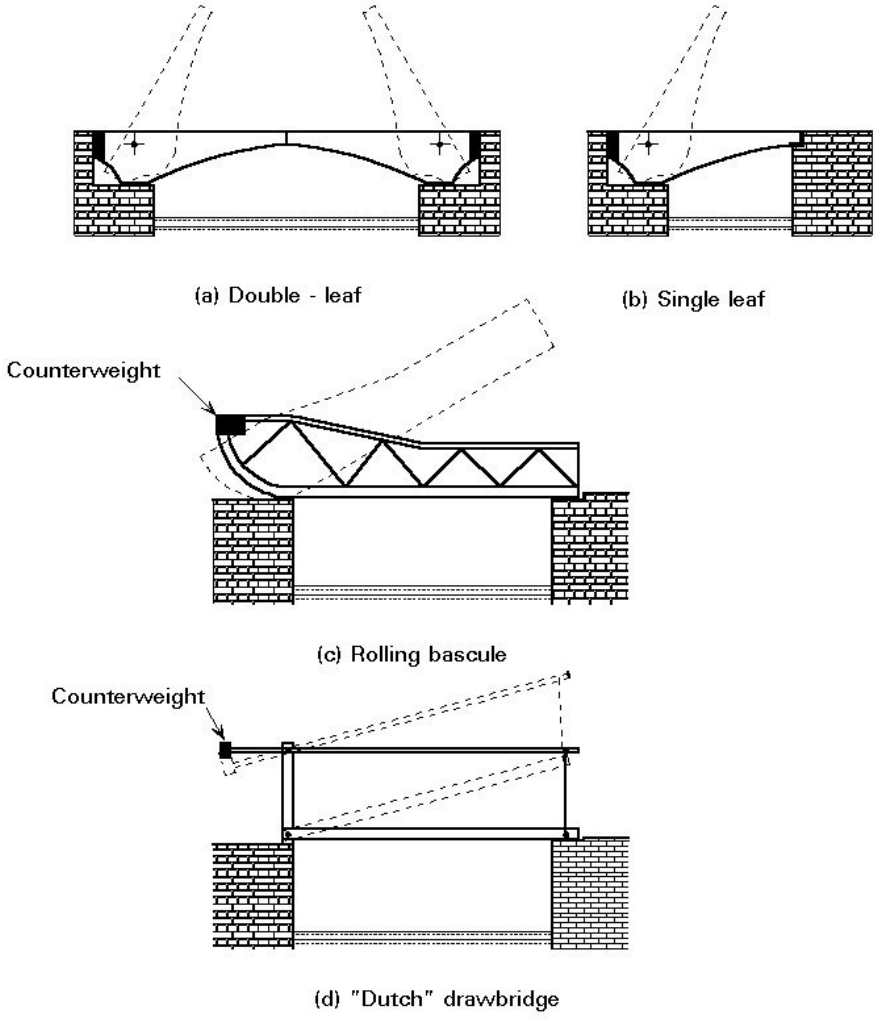

Figure 2.14: Bascule bridge types with fixed-axis (a,b,d) vs. rolling (c) [22]

The electrical demand of a bascule bridge can be grouped into three main categories: auxiliary systems such as distribution and control equipment, heating, and lighting loads. In terms of energy use in relation to each other, the installed capacity is typically distributed at around 30% for heating and control, 55% for lighting, and 15% for machinery of deck movement. However, when looking at actual operational power use, the machinery becomes the dominant consumer, accounting for more than 70% of the total power demand during bridge movements [1].

A critical design choice is whether the bascule bridge will use a single or double leaf. For a single-leaf span, the moving section must overcome higher instantaneous drive power requirements than for a double-leaf configuration. When the bridge is idle, energy use is relatively low, with lighting becoming the dominant load. Despite its modest share, the reliability of emergency generators, backup power units used during outages, is of major importance to ensure safe operation in the event of mid-operation failures.

2.3.2. Supply

Renewable electrical energy sources can be integrated into bridge environments, but their performance and installation constraints must be carefully considered. On bascule bridges, where counterweight tuning is critical, the placement of hardware is especially important. In other studies, solar panels mounted beneath a bridge with reflective mirrors are effective [55], but this solution is unsuitable for bridges spanning water, excluding this from the theoretical analysis. Small wind turbines can also be integrated; beyond generating electricity, they can provide an additional benefit by contributing to vibration damping, reducing unwanted structural vibrations, through their rotating blades [42].

Solar and wind Energy

Solar panels installed on bridge railings can provide substantial energy generation, particularly on long bridges, due to the large available surface area. While the bridge deck itself could also host solar panels, this option is less desirable because of potential deterioration caused by traffic and travelers. In a study on photovoltaic noise barrier (PVNB) integration [62], noise-reducing walls with integrated solar panels, illustrated in Figure 2.15, several panel configurations were analyzed. Among them, the shingle configuration yielded the highest energy output, regardless of solar orientation throughout the day. However, top-mounted bifacial panels facing east achieved nearly the same morning and afternoon energy capture as the shingle configuration. Importantly, the fastest payback times were achieved with the top-mounted tilted and bifacial options when placed in southern or eastern orientations, since these required fewer panels. Still, if maximizing long-term energy production and durability is prioritized, the shingle or vertically built-on options are preferable.

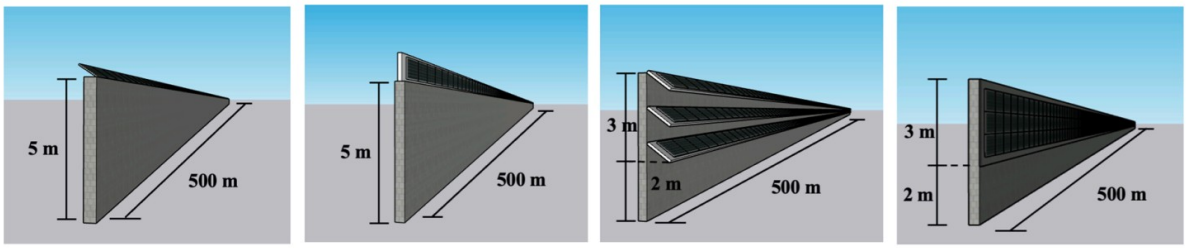

Figure 2.15: PVNB tilted, bifacial, shingles, vertical configurations [62]

The effectiveness of tilted and shingle-type configurations has also been demonstrated by Guo et al. (2025). In their study, solar panels were mounted at a 45° angle on the sides of the bridge deck, combined with small wind turbines installed on top (Figure 2.16). This hybrid system improved the overall wind environment for bridge traffic, though it also increased wind load on the bridge deck itself [32].

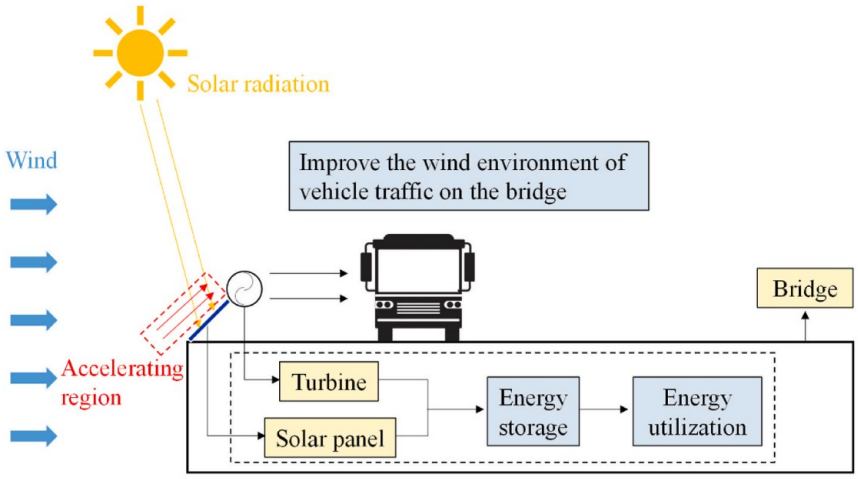

Figure 2.16: Hybrid wind-solar configuration on bridge deck [32]

Vertical-axis wind turbines (VAWTs), turbines that spin around a vertical shaft, and other small wind technologies are increasingly considered for integration into built environments where space is limited. Research shows that, although their power output in dense urban areas is relatively small, careful positioning on aerodynamically favorable structures, locations where airflow is naturally accelerated, can increase wind speed by up to 27%, thereby improving turbine efficiency [36]. Bridges, particularly those spanning rivers, provide such opportunities because they are naturally exposed to stronger and less obstructed winds than inner-city bridges (Figure 2.17). For this reason, small-scale installations, such as horizontal-axis turbines with 3.7 m blades producing 2.4 kW or vertical-axis turbines of 0.8 m diameter producing around 2 kW, can be placed on traffic lights at regular intervals to generate modest but practical amounts of power [36]. Horizontal-axis turbines have rotors that spin like airplane propellers. Studies also demonstrate that micro-wind turbines with multi-blade rotors can successfully power bridge monitoring sensors under moderate wind conditions [54]. Taken together, these findings highlight that small-scale wind technologies are not only feasible but also functional when strategically deployed on bridge infrastructure.

Figure 2.17: Bridge-integrated wind and solar energy harvesting systems [30]

Building on this small-scale potential, larger integrated systems offer even greater promise for energy harvesting on bridges. For instance, incorporating helix-shaped vertical-axis turbines or larger horizontal-axis turbines directly into the bridge structure allows both greater energy capture and im-

proved mitigation of bridge vibrations caused by wind, which can reduce resonance and enhance structural stability [36, 54]. Hybrid systems take this integration further: solar panels installed along bridge deck railings can complement wind energy, creating diversified energy portfolios with higher reliability [30]. These combined approaches suggest that bridge infrastructure can be redefined not only as a means of transportation but also as an active site of renewable energy generation. In this way, small-scale turbine applications (Type I) create a pathway toward more advanced hybrid solutions (Types II and III) shown in Figure 2.17, ensuring that bridges contribute meaningfully to sustainable urban energy systems.

2.3.3. Storage

Battery storage systems play an important role in balancing electricity demand and supply, particularly for applications such as peak shaving, reducing short-term demand spikes, and maximizing self-consumption. Within the category of electrochemical storage, lithium-ion batteries and flow batteries represent the most relevant technologies for modern building-scale systems, while paper and flexible batteries are excluded from this analysis due to their limited applicability in large-scale contexts [18]. On the cell level, lithium-ion batteries offer considerably higher power and more energy per unit of mass and volume (density), enabling compact installations that can handle peak loads efficiently and minimize the required footprint [46]. Flow batteries, by contrast, are less dense but can be constructed vertically, which partially offsets this limitation in spatially constrained environments (Figure 2.18) [57].

However, density advantages must be weighed against other operational characteristics: lithium-ion batteries typically reach only about 500 full charge–discharge cycles, roughly half the durability of flow batteries, and they also involve higher toxicity risks [46]. These differences underline that technology selection cannot be based on density alone but must also account for lifecycle performance and safety in site-specific conditions. For the bridge case, where spatial limitations and safety considerations are both relevant, these trade-offs provide a methodological basis for comparing the two technologies.

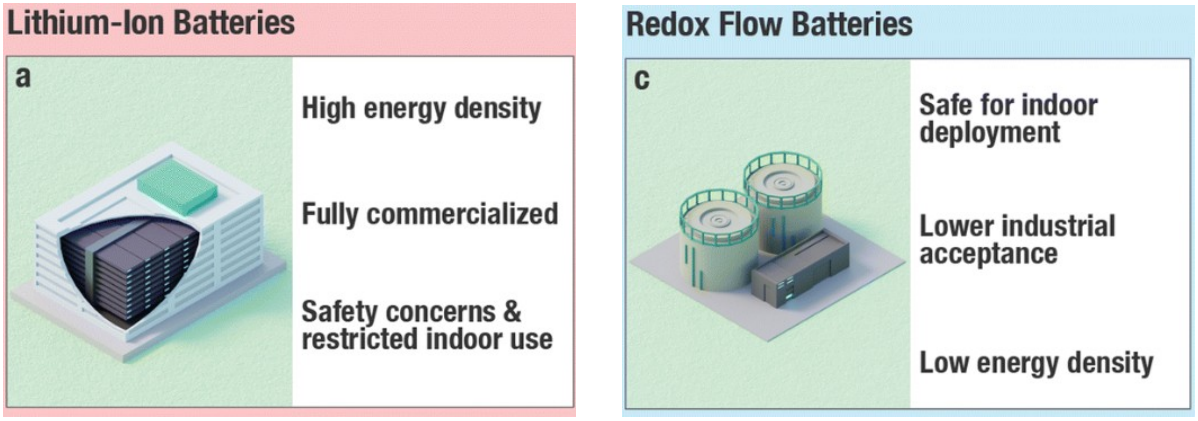

(a) Lithium-Ion batteries **(b)** Redox Flow Batteries

Figure 2.18: Electrochemical battery storage site specifications [57]

Narada Power [51], a China-based manufacturer and global supplier active since 2001, illustrates the current market maturity of lithium-ion storage solutions. With exports to more than 158 countries, the company exemplifies how lithium-ion technology has already achieved large-scale deployment and established industrial supply chains. This strengthens the argument for considering lithium-ion batteries as a baseline option in the case study, while the comparative advantages of flow batteries in terms of durability and lower toxicity provide a meaningful counterpoint.

2.4. Embodied CO_2 emissions

The embodied CO_2 of the system is assessed by focusing on the heat exchange components of the energy piles, aquathermal heat exchangers, and the ATES storage system compared to the embodied CO_2 of calcium chloride ($CaCl_2$) salt use for conventional de-icing. Energy piles and aquathermal heat exchangers calculations will be explained in the methodology section since they are unique for their own system parameters. The bridge deck tubes are excluded from this analysis, since they are present in all design options and therefore do not influence the comparative outcomes. This scope ensures that the results reflect only the differences in heat exchange capacity and material choice, which are decisive for the environmental performance of the bridge energy system.

In terms of life cycle assessment (LCA), a method for evaluating environmental impacts across a product's life, the analysis is limited to the product stage, or "cradle to gate," as indicated in Figure 2.19. This stage comprises raw material supply, transportation to the factory, and manufacturing [11]. Focusing on this boundary condition aligns with identifying design-dependent embodied emissions, while excluding operational and end-of-life phases.

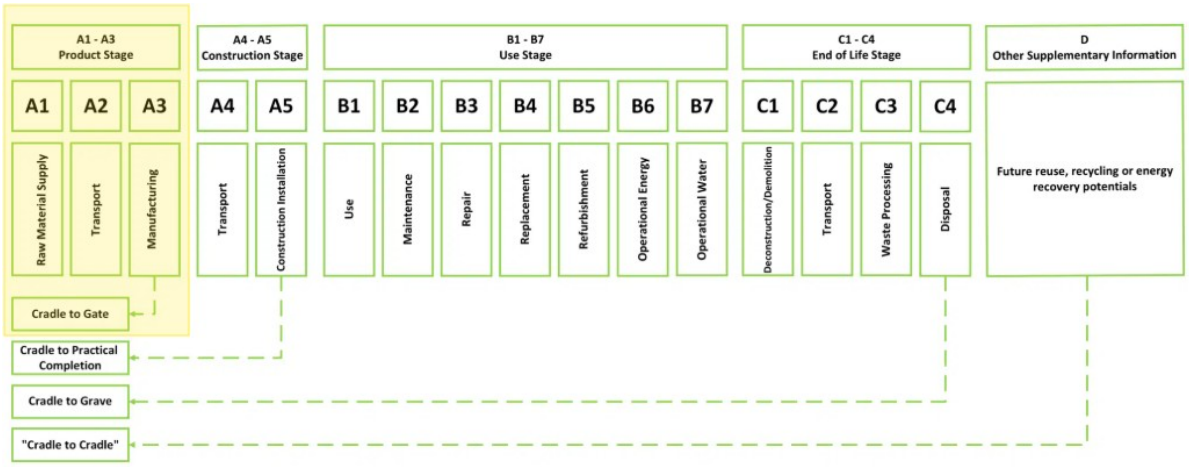

Figure 2.19: Circular ecology framework, highlighting cradle to gate section [11]

Using calcium chloride de-icing salt on a 14,400 m² deck area of the Oostbrug at a rate of 12 g/m² for 30 applications per year (chapter 1) results in about 5.2 tons of salt annually, corresponding to roughly 7.9 t CO_2 per year (based on 1.53 kg CO_2/kg $CaCl_2$ for transport and processing in the product stage of the salt [9]).

For an ATES, no reliable data are available on the embodied CO_2 of the product stage (raw material extraction and manufacturing). Therefore, this stage is excluded from the analysis. Instead, the construction stage (phase covering drilling, installation, and surface works) is considered, as it represents the main contribution of ATES before operation.

The environmental assessment of typical ATES systems shows that only about 14% of the total greenhouse gas emissions stem from subsurface works, surface installation, and well construction, while the largest share (83%) is related to electricity consumption during operation. Decommissioning (the removal of the system after its lifetime) has a negligible impact [65]. Expressed per unit of delivered heat, the embodied emissions amount to around 83 gCO_2/kWh_{th}.

Part II – System Design and Quantitative Analysis

3

General Methodology

Part II examines the energy needs of the Oostbrug through five alternative heating systems, divided into direct and indirect heat supply approaches. For direct systems, energy is generated and directly used, while indirect systems use intermediate thermal storage. Each configuration is evaluated under shared boundary conditions to assess thermal performance, storage potential, and electrical balance, including pump or heat-pump demand and renewable inputs from calculated wind and solar. The direct systems (chapter 4) focus on heat delivery with a fixed bridge deck flow rate, whereas the indirect systems (chapter 5) adjust the deck and storage loops to balance summer and winter operation and ensure equal power transfer. This part addresses:

- *Sub-question 2: What is the Oostbrug's thermal energy demand profile?*
- *Sub-question 3: How much usable thermal energy can be extracted from the IJ River under seasonal temperature variations?*
- *Sub-question 4: Which renewable electricity sources (solar and wind) are feasible on the bridge based solely on energetic potential?*

3.1. Purpose and Structure of Part II

This part of the thesis investigates how different renewable heating and power concepts can be integrated into the Oostbrug to achieve energy self-sufficiency. The assessment is organised into two groups. In direct systems, heat is supplied directly from its source; Energy piles or aquathermal exchangers are connected to the bridge deck, without the use of intermediate seasonal storage. In contrast, indirect systems first harvest and store heat; An ATES is explained in subsection 2.2.3 , which is subsequently used to supply the deck during winter operation. The overview of different heating systems are summarized in Table 3.1:

Table 3.1: Overview of the heating supply systems

Group	Systems	Heating Type	Storage
Direct	1 – Water-based pile + HP 2 – Ground pile + HP 3 – Aquathermal + HP	Heat delivered directly	None
Indirect	4 – Aquathermal + ATES 5 – Bridge deck + ATES	Heat stored seasonally	ATES

3.2. Method and Framework

Figure 3.1 outlines a four-step framework used to consistently evaluate all heating systems under identical conditions. First, the de-icing demand of the bridge deck is determined, followed by defining the bridge layouts for both direct and indirect systems and boundary conditions. The modelled IJ-water temperature provides input for the heating models and defines when heat extraction is permitted (systems 1, 3, and 4). Renewable electricity supply is applied uniformly across all configurations. Next, thermal and electrical performance are evaluated as interdependent subsystems: pump operation drives electricity demand, while renewable availability limits autonomy. chapter 4 analyzes pump and heat-pump electricity use, and chapter 5 includes storage charging, discharging pumping. Finally, results are compared in terms of energy coverage, embodied CO_2, and battery sizing.

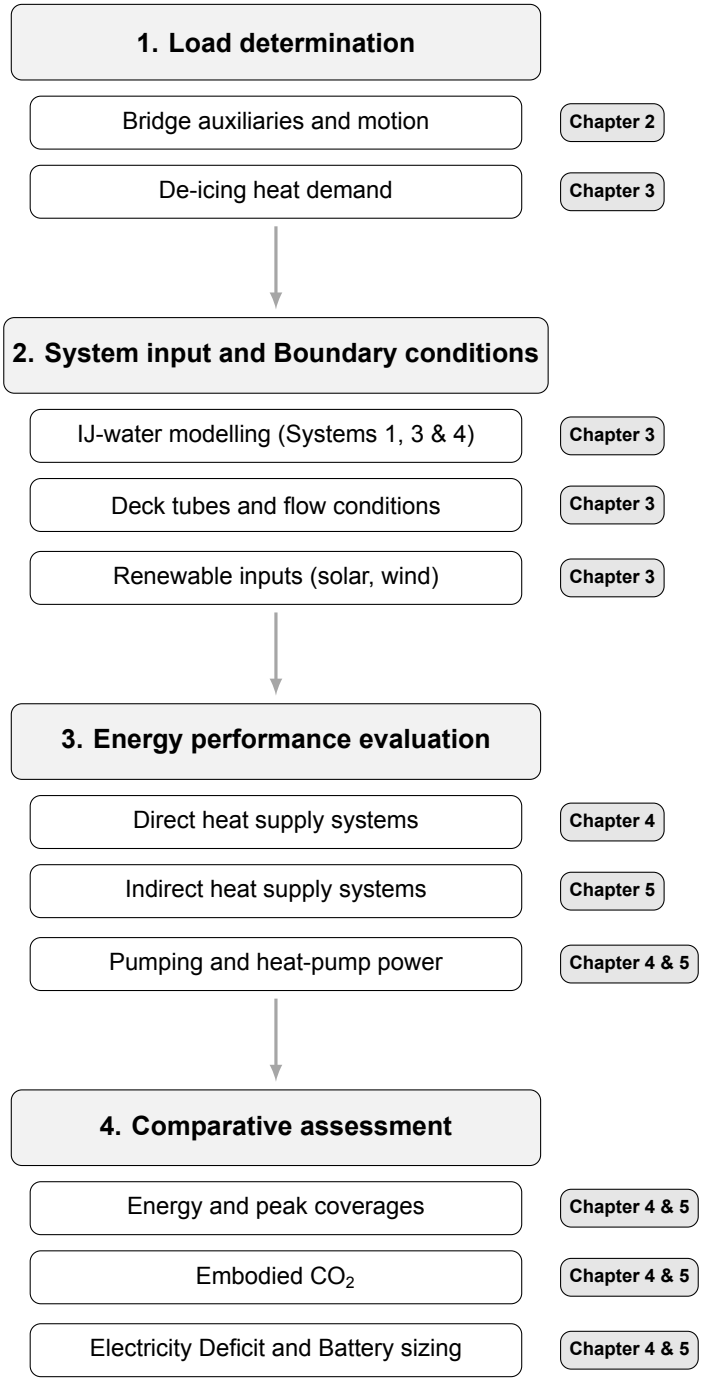

Figure 3.1: Methodological framework for system assessment

From this framework, the thermal de-icing demand, IJ-water temperature modelling, renewable solar and wind inputs, the energy performance evaluation of each system configuration, accompanied by its comparative assessments, were all carried out in MATLAB R2024b. The software environment was used to implement the numerical models, process the KNMI datasets, and generate the figures and results presented throughout this report.

1. Load determination

The electricity demand from deck motion and auxiliary systems has been determined in the literature review in section 2.1. Results show an annual consumption of 33.5 MWh for a double-leaf and 37.4 MWh for a single-leaf bascule bridge, with lighting representing the largest share and deck motion contributing only 8–18% of total demand. In chapter 4 and chapter 5, electricity demand from the pumps and heat pumps are calculated for each heating system.

In addition to these electrical loads, the bridge requires thermal energy for de-icing to ensure safe operation during freezing conditions. The following section therefore focuses on calculating the de-icing heat demand, based on climatic conditions and the surface energy balance of the bridge deck.

De-icing heat demand

The thermal load of the bridge deck is derived from a surface-energy balance as shown in Figure 2.4 in subsection 2.2.1, driven by the Royal Netherlands Meteorological Institute (KNMI) for Amsterdam in 2024 climate data [41]. Hourly air temperature, wind speed, and solar radiation define convective and radiative exchange with the deck surface. The hourly demand profile derived from Equation 3.1 is shown in Appendix C. This method reflects a simplified energy balance. The overall heat transfer coefficient (*U*-value) was modeled as a function of wind speed. These U-values are based on prior studies conducted by Filippini [25] from Haskoning, using climate reference data from KNMI, and supported by scientific literature on wind-driven convection over exposed surfaces.

The systems were designed to maintain the deck temperature above 0 °C during freezing events. Heating operation is initiated when $T_{\text{air}} < 2\,^{\circ}\text{C}$ [48, 13]. For the entire deck length, an annual energy of 222.3 MWh and a maximum power of 3 MW is required (Figure C.3). With a total deck area of 14,400 m², the heat flux for de-icing is 208 W/m². The calculated heat-demand profile was used to compare if the heat supply systems in chapter 4 and chapter 5 meet the required yearly power and energy profile. The required heat for de-icing is calculated as:

$$Q = A\,U\,\Delta T \tag{3.1}$$

where Q is the bridge deck heat demand (W), A the bridge surface area (m^2), U the overall heat transfer coefficient (W/m^2K), and ΔT the temperature difference (K).

2. System input and Boundary conditions

This framework defines the environmental and structural parameters governing system operation. The IJ-water temperature is modelled through a one-dimensional heat-balance approach to provide boundary conditions for heat exchange with surface water. Bridge geometry for direct and indirect systems with storage is given, flow and deck tube system boundaries, and renewable inputs from solar and wind energy are incorporated to represent realistic physical and climatic conditions, forming the basis for subsequent energy performance evaluation.

IJ water temperature modelling

The IJ-water temperature is modelled to provide the boundary condition for systems exchanging heat with surface water (systems 1, 3, and 4). The river is locally treated as a static water body, represented by a simplified one-kilometre-long section of the IJ. A one-dimensional heat-balance model based on De Graaf et al. [14] is applied, as defined in Equation 3.2 and Equation 3.3. The total heat flux H_{total} includes short- and long-wave radiation, convection, evaporation, and ground conduction. An initial water temperature of 7.6 °C in January is assumed [61]. Ground conduction is modelled with a thermal conductivity of 2.16 W/m·K [8], a ground temperature of 10 °C, and a conduction depth equal to the river depth.

$$H_{\text{total}} = H_{\text{sl}} + H_a + H_l + H_e + H_c + H_f + H_{\text{ground}}, \tag{3.2}$$

$$T_{\text{water}} = T_{\text{old}} + \frac{H_{\text{total}} A}{\rho c_p V}, \tag{3.3}$$

where T_{water} is the updated water temperature (°C), T_{old} the previous water temperature (°C), H_{total} the total heat flux (W/m^2), A the water surface area (m^2), ρ the water density (1000 kg/m^3), c_p the specific heat capacity of water (4180 J/kg·K), and V the water volume (m^3).

Meteorological inputs from KNMI [41], including air temperature, wind speed, cloud cover, and solar radiation, are converted to consistent physical units and used to calculate the individual fluxes described in Appendix D. Derived parameters such as vapor pressure, emissivity, and evaporation are used to determine the total heat exchange, which updates the water temperature at each hourly time step (Equation 3.3).

The resulting IJ-water and air temperature profiles for 2024 are shown in Figure 3.2. The figure also indicates that heating operation is required for approximately 326 hours per year, corresponding to periods when $T_{\text{air}} < 2$ °C.

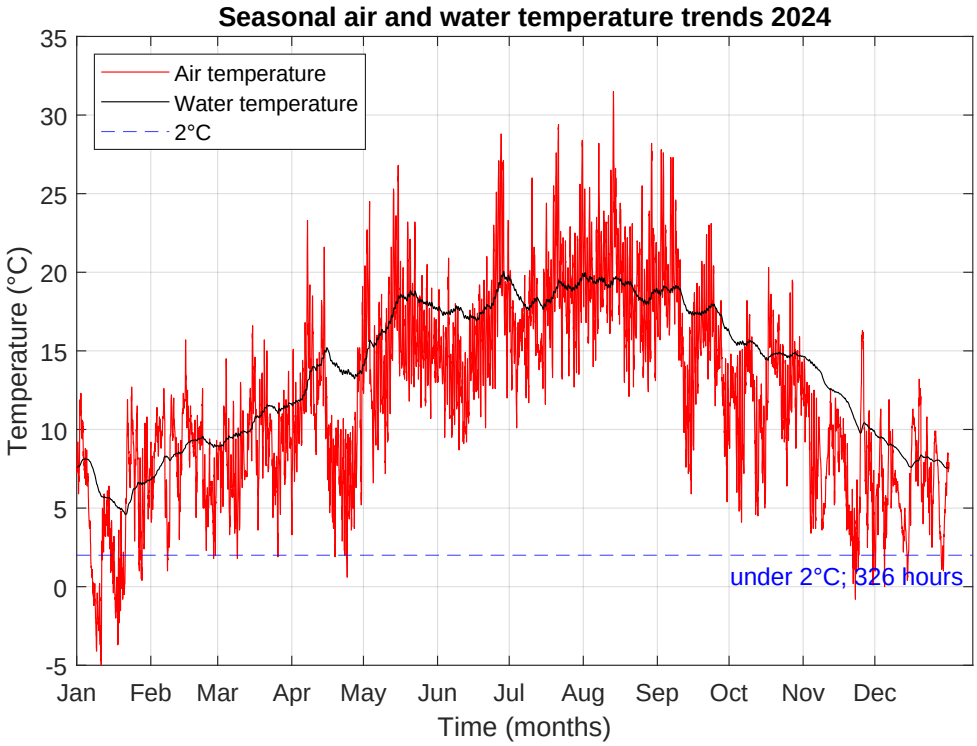

Figure 3.2: Computed IJ-water and air temperature from KNMI data, Amsterdam 2024[41]

Direct systems: bridge layout

Figure 3.3 shows the schematic top view of the Oostbrug for the direct system layout. This modular division is for the direct systems configurations, where the indicating pillar foundations support systems 1 and 2. The bridge is divided into four main structural sections, arranged symmetrically along the north–south axis. Each section is supported by pillar foundations, which differ in geometry and subsurface conditions. This variation in the pillar foundations is the main reason for dividing the bridge into separate hydraulic zones. In addition, the shortest span between two main structural sections open for vessel passage, meaning that the hydraulic systems are separated so that no single system needs to cross an open bridge. Each zone corresponds to a distinct foundation group and can therefore host its own energy-exchange system and operational control.

Each section can be equipped with parallel tube loops that allow the circulation of a heat-transfer fluid through the deck. The arrows indicate the conceptual flow directions of the hydronic circuits. The deck segment measuring 96.5 m will hereafter be referred to as the short deck length, while the segment measuring 468.5 m will be referred to as the long deck length.

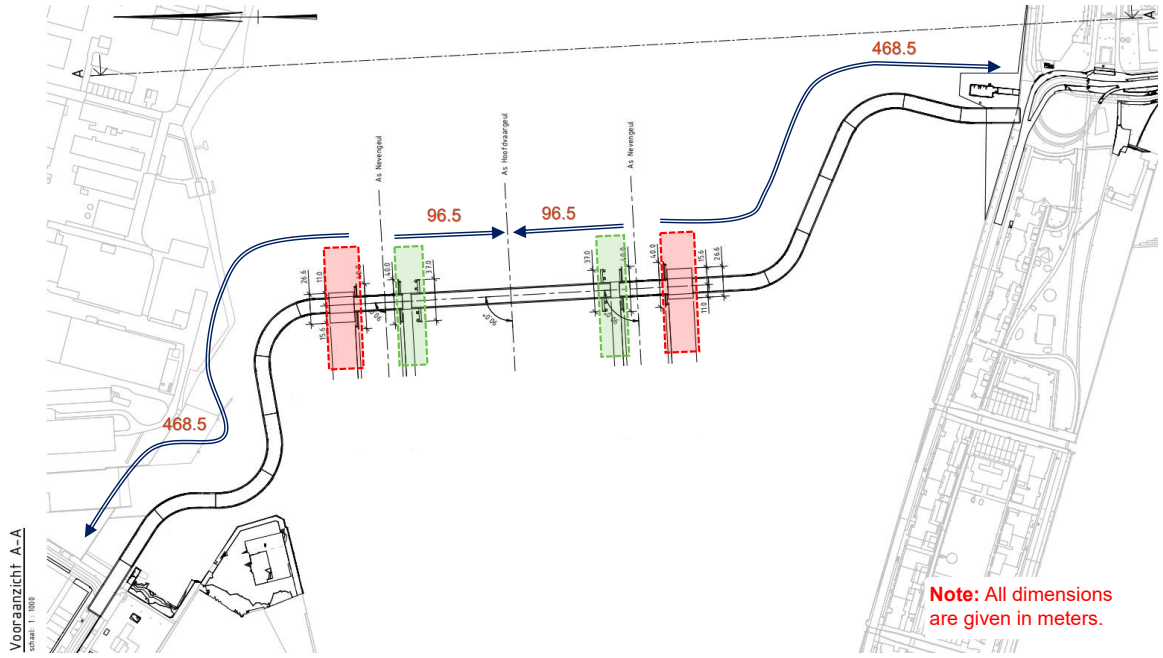

Figure 3.3: System 1-3: cellar (red) and main (green) pillars and flow direction arrows

Each configuration of the direct system is modeled using an hourly energy balance to determine heat flows, with parameters scaled to the representative bridge section lengths. Two foundation systems are considered: System 1, water-adjacent piles (6.5 m) that enable direct aquathermal exchange with the IJ water, and System 2, ground-embedded piles that extend into deeper soil layers for subsurface exchange. System 3, combining both open and closed aquathermal systems, is designed to meet the required thermal demand (calculated accordingly). In contrast, the performance of Systems 1 and 2 depends on the number of bridge piles, reflecting a different approach for each system.

Indirect systems: bridge and ATES layout

In addition to the water-adjacent piles, the ground-embedded piles, and the aquathermal systems (system 3), the bridge is coupled to ATES systems to enable seasonal heat management for the two indirect heating system configurations (systems 4 and 5). In these concepts, the bridge deck's hydronic network is divided into two main supply zones: one on the north side and one on the south side of the bascule span. With a deck length of approximately 600 meters. Each side is connected to a dedicated ATES installation located on the corresponding riverbank. This dual arrangement allows each half of the bridge to operate semi-independently, reducing distribution distances and hydraulic losses while maintaining operational flexibility. ATES systems are not installed beneath rivers because fluctuating groundwater flow and hydraulic gradients cause thermal losses and instability in heat storage [49]. Figure 3.4 shows this bridge layout.

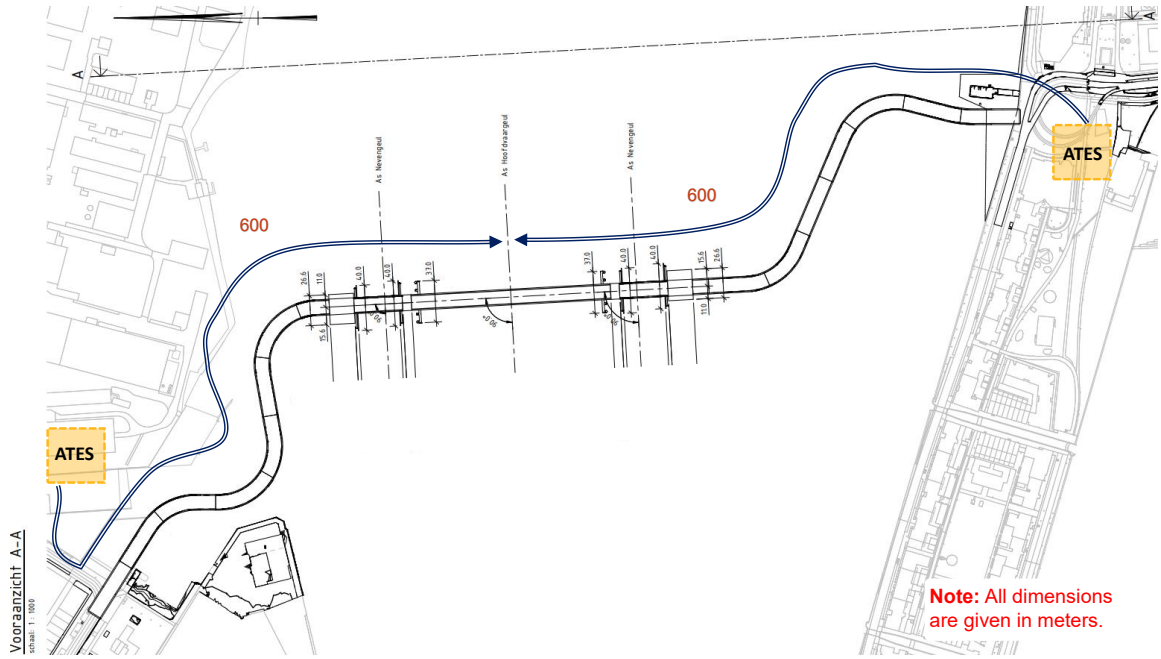

Figure 3.4: System 4-5: ATES on both river sides serve 600 meters deck

The ATES system functions as a pair of wells: a warm well that stores surplus heat collected during summer and a cold well that stores chilled groundwater for potential cooling use. During winter operation, the stored heat can be extracted and supplied to the bridge deck loops via a heat exchanger and circulation pumps. In summer, excess heat from the deck can be reinjected into the warm well, effectively closing the annual thermal balance of the system.

It is assumed that the required supply and return pipelines can cross the movable bascule span. From a design perspective, this configuration focuses on the energy-system functionality and distribution logic; the precise mechanical integration with the movable bridge components lies outside the scope of this study.

Deck tubes and flow conditions

Chosen is for a concrete deck structure variant (Figure 2.1) from Haskoning [34] consisting of 1.5 m of prefabricated concrete with a 5 cm cast asphalt top layer. The bridge deck is assumed to be composed of reinforced concrete, providing sufficient strength and thermal conductivity for the integration of embedded hydronic tube systems used for heating and cooling. A small section of 25 cm will be cast in situ to finish and fix pipes. A reinforced concrete deck is preferred for integrating embedded hydronic tubes, as opposed to a steel deck with low thermal mass, as described in subsection 2.2.1.

The deck layout consists of 40 sections in length by 12 in width, resulting in a total of 480 tube loops. Each loop is approximately 1 m wide and 30 m long, giving an effective stretched length of about 200 m, calculated from the strip width, tube spacing, and section length. The tube diameter is 0.023 m (Table 3.2). For both summer and winter operation, each tube loop must be able to either deliver a certain heat flux (heating in winter) or absorb it (cooling in summer), which primarily depends on the flow rate [43]. The temperature difference is nearly the same across the system and the deck loops, since main line losses are negligible at high flow and each loop's flow is scaled to its surface area.

The required flow rate is set to 0.6 m/s as used in Lyu et al. [43]. This is done for the reason that the optimal inlet temperatures Figure 2.6 in subsection 2.2.1 can be compared to this report's bridge deck layout tube system. In Figure 3.2, the minimum air temperature in Amsterdam for 2024 is -5 °C outside, the minimum inlet temperature for de-icing is between 16 and 18 °C with a tube spacing of 15 cm [43]. Moreover, this is supported by the findings of Studios [66], which determined an inlet temperature range of 15–20 °C to achieve a heat flux of 208 W/m² (Figure 2.11), as required for de-icing the entire deck of the Oostbrug during the coldest moment in Amsterdam for 2024.

Using the values in Table 3.2, the flow rate for a single tube is calculated and subsequently multiplied by the total number of tubes to obtain the overall flow rate possible through the deck (Table 3.2).

Table 3.2: Parameters for the bridge deck tubes

Parameter	Symbol	Value	Unit
Section width	W	1	m
Section length	L	30	m
Tube spacing	s	0.15	m
Number of tubes	$N = W \times L$	480	-
Length of tube	$l = \frac{W}{s} \times L$	200	m
Tube diameter	D	0.023	m
Flow velocity per tube	v	0.6	m/s
Total flow rate	Q	0.12	m³/s

Solar energy input profile

Solar electricity production was estimated based on the available hourly solar irradiance combined with assumed system efficiencies. The photovoltaic (PV) panels were assumed to cover 1.2 meters of the railing by 1200 meters of the bridge deck length, for both sides. A panel conversion efficiency of 20% was used, 10% loss of shadow on the railing, along with a system-to-user efficiency of 85%, which accounts for losses in inverters, cabling, and other components. These assumptions yield a total effective efficiency of 15.3% [70].

Solar panels benefit from high irradiance during summer months. Hourly climate data from the KNMI for Amsterdam in 2025 was used [41]. The hourly energy yield from solar power was calculated in Equation 3.4. The total annual solar energy production was obtained by summing all hourly values and converting the result to MWh.

$$P_{\text{solar}} = Q_{\text{sol}} \cdot Q_{\text{duur}} \cdot A \cdot \eta_{\text{effective}} \tag{3.4}$$

where P_{sol} is the solar power (W), Q_{sol} the solar irradiance (W/m^2), Q_{duur} the hourly duration (h), A the total bridge deck area (m^2), and $\eta_{\text{effective}}$ the effective efficiency (%).

In Figure 3.5a the total energy energy accounts for 203.5 MWh yearly and the layout of the solar panels on the railing is shown in Figure 3.5b.

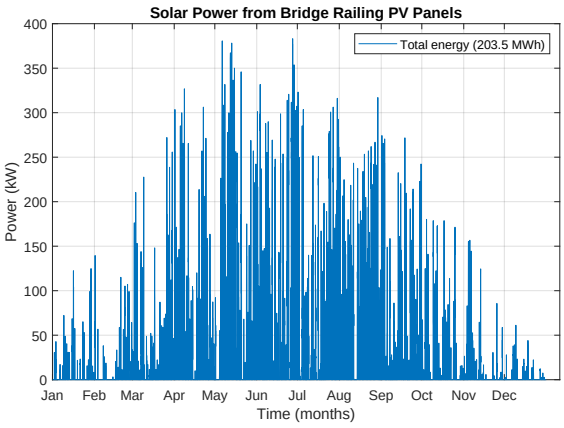

(a) Solar irradiance converted to energy from the railings of the bridge

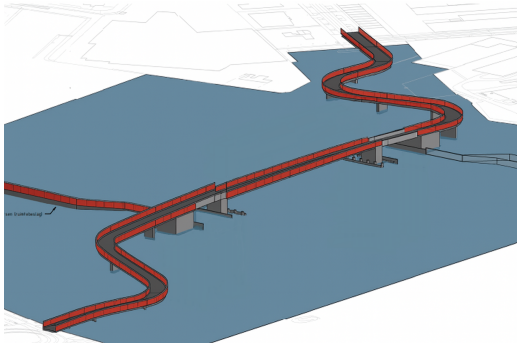

(b) Layout of the solar panels on the railing of the bridge.

Figure 3.5: Solar energy potential

Wind energy input profile

Wind energy generation was evaluated for a layout consisting of eight vertical-axis wind turbines (VAWT)

positioned along the bridge with a total height that can differ between 8 to 15 meters of the entire mast. Each turbine has a blade diameter of 5 m and operates with a system efficiency set to 35% since the average hourly wind speed at this height is 6 m/s. The air density was set at 1.3 kg/m³ [69].

Wind turbines can supplement energy production during windier period. Hourly climate data from the KNMI for Amsterdam in 2025 was used [41]. The energy production for a single turbine was calculated in Equation 3.5. Accordingly, the output was scaled up to a total of 8 turbines and summed over all hours in the year to obtain the total annual wind energy production.

$$P_{\text{wind}} = \frac{1}{2} \cdot \rho_{\text{air}} \cdot A \cdot v^3 \cdot \eta \tag{3.5}$$

where P_{wind} is the wind power (W), ρ_{air} the air density (kg/m^3), A the rotor swept area ($\pi D^2/4$), v the wind speed (m/s), and η the efficiency (%).

In Figure 3.6a, the power outcomes of two times a 4 stacked rotor (2 layers of blades on one shaft) are shown. The estimated wind power potential of up to 200 kW was based on a wind speed of 18 m/s from the KNMI data. However, such wind speeds are unlikely to occur at the considered hub height, and this estimate can therefore be disregarded. Two wind turbines are positioned on a part of the bridge deck, as shown in Figure 3.6b.

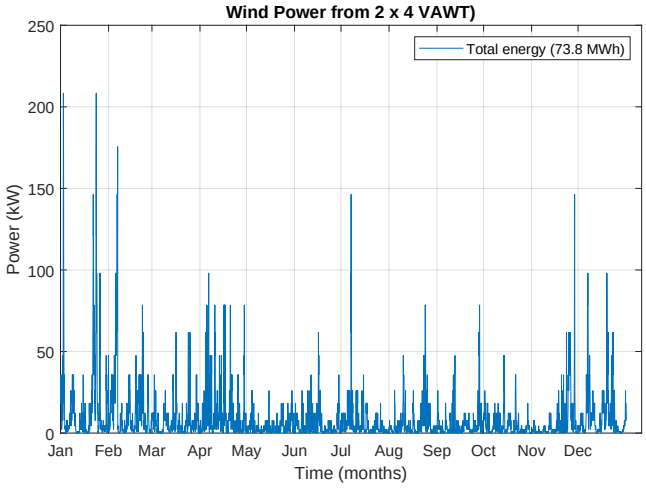

(a) Wind speeds converted to wind power

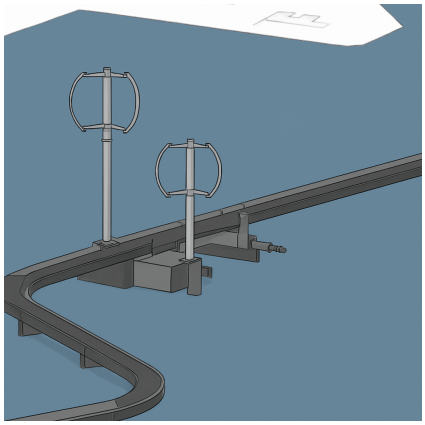

(b) Layout 1 × 2 VAWTs, mirroring the opposite side (slightly out of scale)

Figure 3.6: Wind energy potential

3. Energy performance evaluation

This framework quantifies the electrical and thermal performance of the proposed systems. Electrical loads are disaggregated by subsystem to identify consumption patterns, peak demands, and the distribution of energy use.

For all systems, electricity demand is defined on the supply side. In the direct systems, this includes the heat pump and hydraulic pumps operating before the bridge deck circuit. For the indirect systems, electricity demand is determined by the hydraulic components associated with heat exchange and storage. In System 4, this comprises the aquathermal loop recharging from the IJ and the aquifer loop serving the warm well; between the loops, heat is exchanged. During winter, only the discharging of the aquifer loop is considered for consistency. In System 5, the aquifer loop operates in winter for discharging the warm well, while in summer, both the aquifer and bridge deck loops are included, as they jointly supply the warm well. Across all systems, the bridge deck tubing distribution hydraulics in winter itself is excluded from electricity demand calculations, since it represents a common load. Only when the bridge deck loop side acts as a supply source, as in System 5, are its hydraulics included.

Pumping and heat pump power requirements are determined from hydraulic and thermal relations, while renewable energy generation is modelled using hourly KNMI data for solar irradiance and wind speed. These parameters establish the baseline energy demand, against which renewable supply and storage performance are later assessed in Chapters 4 and 5.

Pumping and Heat Pump Power
The hydraulic and thermal parameters for each configuration are used to calculate flow rate, pressure drop, and the corresponding pumping and heat-pump energy requirements. For the direct systems, heat pumps are provided. The heat from the river water (systems 1 and 3) and the energy piles [78] (system 3) needs to be boosted to reach the temperatures required for effective de-icing and adequate power supply. A City™ RTSF Water-to-Water Heat Pump (RTSF 070 G heating only [68]) is used with a heating capacity between 195 to 430 kW, varying with source temperatures from -12C to +30C. This heat pump works with a COP of 3, applied to all direct systems. However, for the indirect system, heat pumps are not required since the power and temperature are already sufficient.

For the hydraulic pumps, a turbulent flow with a lambda of 0.02 has been assumed. A pump efficiency of 40% was assumed for all direct systems, since for smaller pumps (≤10 kW) efficiencies between 30–50% are considered, and typically circulator pumps are used [38]. For the indirect systems, ATES generally use centrifugal pumps for water circulation between the wells and heat exchangers with a pump efficiency of 70% [40].

The governing relations are defined as:

$$\dot{V} = \frac{P_{\text{max}}}{\rho\, c_p\, \Delta T} \qquad \Delta P = f\,\frac{L}{D}\,\frac{\rho v^2}{2} \qquad \Delta P_{\text{ATES}} = \frac{\dot{V}_{max}\,\mu\,\ln\left(\frac{L}{r_w}\right)}{2\pi k h} \tag{3.6}$$

where $\dot{V}$ is the volume flow rate (m^3/s), $\dot{V}_{\text{max}}$ the maximum permissible aquifer flow rate (m^3/s), P_{max} the maximum thermal power (W), ρ the fluid density (kg/m^3), c_p the specific heat capacity (J/kg·K), ΔT the temperature difference (K), ΔP the pressure drop in the circulation loop (Pa), ΔP_{ATES} the pressure drop across the ATES wells (Pa), f the Darcy friction factor (-), L the pipe length (m), D the pipe inner diameter (m), v the mean fluid velocity (m/s), μ the dynamic viscosity (Pa·s), r_w the wellbore radius (m), k the permeability of the medium (m^2), and h the reservoir thickness (m).

The electricity input needed for the pumping electricity for all systems 1 to 5 and the input for the heat pump is performed by Equation 3.7. The resulting heat output is the power from the glycol loop plus the external electrical input of the heat pump. In Figure 3.7, the heat pump inputs and outputs are schematically drawn, which applies for systems 1, 2, and 3.

$$E_{\text{pump}} = \frac{\dot{V}\,\Delta P}{\eta_{\text{pump}}} \qquad E_{\text{elec,HP}} = \frac{Q_{\text{glycol}}}{COP - 1} \tag{3.7}$$

where E_{pump} is the pumping power (W), η_{pump} the pump efficiency (-), $E_{\text{elec,HP}}$ the electrical energy consumption of the heat pump (W), Q_{glycol} the heat exchanger thermal input by the glycol loop (W), and COP the coefficient of performance (-).

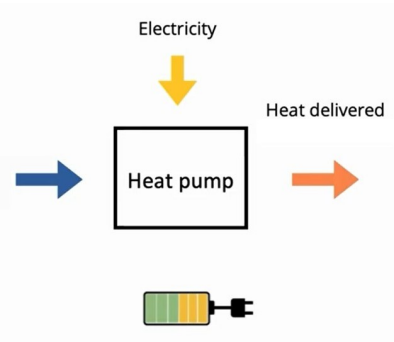

Figure 3.7: Heat pump operation principle [6]

4. Comparative assessment

This framework evaluates each system's ability to meet thermal energy demand while minimizing environmental impact and maximizing renewable energy integration. The assessment includes energy and peak coverage, embodied CO2, and battery storage performance.

Compared to the renewable generation potentials of 203.5 MWh from solar PV and 73.8 MWh from wind energy, the contribution of bridge regeneration in section 2.1 is negligible, 0.3 to 0.9 MWh, and does not significantly affect the overall energy balance. Therefore, regeneration is considered a minor input factor and is not explicitly included in subsequent system performance assessments.

Energy and Peak coverage

The performance of each system is evaluated in terms of its ability to cover the thermal energy demand and peak load of the bridge deck. The energy coverage is defined as the ratio of the annual thermal energy supplied by the system to the total annual thermal energy demand of the deck in Equation 3.8. Similarly, the peak coverage is defined as the ratio of the thermal power supplied by the system to the deck's maximum thermal power demand in Equation 3.9. Performance metrics include:

$$\text{Energy Coverage (EC)} = \frac{Q_{\text{system}}}{Q_{\text{demand,deck}}}, \tag{3.8}$$

$$\text{Peak Coverage (PC)} = \frac{P_{\text{system}}}{P_{\text{demand,deck}}}, \tag{3.9}$$

where Q_{system} is the annual thermal energy supplied (MWh), $Q_{\text{demand,deck}}$ the total annual deck demand (MWh), P_{system} the supplied thermal power at peak demand (kW), and $P_{\text{demand,deck}}$ the maximum deck demand (kW).

Emboddied CO2

The embodied CO2 per pile (system 1 and 2) is determined from the material quantities and emission factors, scaled by the total number of piles. The same approach applies to both open Stainless Steel (RVS) and closed High-Density Polyethylene (HDPE) aquathermal configurations (system 3 and 4). For each design load, the embodied CO2 is computed from the required heat-transfer area, the areal mass density of the exchanger material, and the emission factor [27, 44], according to Equation 3.10 :

$$\mathrm{CO}_{2,\text{pile}} = A_{\mathrm{HDPE}}\, L_{\mathrm{pipe}}\, \rho_{\mathrm{HDPE}}\, EF_{\mathrm{HDPE}}, \qquad \mathrm{CO}_{2,\text{hx}} = \rho_A\, \frac{Q}{k}\, EF. \tag{3.10}$$

where A_{HDPE} is the HDPE pipe cross-sectional area (m^2), L_{pipe} the U-loop length per pile (m), Q the design heat load (kW), ρ_{HDPE} the HDPE density (950 kg/m^3), EF_{HDPE} the emission factor of HDPE (2.0 kg CO_2/kg), ρ_A the areal mass density (20 kg/m^2 for RVS, 6 kg/m^2 for HDPE), k the performance factor (86.7 kW/m^2 for RVS, 2.7 kW/m^2 for HDPE), and EF the emission factor (6.0 kg CO_2/kg for RVS, 2.0 kg CO_2/kg for HDPE).

Electricity Deficit and Battery Sizing

The lithium-ion battery storage system is based on the *Narada battery rack type 3* [50], where each rack consists of 15 modules connected in series (Figure 3.8a). Each module has a cell capacity of $160\,\mathrm{A\,h}$ and a nominal voltage of $76.8\,\mathrm{V}$. The total energy capacity of one rack is calculated as Equation 3.11:

$$E_{\text{rack}} = 15 \times (76.8\,\mathrm{V} \times 160\,\mathrm{Ah}) = 184\,\mathrm{kW\,h}. \tag{3.11}$$

To determine the number of racks needed for the system, the maximum hourly energy deficit must first be calculated. This is done by evaluating the difference between the hourly power demand and the renewable energy supply. For each hour, the shortage is identified, and the cumulative sum of these shortages represents the total energy deficit that must be covered by the battery system. The cumulative energy deficit is obtained as Equation 3.12:

$$E_{\text{deficit}} = \sum_{t=1}^{T} \max\left(P_{\text{demand}}(t) - P_{\text{renewable}}(t),\, 0\right) \tag{3.12}$$

where $P_{\text{demand}}(t)$ and $P_{\text{renewable}}(t)$ are the hourly demand and renewable generation (kW), and T is the total number of hours considered. The required number of racks is determined by dividing the annual energy deficit by the capacity of one battery rack ($E_{\text{rack}} = 184\,\text{kW h}$) and each container can accommodate up to 20 racks (Figure 3.8b) :

$$N_{\text{racks}} = \frac{E_{\text{deficit}}}{E_{\text{rack}}}, \qquad N_{\text{containers}} = \left\lceil \frac{N_{\text{racks}}}{20} \right\rceil . \tag{3.13}$$

Only the portion of the deficit that can be replenished from renewable generation is considered in the final sizing of the storage system.

(a) One rack, metal frames used to hold and organize 15 battery modules within the storage container

(b) Storage container (2.4 m height) with 20 racks compared to 1 person

Figure 3.8: Narada container (Rack Type 3), 15 modules × 20 racks, 1.13 m³ / 2120 kg [50]

3.3. Summary

Table 3.3 highlights the key values that serve as a summary, key synthesis, and main takeaway after reading this chapter. It provides at a glance the most important results, input, and boundary parameters from the performed calculations and system configurations.

Table 3.3: Summary of methodology steps and key values

Step	Description	Key Values
Bridge operation load	Determined annual demand, lighting dominant annually.	$E_{\text{op,max}}$ = 37.4 MWh/yr
De-icing demand	Calculated from surface energy balance using hourly KNMI (2024) data; heating active 326 hours below 2°C (Appendix C).	E_{th} = 222.3 MWh/yr $q_{\text{flux, winter}}$ = 208 W/m²
IJ-water temperature	Calculated via the heat balance in Appendix D (radiation, convection, evaporation, conduction); defines heating boundary.	T_{air} = -5°C to 33°C T_{water} = 5°C to 20°C
System configurations	Defined as direct (foundation piles, aquathermal) and indirect (ATES) systems for seasonal storage.	$L_{\text{direct, short}}$ = 96.5 m $L_{\text{direct, long}}$ = 468.5 m L_{indirect} = 600 m
Deck and flow parameters	Determined prefab deck with in situ cast 480 hydronic loops; flow based on pipe diameter and velocity.	Q_{total} = 0.12 m³/s T_{inflow} = 16°C to 18°C
Renewable inputs	Calculated Solar PV and small vertical wind turbines as main electricity sources.	E_{PV} = 203.5 MWh/yr E_{wind} = 73.8 MWh/yr
Energy performance	Evaluated via hydraulic–thermal relations, energy/peak coverage, embodied CO_2, and storage sizing.	$\eta_{\text{pump, direct}}$ = 40% $\eta_{\text{pump, indirect}}$ = 70% $COP_{\text{heat pump,direct}}$ = 3 $E_{\text{container, storage}}$ = 2.68 MWh

4

Direct Heating Systems

This chapter outlines the methodology, verification process, thermal results, energy coverage performance, and environmental assessment for the three direct heating systems. The analysis focuses on evaluating the systems' heating supply characteristics. The corresponding electrical heat pump and pumping loads and required battery storage are calculated and are summarized for all systems in the final section. This part addresses:

- *Sub-question 5: What are the Oostbrug's heating supply, thermal operational electricity load, and required battery storage for a direct heating system?*

4.1. System 1: Water-Based Pile

The system shown utilizes submerged pile foundations as a direct heat exchange interface with the IJ River. Within the reinforced concrete piles as shown in Figure 4.1 (or a tubex pile), a network of heat exchanger pipes circulates a heat transfer fluid that absorbs thermal energy through conduction with the surrounding river water. During operation, the water temperature of the IJ acts as a thermal reservoir. The fluid loops carry this absorbed heat to a heat pump, where the energy and temperature is upgraded and distributed through a circulation pump to embedded deck tubes for de-icing. Conversely, excess heat can be rejected back to the river when cooling is required in summer. System performance depends strongly on the river's seasonal temperature fluctuations, thermal conductivity of the pile materials as steel or concrete casing and grout within the pile, and hydraulic losses within the closed-loop circuit.

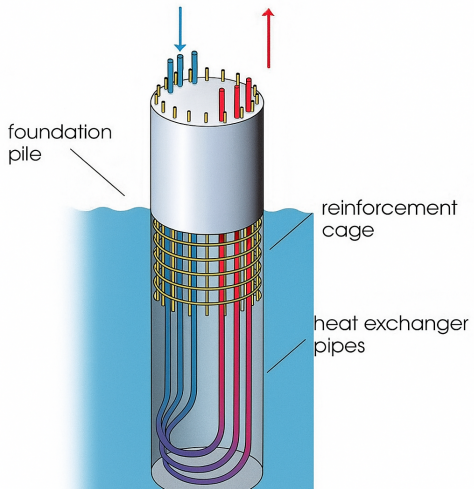

Figure 4.1: System 1: Water-based pile heat exchange system [35]

4.1.1. Methodology

Parameter choices, ΔT limits, and loss coefficients are stated, along with how per-pile performance scales to the pillar inventory. Figure 2.2 and Figure 4.2 illustrates the structural layout of the bridge foundation, highlighting the 'Kelderpijler' and 'Pijler hoofdoverspanning' pile sections and their submersion in the IJ River. These schematics provide an understanding of the lengths and locations of the water-based pile systems.

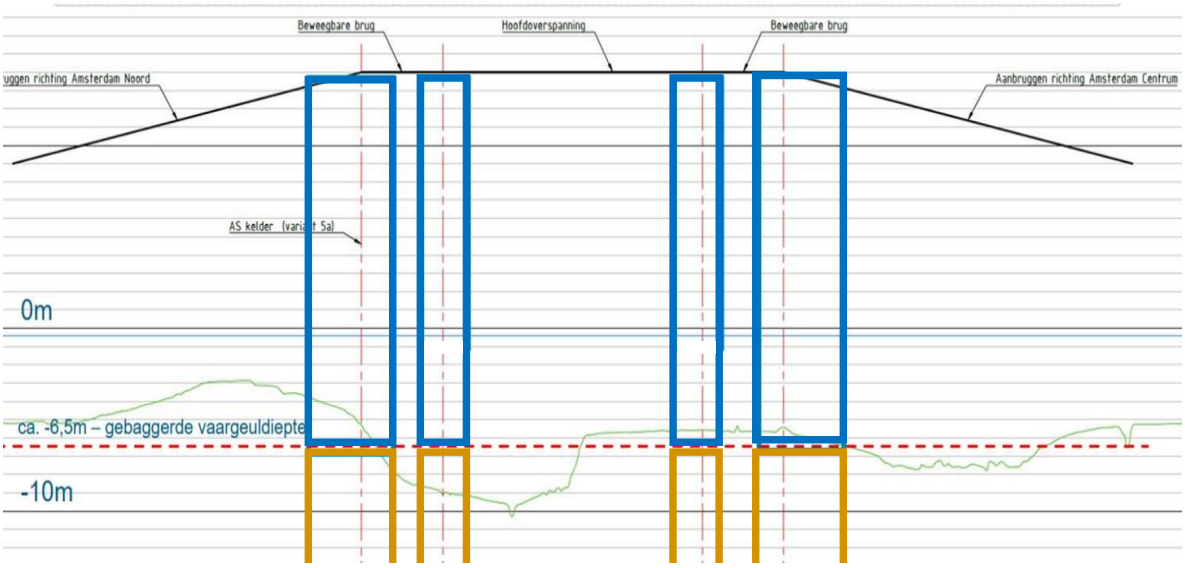

Figure 4.2: System 1: Submerged foundation piles in the IJ River [34]

The net heat transfer of the pile system has been evaluated for two different fluid media. Using the parameters in Table 4.1, the heat gained by the water is determined from the temperature difference between the fluid medium and the IJ river, with a maximum exchange of 3 °C to ensure ecological balance and prevent stress on the water environment [44]. For a water-only medium, extraction is possible only when river water is at least 6 °C to avoid freezing, while a 42% propylene glycol medium allows extraction at lower river water temperatures. Heat losses to the surrounding air and water are calculated as the product of their respective loss coefficients and the pile length exposed to each medium. The net heat transfer is then obtained by subtracting these losses from the gross heat gained (Equation 4.2).

The total heat transfer of the system is calculated by multiplying the net heat transfer per pile by the total number of piles. In this assessment, prefabricated piles are selected instead of Tubex piles, since they require a greater number of units and therefore provide a larger overall exchange area. This choice ensures that the heat extraction potential is fully utilized, while also highlighting the influence of both the fluid medium and pile configuration on the system's overall performance.

Table 4.1: System 1: Model parameters for water-based pile sections

Parameter	Symbol	Value	Unit
Pile diameter	D	0.8	m
Length in water (direct-water section)	L_{water}	6.5	m
Overall U-value (water section)	U_{water}	25	$\mathrm{W\,m^{-2}\,K^{-1}}$
Loss per metre (water)	v_{water}	5	$\mathrm{W\,m^{-1}}$
'Pijler' Tubex piles sand layer 3	$N_{4\times12}$	48	–
'Pijler' Prefab piles sand layer 2	$N_{5\times20}$	100	–
'Kelder' Tubex piles sand layer 3	$N_{5\times7}$	35	–
'Kelder' Prefab piles sand layer 2	$N_{8\times11}$	88	–

For this system methodology, both water and glycol are set to a temperature difference of $3\,\mathrm{C}$ to ensure ecological balance [44] and prevent stress on the water environment:

- **Heat extracted from water:** Limited to $\Delta T \leq 3°\mathrm{C}$, only extracting heat from a water temperature of $6\,°\mathrm{C}$.
- **Heat input to the HP glycol loop:** Limited to $\Delta T \leq 3°\mathrm{C}$, only extracting heat from a water temperature of $4\,°\mathrm{C}$.

$$Q_{\text{water}} = A_{\text{water}}\, U_{\text{water}}\, \Delta T, \tag{4.1}$$

$$Q_{\text{netto,water}} = Q_{\text{water}} - Q_{\text{loss,water}}, \tag{4.2}$$

$$A_{\text{water}} = 2\pi \left(\frac{D}{2}\right) L_{\text{water}}, \tag{4.3}$$

where Q_{water} is the gross heat transfer from the water (W), A_{water} the heat exchange area in contact with the water (m^2), U_{water} the overall heat transfer coefficient (W/(m^2·K)), and ΔT the effective temperature difference between fluid and structure (K). $Q_{\text{netto,water}}$ denotes the net heat gain after accounting for losses $Q_{\text{loss,water}}$ (W), D the pile diameter (m), and L_{water} the immersed length in water (m).

Verification

The overall heat transfer coefficient (*U*-value) was determined using Basic heat and mass transfer from Mills [47] from a resistance model combining external convection, conduction through the concrete cover, and internal resistance of grout and pipe resulting in an overall coefficient of $U \approx 27$ W·m^{-2}·K^{-1}. To be on the safe side, in this method is chosen for an $U = 25$ W·m^{-2}·K^{-1}. Using typical values for river water at 10 °C flowing at 1 m·s^{-1} (due to the river water not being fully free convective water, but a small flow, the external water coefficient is above 1000 W·m^{-2}·K^{-1}) past a 0.8 m pile, this yields:

$$\frac{1}{U} = \frac{1}{h_{\text{water}}} + \frac{\delta}{k_{\text{conc}}} + \frac{1}{h_{\text{inside}}} \tag{4.4}$$

where h_{water} is the external convection coefficient ($h_{\text{water}} \approx 1500$ W·m^{-2}·K^{-1}), δ/k_{conc} the conduction resistance of the concrete cover ($\delta/k_{\text{conc}} \approx 0.080$ m^2·K·W^{-1}), and h_{inside} the internal resistance due to grout, pipe wall, and in-pipe convection ($h_{\text{inside}} \approx 150$ W·m^{-2}·K^{-1}) [47].

4.1.2. Thermal Results

Net heat transfer ranges and sensitivity to water temperature are presented, indicating where the concept is viable and where auxiliary measures are required. Results are presented for the highest combination of pile sections; the prefab piles until sand layer 2 (Table 4.1).

For both bridge lengths in Figure 4.3 and Figure 4.4 the water pile sections from the 'pijler' (Figure 4.3a) and the 'kelder' (Figure 4.4a) section do not deliver enough power to meet the maximum required deicing demand in January. Although for the 96.5-meter bridge deck length, with the glycol loop, small demand peaks can be covered.

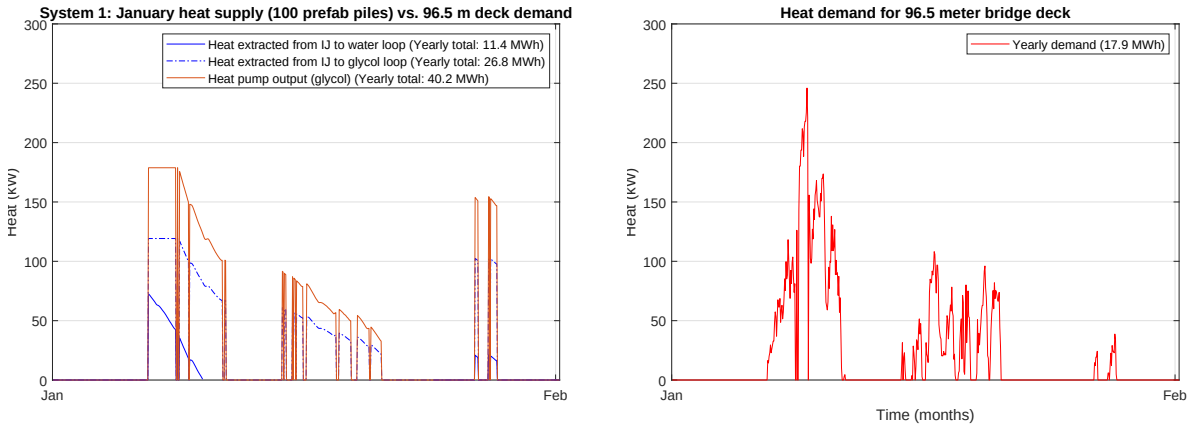

(a) Supply **(b)** Demand

Figure 4.3: System 1 January: 96.5 meters deck

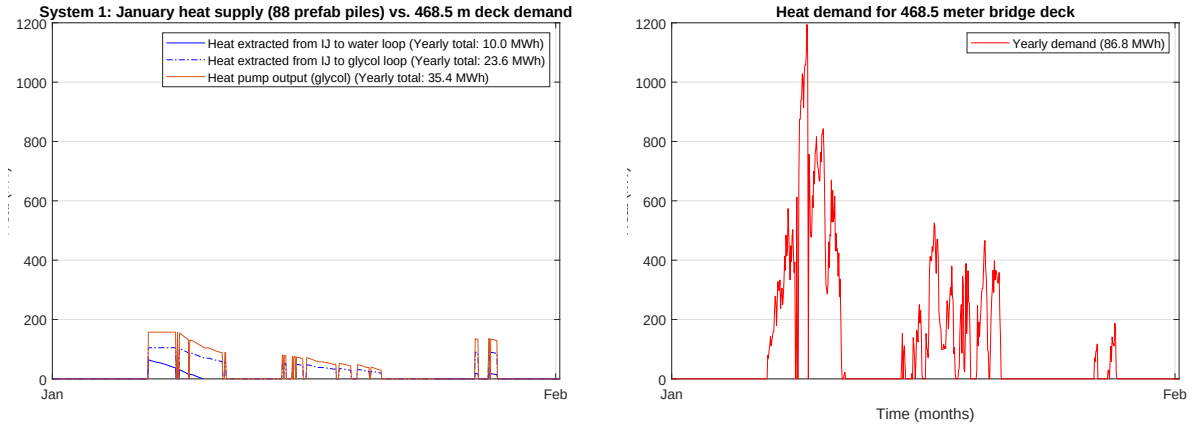

(a) Supply **(b)** Demand

Figure 4.4: System 1 January: 468.5 meters deck

Performance Assessment

Table 4.2 summarizes the energy and peak coverage. For the 96.5 meter deck, both the glycol and empowered heat pump systems provide sufficient energy coverage, while for the 468.5 meter deck none of the configurations meet the energy demand. In addition, none of the three system configurations achieves full peak coverage (a value above 1) at either deck length, at time of the peak demand.

Table 4.2: System 1: Energy and peak coverage fractions at two deck lengths

Deck	System	Energy	Peak
Short	Water loop	0.64	0.08
	Glycol loop	1.50	0.41
	Heat pump	2.25	0.62
Long	Water loop	0.12	0.01
	Glycol loop	0.27	0.08
	Heat pump	0.41	0.11

Embodied CO_2

For the piles equipped with a 6.5 meters water-exchange section, the embodied CO_2 of the HDPE U-loops was calculated using the first equation in Equation 3.10 explained in section 3.2. The effective pipe length L_{pipe} corresponds to two legs of 6.5 meters each, giving the per-pile contribution of 7.55 kg CO_2. Multiplying by the number of piles in each configuration yields the total embodied emissions.

For the total system configuration, both sides of the bridge are considered. This corresponds to two times 100 piles for the shorter deck length (96.5 m) and two times 88 piles for the longer deck length (468.5 m). The aggregated results are summarised in Table 4.3.

Table 4.3: System 1: Embodied CO_2 of HDPE U-loops for prefab piles

Configuration	**System**	**CO_2 (kg, both sides)**
Prefab 88 piles	6.5 m U-loops	1328
Prefab 100 piles	6.5 m U-loops	1510
Total	–	**2838**

4.2. System 2: Ground-based pile storage

Solar-recharged energy piles use energy piles to store heat in deeper soil layers during summer and extract it in winter for deck de-icing, as shown in Figure 4.5. The system in this chapter is treated as a geothermal-recharged system (without storing energy in summer), thus operates as a direct system with a fixed power output per pile length in the winter and constrained by pile foundation properties. Performance depends on pile depth, soil properties and ground temperatures. The fluid loops carry this absorbed heat from the subsurface close to the foundation pile to a heat pump close to the bridge deck, where the energy and temperature is upgraded and distributed through a circulation pump to embedded deck tubes for de-icing.

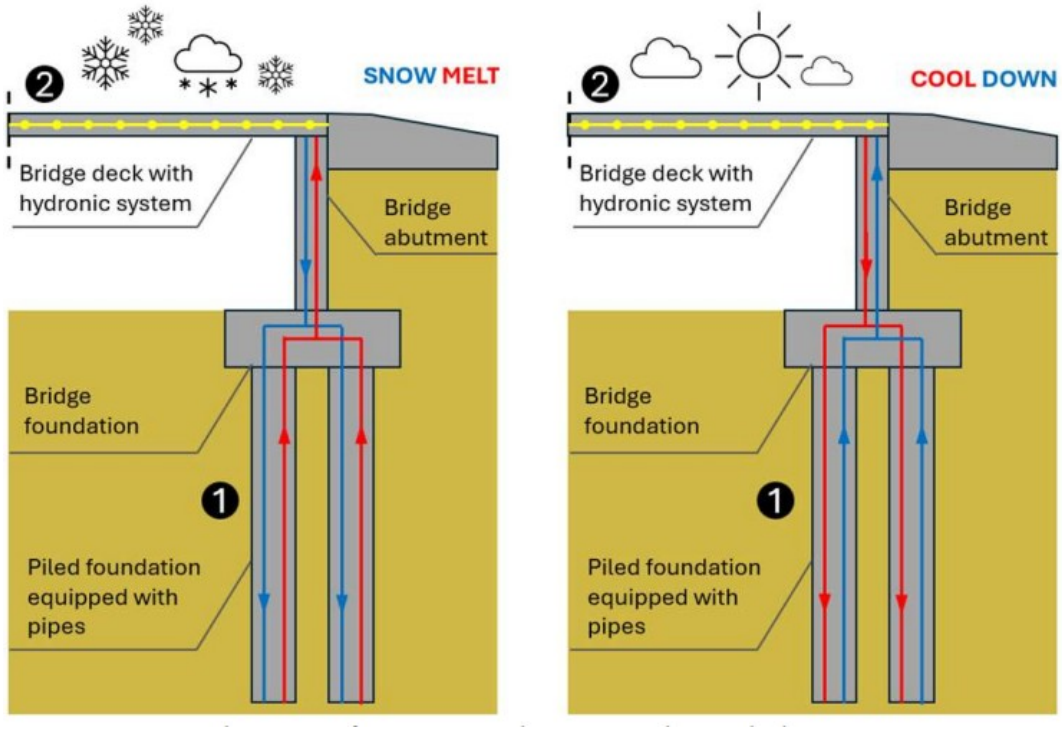

Figure 4.5: Solar-recharged energy pile, discharging (left) and charging from bridge deck (right) [60]

4.2.1. Methodology

The foundation piles in this system are assessed for both prefabricated (prefab) and screwed steel tube (tubex) pile configurations. The prefab piles extend down to the second sand layer, whereas the tubex piles penetrate deeper, passing through the second sand layer and the intervening clay layer to reach the third sand layer. Heat transfer rates for the upper sand layer (second sand layer), the clay layer, and the lower sand layer (third sand layer) are calculated by multiplying the heat yield per metre (p_{sand}= 50 W/m or p_{clay} = 30 W/m) by the segment length. These numbers are extracted from the Crux report [37], which investigates the subsurface quay walls in Amsterdam with clay and sand layers.

Table 4.4: System 2: Model parameters for ground-based pile sections

Parameter	Symbol	Value	Unit
Pile diameter	D	0.8	m
Total maximum pile length	L_{tot}	70	m
Length in water (direct-water section)	L_{water}	6.5	m
Soil length	$L_{\text{soil}} = L_{\text{tot}} - L_{\text{water}}$	63.5	m
Loss per metre (water)	v_{water}	5	$\mathrm{W\,m^{-1}}$
Loss per metre (sand)	v_{z}	5	$\mathrm{W\,m^{-1}}$
Loss per metre (clay)	v_{k}	3	$\mathrm{W\,m^{-1}}$
Heat yield per metre (sand)	p_{z}	50	$\mathrm{W\,m^{-1}}$
Heat yield per metre (clay)	p_{k}	30	$\mathrm{W\,m^{-1}}$
'Pijler' Tubex piles sand layer 3	$N_{4\times12}$	48	–
'Pijler' Prefab piles sand layer 2	$N_{5\times20}$	100	–
'Kelder' Tubex piles sand layer 3	$N_{5\times7}$	35	–
'Kelder' Prefab piles sand layer 2	$N_{8\times11}$	88	–

Total heat transfer is calculated by multiplying the net transfer per pile by the number of piles. For both Tubex piles (Figure 4.6 and Figure 4.7) and Prefab piles (Figure 4.8 and Figure 4.9), the same method applies. Equation 4.5 and Equation 4.6 show the calculation. The model parameters used for the calculations can be seen in Table 4.4. The equations are as follows:

$$Q_{\text{netto,Prefab,piles}} = Q_{\text{sand,layer2}} - Q_{\text{loss,Prefab}}, \tag{4.5}$$

$$Q_{\text{netto,Tubex,piles}} = Q_{\text{layer2,clay,layer3}} - Q_{\text{loss,Tubex}}, \tag{4.6}$$

$$Q_{\text{loss,Prefab}} = Q_{\text{loss,water}} + Q_{\text{loss,layer2}}, \tag{4.7}$$

$$Q_{\text{loss,Tubex}} = Q_{\text{loss,water}} + Q_{\text{loss,layer2}} + Q_{\text{loss,clay}} + Q_{\text{loss,layer3}} \tag{4.8}$$

where $Q_{\text{netto,Prefab,piles}}$ and $Q_{\text{netto,Tubex,piles}}$ are the net heat gains from the Prefab and Tubex pile configurations (W), respectively. $Q_{\text{sand,layer2}}$ and $Q_{\text{layer2,clay,layer3}}$ represent the gross heat extracted from the corresponding soil layers (W). $Q_{\text{loss,Prefab}}$ and $Q_{\text{loss,Tubex}}$ denote total heat losses for each configuration, composed of layer-specific losses: $Q_{\text{loss,water}}$, $Q_{\text{loss,layer2}}$, $Q_{\text{loss,clay}}$, and $Q_{\text{loss,layer3}}$ (all in W).

Tubex piles

Figure 4.6: Foundation: 48 Tubex steel piles (Ø 609/850 mm, NAP –70 m); footprint 9 × 29 m [34]

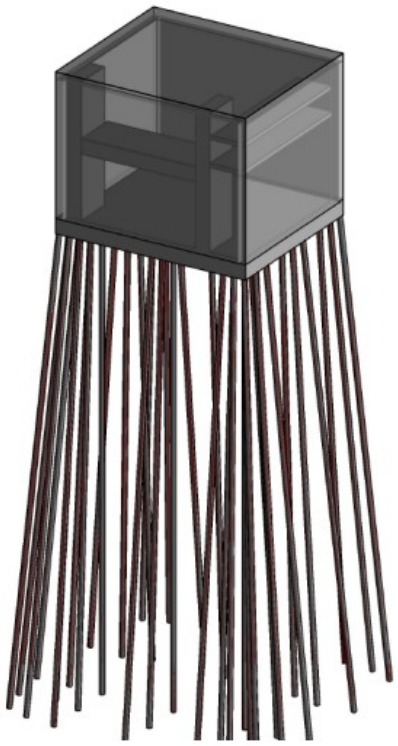

Figure 4.7: Foundation: 35 Tubex steel piles (Ø 609/850 mm, NAP –70 m); footprint 23 × 27 m [34]

Prefab piles

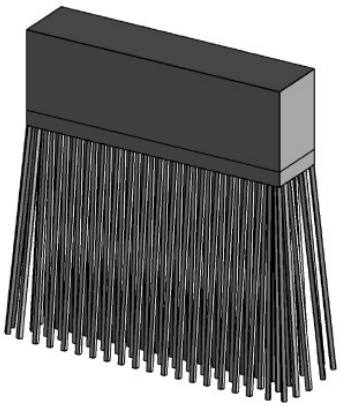

Figure 4.8: Foundation: 100 prefab concrete piles (NAP –27 m); footprint 8 × 36 m [34]

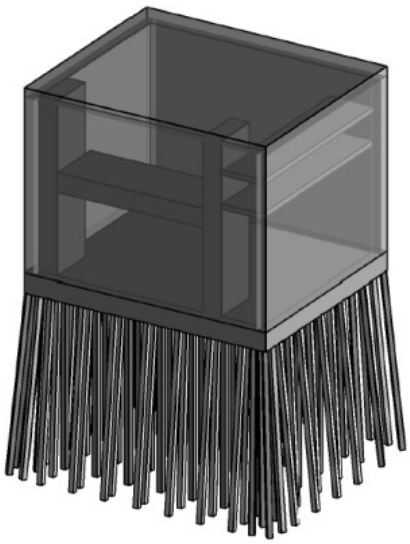

Figure 4.9: Foundation: 88 prefab concrete piles (NAP –27 m); footprint 22 × 27 m [34]

Verification

In subsection 2.2.2 described in the energy piles section, the energy output per pile length ranges from 20 to almost 60 W/m, as shown in Figure 2.8. In Peng Zhang et al. [78], outcomes from the energy

output vary from 27 up to 63 W/m, confirming the rough range of 20 to 60 W/m. This range is highly dependent on the type of pile heat exchanger tube as described in subsection 2.2.2. In this section, only a single U-shape, a double U-shape (W-shape), and a spiral shape are named in ascending order of heat exchange efficiency. Peng Zhang et al. [78] performed a detailed design solution of not only the types mentioned above, but instead of parallel double shaped tube, also a series of double U-shape tubes, performing higher heat exchanges. Furthermore, the parallel double U-shape is extended to a triple and a fifth U-shape. Both scores are just below the spiral shape, around 45 to 54 W/m.

4.2.2. Thermal Results

Heat yields per layer and aggregate capacities are shown, highlighting trade-offs between performance and foundation configuration. In Figure 4.11, medium-high peak demand can be covered by the 48 Tubex piles in the 'pijler'. The 100 Prefab piles' power is approximately 30 kW smaller, but still covers a few peak demands.

Heat pumps are not required because the summer-recharged energy piles deliver adequate temperatures. However, installing heat pumps for the short deck length to increase output will require at least half of the input coming from electricity to maintain the maximum power demand. Resulting in a low COP value.

While in Figure 4.12, both pile types do not even cover the small peaks for the 468.5-meter-long bridge length. For both bridge lengths, the average heat extracted from the energy piles from the third sand layer is dominant.

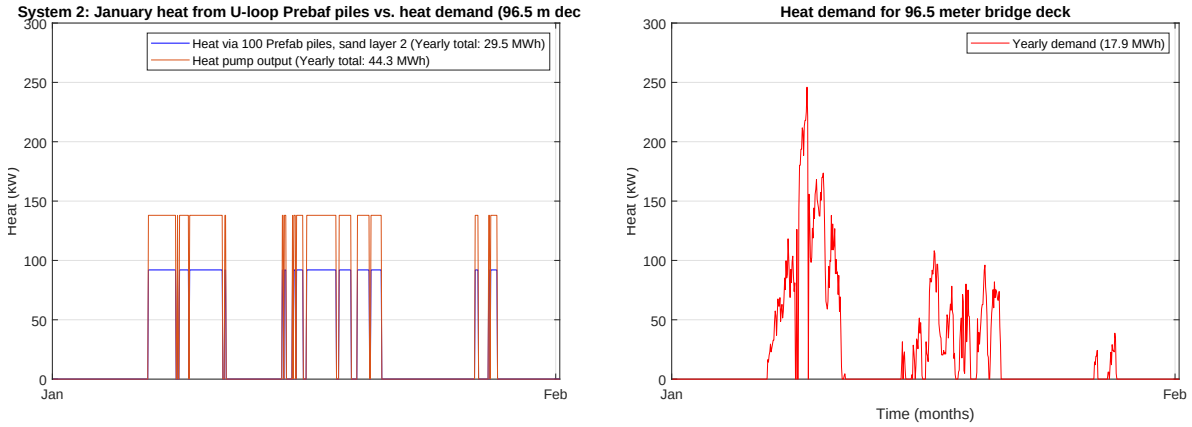

(a) Supply **(b)** Demand

Figure 4.10: System 2 January: Prefab, 96.5 meters deck

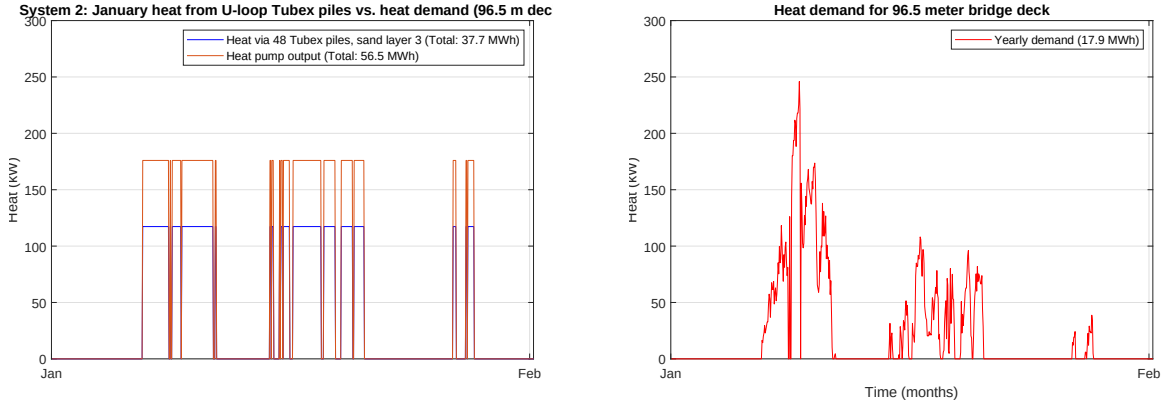

(a) Supply **(b)** Demand

Figure 4.11: System 2 January: Tubex, 96.5 meters deck

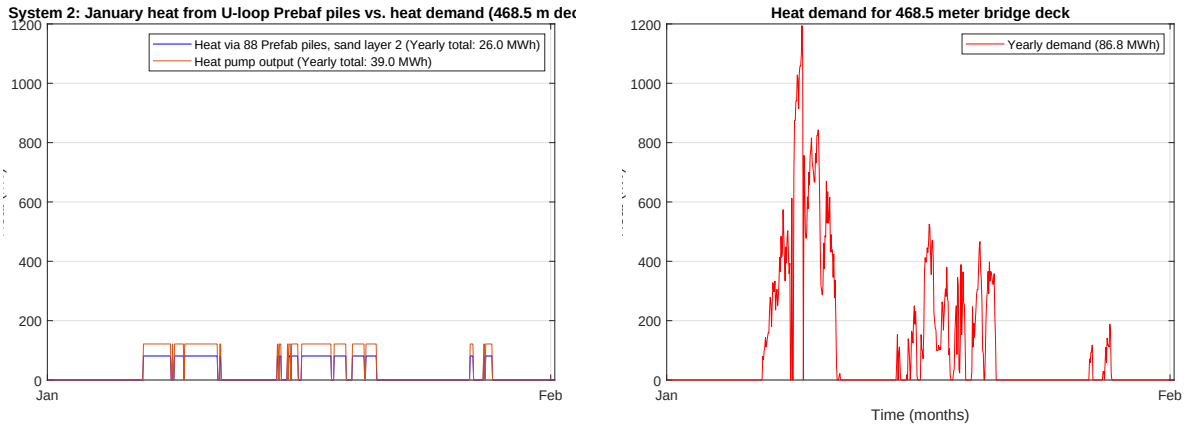

(a) Supply **(b)** Demand

Figure 4.12: System 2 January: Prefab, 468.5 meters deck

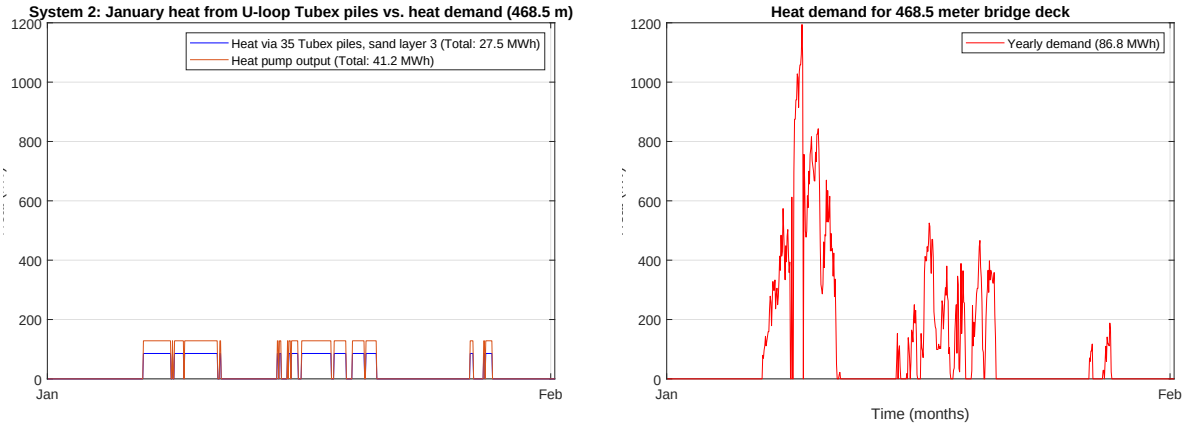

(a) Supply **(b)** Demand

Figure 4.13: System 2 January: Tubex, 468.5 meters deck

Performance Assessment

Table 4.5 summarizes the energy and peak coverage for System 2, comparing prefab and Tubex piles for both short and long deck lengths. For the short deck energy coverage, the systems meets the demand (a value above 1), in some configurations two or three times more than the demand. The peak coverage is for both deck lengths not achieved (a value under 1).

Table 4.5: System 2: Energy and peak coverage fractions at two deck lengths

Deck	System	Energy	Peak
Short	Prefab piles	1.65	0.37
	Prefab piles + HP	2.47	0.56
	Tubex piles	2.11	0.48
	Tubex piles + HP	3.16	0.72
Long	Prefab piles	0.30	0.07
	Prefab piles + HP	0.45	0.10
	Tubex piles	0.32	0.07
	Tubex piles + HP	0.48	0.11

Embodied CO_2

The piles are calculated over their full depth: $L = 21.2$ m for prefab piles and $L = 70$ m for Tubex piles. The embodied CO_2 of the HDPE U-loops was calculated using the first equation in Equation 3.10 explained in section 3.2. The effective pipe length L_{pipe} corresponds to two legs of 21.2 and 70 meters each, giving the per-pile contribution of respectively 21.4 kg CO_2 and 70.7 kg CO_2. Multiplying by the number of piles in each configuration yields the total embodied emissions.

For the total system configuration, both sides of the bridge are considered, where the Tubex and the Prefab configurations are compared. This corresponds to two times 48 Tubex piles for the shorter deck length (96.5 m) and two times 35 Tubex piles for the longer deck length (468.5 m). Similarly, for prefab piles, two times 100 piles and two times 88 piles are required. The aggregated results are summarised in Table 4.6.

Table 4.6: System 2: Embodied CO_2 of HDPE U-loops for Tubex and prefab piles

Configuration	**System**	**CO_2 (kg, both sides)**
Tubex 48 piles	70 m U-loops	6788
Tubex 35 piles	70 m U-loops	4950
Subtotal Tubex	–	**11,734**
Prefab 100 piles	21.2 m U-loops	4280
Prefab 88 piles	21.2 m U-loops	3766
Subtotal Prefab	–	**8046**

4.3. System 3: Aquathermal Energy

In this section, closed and open aquathermal concepts coupled to heat pumps are compared on extractable power and operational practicality under ecological ΔT constraints. Here, the closed configuration refers to heat exchangers directly placed in the IJ river, whereas in the previous section (section 4.1) the closed heat exchangers were integrated into the foundation piles, of which 6.5 m is submerged in the IJ river. The open aquathermal system pumps source water directly into the system through filters and a heat exchanger; a low-lift heat pump raises the supply temperature. Thereafter, water is discharged back. While closed systems keep the source water separate using a closed loop heat exchanger, thin plates placed in the water body, thereafter upgrading it by a heat pump and supplying the bridge deck tubes. Both are shown in Figure 4.14.

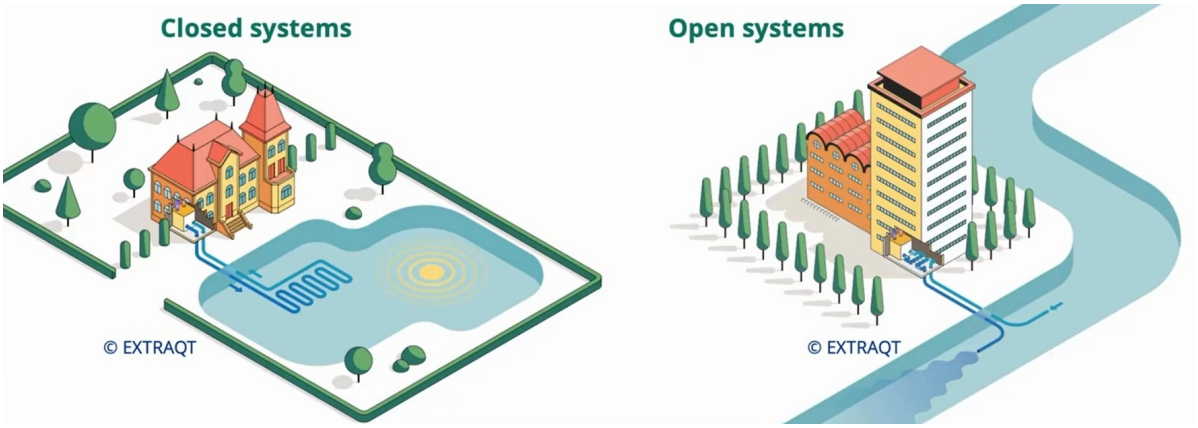

Figure 4.14: System 3: Closed vs. open aquathermal systems, heat exchange in- or outside water [19]

4.3.1. Methodology

The performance of closed and open aquathermal systems with heat pumps was modelled under the constraint of a maximum water temperature decrease of $\Delta T_{\text{max}} = 3\,^{\circ}\text{C}$, to ensure ecological balance and prevent stress on the water environment [44]. Negative temperature differences were set to zero. Both water and a glycol fluid are being looked into. The maximum required power is defined for the coldest water conditions coinciding with heating demand, ensuring complete coverage of the heating load by the heat pump.

- **Heat extracted from water:** Limited to $\Delta T \leq 3^{\circ}\text{C}$, only extracting heat from a water temperature of $6\,^{\circ}\text{C}$.
- **Heat input to the HP glycol loop:** Limited to $\Delta T \leq 3^{\circ}\text{C}$, only extracting heat from a water temperature of $4\,^{\circ}\text{C}$.

In closed aquathermal systems, glycol–water circulates in a sealed pipe loop that exchanges heat with the surface water. In open systems, only surface water is pumped, while any glycol mixture is confined to a secondary closed circuit separated by a heat exchanger.

For closed aquathermal systems a $1.8\,\text{kW}$ per cubic volume heat exchanger is used (Equation 4.9), and for open aquathermal systems $32.6\,\text{kW}$ per cubic volume heat exchanger is used (Equation 4.10) [44]. This difference in numbers is due to the efficiency of heat extraction of both systems. For an open system a much higher heat transfer coefficient and greater flow rate, thus more heat extraction is possible as described in subsection 2.2.2.

$$q_{\text{closed}} = \frac{1.8}{3} \cdot \Delta T \tag{4.9}$$

$$q_{\text{open}} = \frac{32.6}{3} \cdot \Delta T \tag{4.10}$$

where q_{closed} and q_{open} are the volumetric heat extraction rates for the closed and open aquathermal systems, respectively (kW/m^3), and ΔT is the limited temperature difference for water or glycol applied in the aquathermal system (K). The constants 1.8 and 32.6 represent the base heat extraction capacities (kW/m^3) at a reference temperature difference of $3\,^{\circ}\mathrm{C}$, with the factor $\frac{1}{3}$ scaling the heat extraction proportionally to the actual ΔT.

The amount of heat extracted by the glycol loop and the water loop is scaled proportionally to the actual temperature difference of the IJ river. If the water body is able to extract the maximum temperature difference of 3, the designed heat exchanger is able to deliver the required heat demand.

4.3.2. Thermal Results

Thermal inputs and outputs are reported in Figure 4.15. and Figure 4.16. Overall, the modeled aquathermal systems with a glycol loop, in combination with heat pumps, is capable of exceeding the defined heat demand under the given assumptions and boundary conditions in the legend.

The following results are taken from the graph, which has been zoomed in on January, as the direct peak heating demand must be met during this period, and the month provides a clearer view of the daily variations in heat demand.

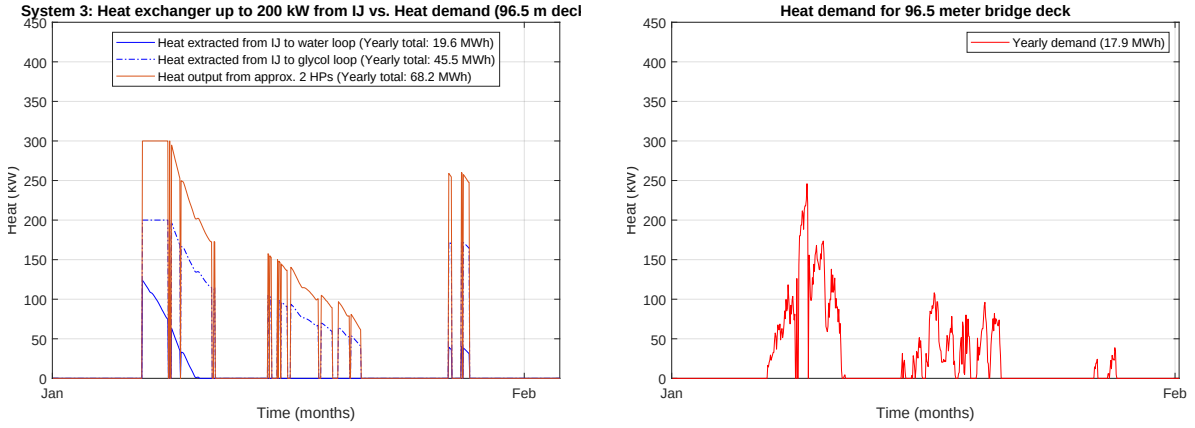

(a) Supply **(b)** Demand

Figure 4.15: System 3 January: 96.5 meters deck

For a deck length of 96.5 meters (Figure 4.15a) with a maximum heat exchanger delivering capacity of 200 kW, the required heat exchanger volumes are listed below. Heat pumps supply any remaining peak demand that the heat exchanger cannot cover.

- **Heat exchanger volumes:** 111 m^3 (closed system) and 6 m^3 (open system).
- **Total heat pump production:** $\sim$68 MWh from 2 heat pumps (COP = 3).
- **Peak demand (Jan–Feb):** almost fully met by the glycol upgraded with heat pumps, with only minor shortfalls in mid-January.

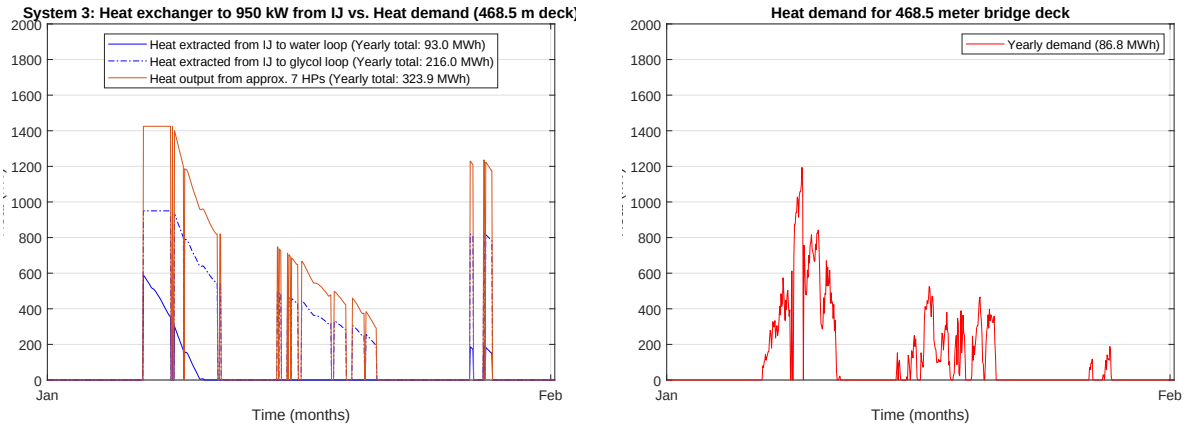

(a) Supply **(b)** Demand

Figure 4.16: System 3 January: 468.5 meters deck

For a deck length of 468.5 meters (Figure 4.16a) with a maximum heat exchanger delivering capacity of 950 kW, the required heat exchanger volumes are listed below. Heat pumps supply any remaining peak demand that the heat exchanger cannot cover.

- **Heat exchanger volumes:** 528 m^3 (closed system) and 29 m^3 (open system).
- **Total heat pump production:** $\sim$324 MWh from 7 heat pumps (COP = 3).
- **Peak demand (Jan–Feb):** almost fully met by the glycol upgraded with heat pumps, with only minor shortfalls in mid-January.

Verification

The graphs in the results section verify that glycol water can extract water at a lower temperature from the IJ river, so the orange dotted line is higher than the solid blue line, where the medium is only water. However, these lines must be parallel to each other because they extract heat from the same body of water (the IJ river).

The ratio of useful heating output to electrical energy input is the COP. The COP is set to 3, and the electrical energy used is the difference between the solid orange and dotted lines. When the heat pumps start to operate at about 300 kW output (Figure 4.15a), the graph shows an electrical input of 100 kW, yielding a COP of 3. This ratio is similar for the other moments in time while the heat pumps are running.

Performance Assessment

Table 4.7 presents the energy and peak coverage fractions at peak demand for System 3, comparing short and long deck lengths across the water loop, glycol loop, and heat pump.

Table 4.7: System 3: Energy and peak coverage fractions at two deck lengths

Deck	System	Energy	Peak
Short	Water loop	1.10	0.15
	Glycol loop	2.54	0.70
	Heat pump	3.82	1.04
Long	Water loop	1.07	0.15
	Glycol loop	2.49	0.68
	Heat pump	3.73	1.02

Embodied CO_2

The embodied CO_2 of the heat exchangers was calculated using the second equation in Equation 3.10, explained in section 3.2. with the required heat transfer area determined from the design load. At a representative load of $Q = 200$ kW, the closed HDPE system requires a much larger surface area than the open RVS system, resulting in higher embodied emissions. This difference becomes even more pronounced at $Q = 950$ kW.

For the total system configuration, both sides of the bridge are considered, corresponding to two heat exchangers of 200 kW for the shorter deck length (96.5 m) and two heat exchangers of 950 kW for the longer deck length (468.5 m). The aggregated results are summarised in Table 4.8, showing a total embodied CO_2 of 3.2 tons for the open RVS system and 10.2 tons for the closed HDPE system.

Table 4.8: System 3: Embodied CO_2 of open and closed heat exchangers

Configuration	**System**	**CO_2 (tons, both sides)**
Short deck (2x 200 kW)	Open RVS	0.55
Long deck (2x 950 kW)	Open RVS	2.63
Subtotal RVS	–	**3.18**
Short deck (2x 200 kW)	Closed HDPE	1.78
Long deck (2x 950 kW)	Closed HDPE	8.44
Subtotal HDPE	–	**10.22**

4.4. Electrical Loads with Battery Storage

This section presents the electrical load analysis for the three direct heating systems, considering the maximum heat output of the glycol-based configuration. The analysis includes both the pumping power and the heat pump electricity input, evaluated for two deck configurations: 96.5 m and 468.5 m. The results illustrate how the system performance varies with deck length and pile configuration, followed by an assessment of the corresponding seasonal power and energy needs. Finally, the section evaluates the battery storage requirements under solar and wind generation scenarios, highlighting the impact of system type and deck configuration on the overall electrical balance and storage capacity.

Results 96.5 Deck

For the given short deck configuration, the corresponding number of piles was 100 for System 1, 100 for System 2 prefab, and 48 for System 2 tubex. The required pumping powers were determined based on the relations presented in Equation 3.6 and Equation 3.7 from section 3.2. The volumetric flow rate was derived from the total maximal thermal power and fluid properties per system, while a fixed pressure drop was assumed for each circuit to represent the hydraulic resistance of the loop. In glycol loops, the working fluid is around 40% propylene glycol, where the viscosity increases compared to a water medium at the same temperature; therefore, the lambda and pressure difference are higher than in water loops [47]. The pump and heat pump power for the water-based systems are not presented, as the analysis focuses on the working fluid with the highest performance potential.

For the four configurations (Sys 1; Sys 2-Prefab; Sys 2-Tubex; Sys 3) in Figure 4.17 the corresponding volumetric flow rates were 35 m³/h, 25 m³/h, 35 m³/h, and 57 m³/h, respectively, calculated by Equation 3.6 . These values were used to calculate the electrical power required to circulate the fluid through each system loop as seen in Figure 4.17.

For the energy piles, converting this flow rate to liters per minute and determining it per pile, via Javed and Spitler [38] , the pressure drops per loop are determined and set to 5 kPa, 5 kPa, and 40 kPa, respectively.

For the aquathermal system, the open-loop configuration was selected as the reference case, as it represents the most critical pressure drop scenario. A pressure drop of 60 kPa was chosen with its corresponding volumetric flow rate. High flow velocities prevent operation within the low-velocity fouling zone [3].

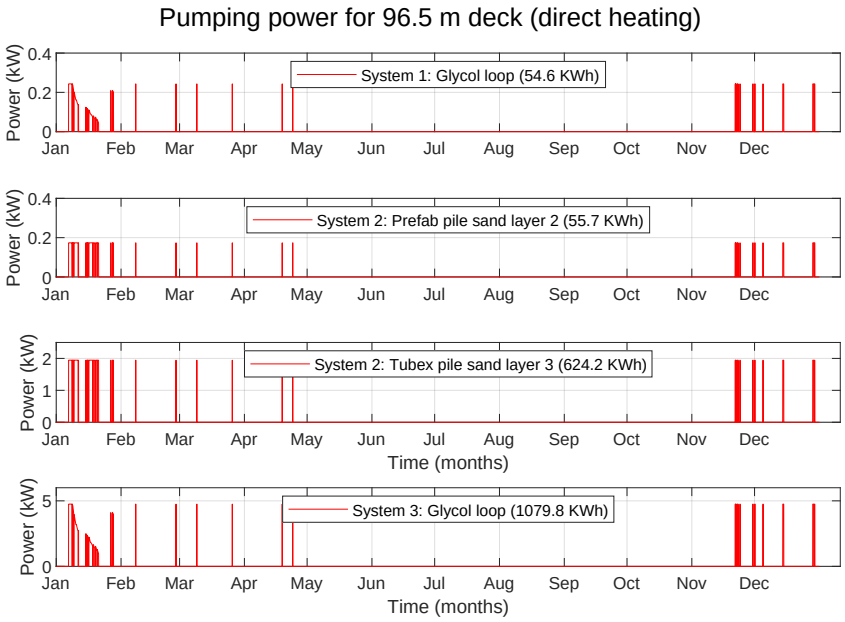

Figure 4.17: System 1-3: Pumping power 96.5 meters deck

The total heat pump electricity input for the short deck configuration was calculated using Equation 3.7, based on the available hourly thermal energy from each system. This dynamic approach determines the heat pump's total electrical input over time, reflecting the varying heat supply in Figure 4.18.

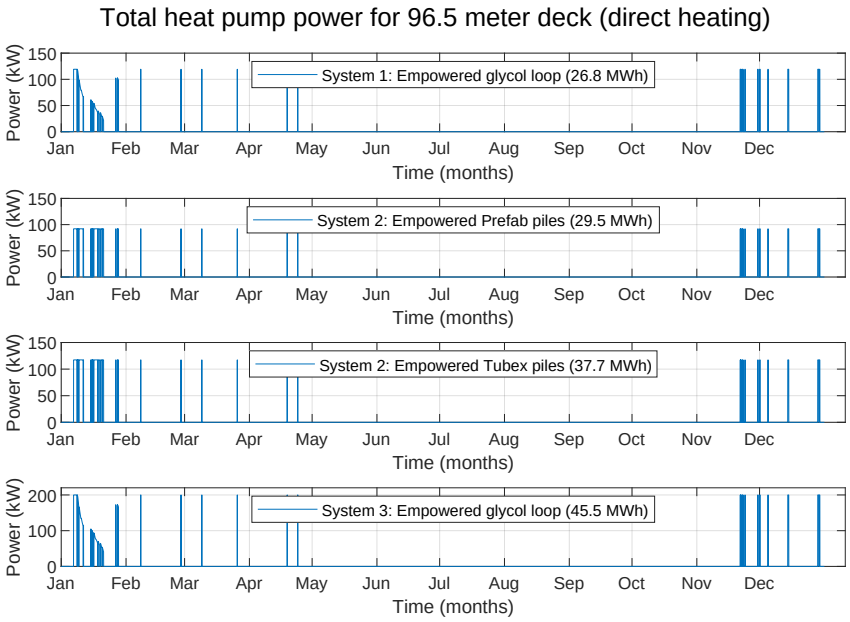

Figure 4.18: System 1-3: Heat pumping power 96.5 meters deck

Results 468.5 Deck

The same approach was applied to the long deck configuration, with 88 piles for System 1, 88 for System 2 (Prefab), and 35 for System 2 (Tubex). Volumetric flow rates were 30, 23, 24, and 273 m³/h for Systems 1–3, respectively, and pressure drops were assumed equal to the short deck (5, 5, 40, and 60 kPa). These parameters were used to calculate the pumping power shown in Figure 4.19.

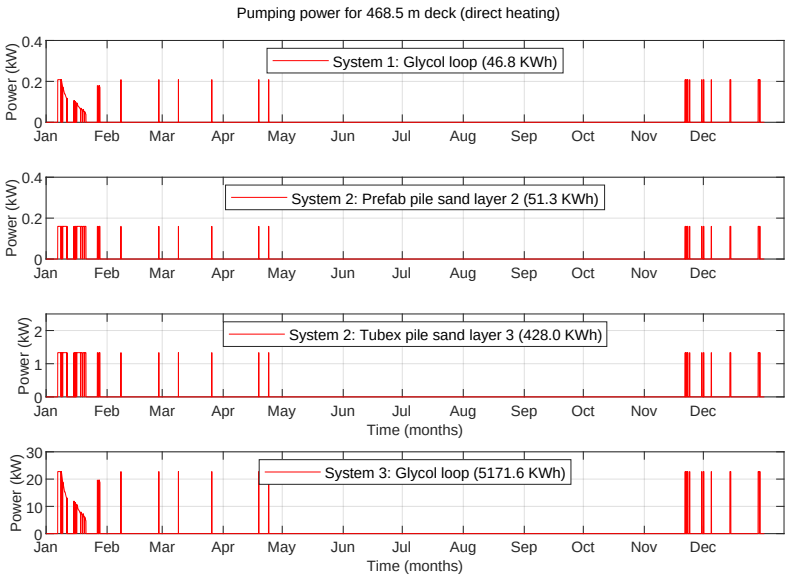

Figure 4.19: System 1-3: Pumping power 468.5 meters deck

The total heat pump electricity input for the long deck configuration was calculated using Equation 3.7, based on the available thermal energy from each system at every hourly time step. This provides a time-dependent estimate of the electrical demand corresponding to the varying heat supply from the systems in Figure 4.20.

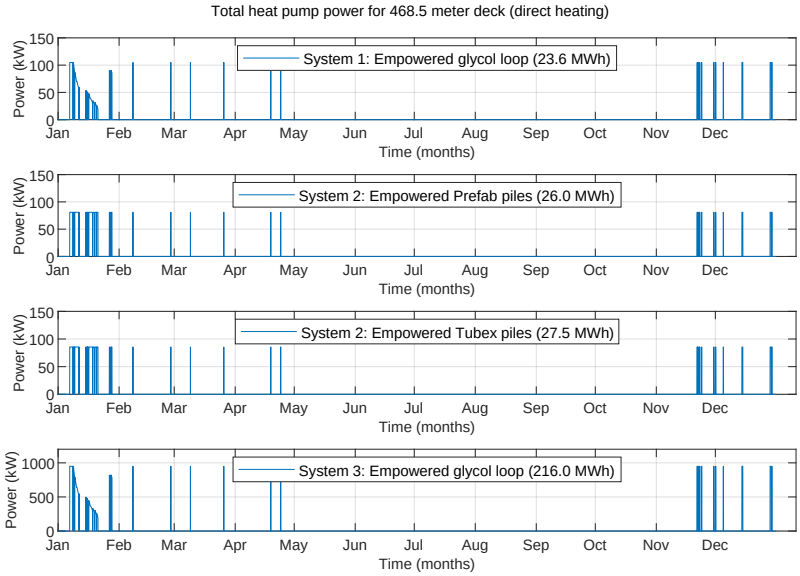

Figure 4.20: System 1-3: Heat pumping power 468.5 meters deck

For both the electricity consumption of the heat pump and pump power, System 3 consistently shows the highest demand, while System 1 requires the lowest across all configurations.

Table 4.9 presents the seasonal power and energy needs for Systems 1–3 under direct heating operation. The results show that System 3 consistently exhibits the highest winter power and energy demand for both deck configurations, while System 1 shows the lowest. For the longer deck, all systems demonstrate slightly lower energy requirements compared to the short deck configuration, except for System 3, which scales proportionally with the increased deck length.

Table 4.9: System 1-3: Seasonal power and energy requirements

System & Scope	Winter P (kW)	Winter E (MWh)
Short Length — pumping + HP		
System 1	120.25	26.855
System 2 Prefab	90.18	29.556
System 2 Tubex	121.95	38.324
System 3	204.80	46.580
Long Length — pumping + HP		
System 1	105.21	23.647
System 2 Prefab	80.17	26.051
System 2 Tubex	86.30	27.928
System 3	953.00	221.172

Battery System Sizing

Table 4.10 and Table 4.11 present the deficit summaries for Systems 1–3, comparing the short and long deck configurations under both solar and wind generation scenarios. The results show that System 3 consistently experiences the highest electrical deficits, requiring the largest battery capacity, with up to 13 containers for the short deck and 59 containers for the long deck configuration. In contrast, Systems 1 and 2 exhibit considerably lower deficits, typically requiring 7–8 containers for the short deck and 6–9 containers for the long deck.

Additionally, meeting the bridge service load of 33.5 MWh/year for the double-leaf bridge type requires 9.1 containers (rounded to 10), assuming 2.68 MWh per container.

Table 4.10: System 1-3: Renewable deficit and storage at deck length 96.5 meters deck

	Solar deficit		Wind deficit		Solar / Wind
System	**kW**	**MWh**	**kW**	**MWh**	**Containers**
System 1	119.2	26.2	119.2	24.9	**8 / 7**
System 2 (Prefab)	92.0	28.9	92.0	27.6	**8 / 8**
System 2 (Tubex)	117.3	37.0	117.3	35.7	**10 / 10**
System 3	200.0	44.8	200.0	43.5	**13 / 12**
Bridge service loads					**10**

Table 4.11: System 1-3: Renewable deficit and storage at deck length 468.5 meters deck

	Solar deficit		Wind deficit		Solar / Wind
System	**kW**	**MWh**	**kW**	**MWh**	**Containers**
System 1	104.9	23.0	104.9	21.7	**7 / 6**
System 2 (Prefab)	81.0	25.4	81.0	24.1	**7 / 7**
System 2 (Tubex)	85.5	26.8	85.5	25.5	**8 / 7**
System 3	958.0	215.3	950.0	214.0	**59 / 59**
Bridge service loads					**10**

5

Indirect Heating System

This chapter outlines the methodology, heat storage, verification process, thermal results, energy coverage performance, and environmental assessment for the two indirect heating systems. Each side of the river is equipped with an ATES system supplying half of the bridge deck, corresponding to a total bridge deck area of 7,200 m². The analysis focuses on evaluating the systems' heating supply characteristics. The corresponding electrical pumping loads and required battery storage are calculated and are summarized for all systems in the final section. This part addresses:

- *Sub-question 6: What are the Oostbrug's heating supply, heat storage capacity, thermal operational electricity load, and required battery storage for an indirect heating system?*

5.1. System 4: Seasonal Storage with Aquathermal Energy

Summer surface-water heat capture combined with ATES is assessed for delivering winter de-icing heat reliably and efficiently. Chosen is for an open loop system configuration as shown in Figure 5.1, since these systems preferably occur for systems with a demand above 300 kW [44]. Heat from the IJ water is stored in the warm well via a heat exchanger in summer and used to heat the deck in winter.

Figure 5.1: System 4: Open-loop aquathermal system with filters, heat exchanger, and outflow [6]

The ATES system design is carried out according to the following steps:

1. **System dimensioning** — Sized to ensure extractable energy covers yearly bridge demand.
2. **Summer recharging** — Heat replenished via exchanger with balanced flows within well capacity.
3. **Operational setpoints** — Well and exchanger temperatures controlled for seasonal performance.
4. **Design parameters** — Doublets defined with parameters for summer and winter operation.

5.1.1. Methodology

The thermal power extracted from the IJ river was calculated based on the water temperature, the reference setpoint ($18\ ^\circ\mathrm{C}$), the volumetric flow rate, and the thermophysical properties of the heat transfer fluid. The calculation assumes a constant flow velocity of 600 m3/h.

The calculation follows a conditional approach to determine the temperature difference depending on the measured water temperature:

- If $T_{\text{water}} > 18\ ^\circ\mathrm{C}$, then $\Delta T = T_{\text{water}} - 18$.
- If $\Delta T > 3$, it is capped at 3 °C to avoid overestimation of extractable energy.
- If $T_{\text{water}} \leq 18\ ^\circ\mathrm{C}$, then $\Delta T = 0$, and no energy is recovered.

The thermal power is computed using:

$$Q = \dot{V} \cdot \rho \cdot c \cdot \Delta T \tag{5.1}$$

where $\dot{V}$ is the volumetric flow rate (m^3/s), ρ the density of water (kg/m^3), c the specific heat capacity of water (J/(kg·K)), and ΔT the temperature difference between the inlet and outlet (°C).

Heat Storage

The ATES is dimensioned based on the storage capacity of the maximum energy supplied by the aquathermal source, depending on the set temperature and flow conditions. From the moment the system starts operating, the initial stored heat in the aquifer (MWh) must be sufficient to meet one side of the the bridge's demand. During summer, the warm well is recharged by the IJ river until at least the required energy volume is restored.

To ensure that, during summer recharging from 18 °C on the aquathermal side, the warm well temperature in the aquifer approaches this value, the flow rate and temperature difference of the aquathermal and ATES loops are scaled so that the heat exchanger transfers equal power (Equation 5.1). On the aquathermal side, the available temperature differential is set to 3 °C, as defined above. Because the temperature differential on the aquifer side is set to two times the aquathermal side, its flow rate must be proportionally lowered on the aquifer side. Based on equal heat balance of Equation 5.1, this results in an ATES flow rate of 218.2 m³/h during summer operation to get close to the aquathermal extraction temperature.

Additionally, at each side of the heat exchanger, either a loop enters or leaves the side, the temperature difference between the two heat exchanger sides should remain about 2 °C, ensuring efficient heat transfer [21]. Thus, the minimum temperature entering the heat exchanger in the aquathermal loop in summer is 18 °C; then the injection temperature leaving the heat exchanger to the hot well in the aquifer loop should be around 16 °C. A smaller temperature difference indicates better performance of the heat exchanger.

The setpoints for the cold and warm wells are set at 12 °C and 17.5 °C, respectively. The warm well will operate within a range of 16 °C to 19 °C, as the entering temperature on the aquathermal side of the heat exchanger is expected to be between 18 °C and 21 °C.

The maximum required power for half the bridge deck is 1.53 MW, assumed on both sides an ATES system. In the schematic overview of the subsurface at KNSM-eiland (South) and Hamerkwartier (North) in Appendix E (Figure E.1), the aquifer thickness is taken as 40 m. The remaining parameter inputs for the ATES system are given in the following Table 5.1:

Table 5.1: System 4: Parameter inputs for ATES system supplying 600 meters deck

Parameter	Value	Unit
Specific heat water c_w	4200	J/kgK
Warm well temperature T_w	17.5	°C
Cold well temperature T_c	12	°C
Max thermal power $Q_{th,max}$	1.53×10^6	W
Max velocity u_{max}	3	m/h
Aquifer thickness h	40	m
Well radius r_w	0.2	m
Density of water ρ_w	1000	kg/m^3
Density of aquifer ρ_a	2640	kg/m^3
Heat capacity aquifer c_a	710	J/kgK
Viscosity μ	4.67×10^{-4}	Pa·s
Permeability k	1.48×10^{-12}	m^2

5.1.2. Thermal Results

From the water body above 18°C, a total energy amount of 1297.4 MWh can be extracted (Figure 5.2, which is above de 111.2 MWh required for half of the bridge deck.

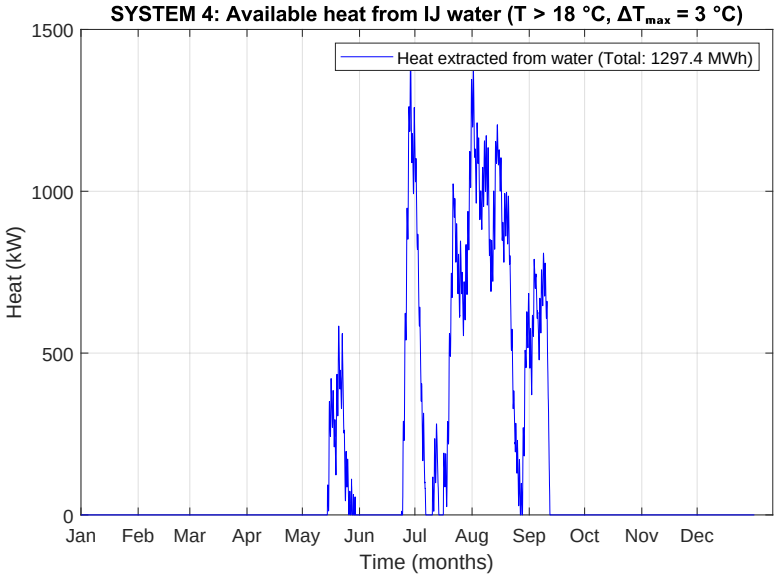

Figure 5.2: System 4: Extracted aquathermal energy from the IJ River

Serving the demand in wintertime, with an average temperature difference of approximately 5.5°C between the ATES wells, the required flow rate of 238.3 m3/h is calculated by Equation 5.1 with 1.53 MW required demand per storage system.

Using the 1297.4 MWh of energy extracted from the water body for each storage system on both sides, and the input parameters from Table 5.1, the ATES properties were calculated according to the formulas in subsection 2.2.3, with the results shown in Table 5.2. The required number of doublets is two.

In Table 5.3, the system parameters for summer and winter seasons are summarized for half of the bridge, with its corresponding in and outlet temperatures from the sides of the heat exchanger. The total flow required on the aquifer side during summertime recharging is below the maximum flow rate of the two doublets. Thus, the aquifer loop can to flow with 218.2 m^3/h to equally fill the doublets on both sides of the river with 1297.4 MWh.

Table 5.2: System 4: ATES results for one storage unit supplying 600 meters deck

Calculated	Value	Unit
maximum heat storage Q_{th}	12.98×10^8	Wh/year
Volume ATES	56164.5	m^3/year
Required flow rate $\dot{V}_{\text{req}}$	238.3	m^3/h
Maximum flow rate $\dot{V}_{\text{max}}$	150.8	m^3/h
Thermal radius R_{th}	31.65	m
Length L	94.94	m
Surface-to-volume ratio A/V	0.08	m^{-1}
Aspect ratio L/R	1.26	–
Required number of doublets	1.58	–

Table 5.3: System 4: System performance for Aquathermal and ATES loops at 600 meters deck

Season	Side	T_{in} (°C)	T_{out} (°C)	ΔT (K)	Flow (m^3/h)	Power (MW)	Energy (MWh)	Notes
Summer	Aquathermal	18–21	15–18	1–3	600	≈ 1.40	1297.4	Warm well recharge
	Aquifer	12.0	16–19	4–7	≈ 218.2	≈ 1.40	1297.4	Cooling the IJ river
Winter	Bridge Deck	10.0	15.5	5.5	238.3	1.53	111.2	Cold well recharge
	Aquifer	17.5	12.0	5.5	238.3	1.53	111.2	Heating bridge

The total energy captured in summer potentially exceeds the heat demand required in winter, suggesting that the system could meet annual heating needs, as shown in Figure 5.3. This represents the maximum storage capacity for one system with two doublets. Both the north and south sides will each have such a storage system.

However, the storage operation is not fully balanced throughout the year, as the warm well is recharged more than the cold well during winter. During summer, the warm well is replenished by the IJ River until at least the required energy volume is restored.

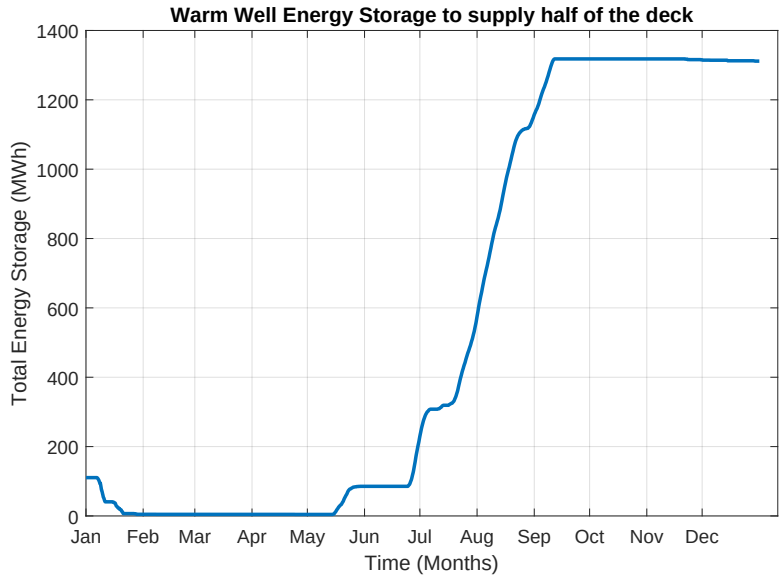

Figure 5.3: System 4: Cumulative aquathermal energy stored in aquifer for 600 meters deck

Verification

The peak extraction of Figure 5.2 is the first of July, which corresponds to the highest water temperature, as shown in Figure 3.2 from section 3.2, slightly above 20°C. The thermal power is calculated as

$$Q \;=\; \frac{600\,\mathrm{m^3/h}}{3600} \cdot c_p \cdot \Delta T \;\approx\; 1400\,\mathrm{kW}, \tag{5.2}$$

where $\Delta T \approx (20 - 18)\,^{\circ}\mathrm{C}$.

Performance Assessment

Table 5.4 shows the energy and peak coverage fractions for System 4, representing the entire bridge deck with ATES.

Table 5.4: System 4: Energy and peak coverage fractions

Deck	System	Energy	Peak
Entire	ATES	11.67	1.00

Embodied CO_2

The embodied CO_2 of the system has been quantified for both the open (RVS) heat exchanger and the ATES storage system. For the aquathermal heat exchanger, the embodied emissions were calculated using the general relation in the second equation in Equation 3.10, explained in section 3.2. The heat transfer area obtained from the heat load. The design capacity of $Q \approx 1400$ kW yields a required heat transfer area of 16.1 m^2. With material parameters of $\rho_A = 20$ kg/m^2 and $EF = 6.0$ kg CO_2/kg, the resulting embodied emissions are approximately 1.94 tons of CO_2 (Table 5.5).

For the ATES system, the storage capacity is designed at 1,297.4 MWh. Based on life-cycle emissions of 83 gCO_2/kWh$_{th}$, of which 14% is attributed to the construction phase (section 2.4), the embodied emissions are estimated at 15.1 tons of CO_2 (Table 5.5).

When combined, the aquathermal heat exchanger and the ATES system result in total embodied emissions of about 17.0 tons of CO_2. For both sides of the bridge demand, this doubles to approximately 34 tons of CO_2, highlighting the embodied footprint associated with system deployment.

Table 5.5: System 4: Embodied CO_2 emissions for open heat exchanger and ATES system

Component	Capacity/Design Basis	Embodied CO_2 (tons)
Open RVS heat exchanger	$Q \approx 1400$ kW	1.94
ATES storage system	1,297.4 MWh	15.10
Total (one side)		**17.04**
Total (both sides)		**34.08**

5.2. System 5: Seasonal Storage with Bridge Deck Energy

For this system configuration, the bridge deck functions as a summer collector to recharge storage, as shown in Figure 5.4. This is transferred via a heat exchanger to the ATES warm well. The stored heat is later used to warm the deck in winter. With solar radiation and duration throughout the year from the KNMI data [41] .

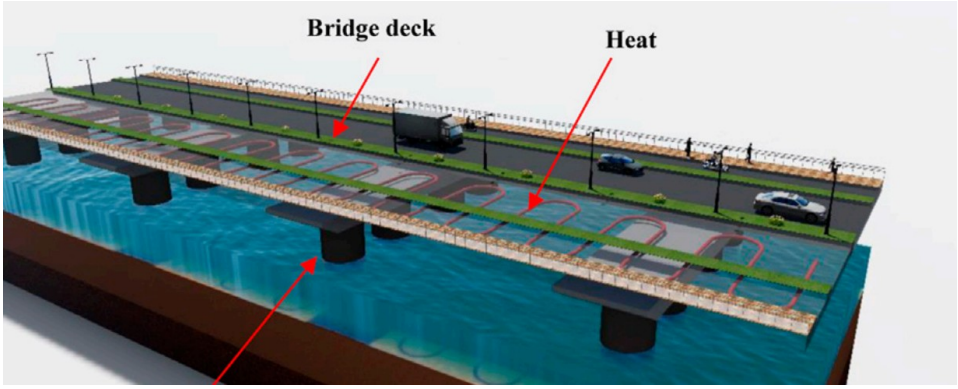

Figure 5.4: System 5: hydronically heated bridge deck tubes layout [78]

The ATES system design is carried out according to the following steps:

1. **System dimensioning** — Sized to ensure extractable energy covers yearly bridge demand.
2. **Summer recharging** — Heat replenished via exchanger with balanced flows within well capacity.
3. **Operational setpoints** — Well and exchanger temperatures controlled for seasonal performance.
4. **Design parameters** — Doublets defined with parameters for summer and winter operation.

5.2.1. Methodology

The temperature difference (Equation 5.3) is a function of the solar radiation on the bridge deck surface between 400 W/m2 and 1200 W/m2, solar energy collector efficiency of the bridge deck approximately set to 35% [74], the sun duration hours divided by the flow rate of the deck tube. Accordingly, the heat gain (Equation 5.4) was calculated with a flow rate of 30 m^3/h.

The temperature difference is computed as:

$$\Delta T = \frac{Q_{\text{rad}} \cdot A \cdot \eta \cdot t_{\text{rad}}}{\dot{V} \cdot \rho \cdot c} \tag{5.3}$$

and the thermal solar gain is given by:

$$Q_{\text{gain}} = \dot{V} \cdot \rho \cdot c_{\text{p}} \cdot \Delta T \tag{5.4}$$

where Q_{rad} is the available solar energy radiation (W/m^2), A the surface area of the bridge deck (m^2), η the solar energy collector efficiency of the bridge deck, t_{rad} the duration of solar radiation (h), $\dot{V}$ the volumetric flow rate (m^3/s), ρ the density of water (kg/m^3), and c_p the specific heat capacity of water (J/(kg·K)).

Heat Storage

The ATES is dimensioned based on the storage capacity of the maximum energy supplied by the bridge source, depending on the solar radiation, efficiency, and flow conditions. From the moment the system starts operating, the initial stored heat in the aquifer (MWh) must be sufficient to meet one side of the bridge's demand. During summer, the warm well is recharged by the bridge deck's concrete until at least the required energy volume is restored.

To ensure that, during summer recharging with a temperature difference calculated from Equation 5.3 on the bridge deck side, the warm well temperature in the aquifer approaches this value, the flow rate and temperature difference of the bridge deck and ATES loops are scaled so that the heat exchanger transfers equal power (Equation 5.4). On the bridge deck side, the available temperature differential is set to the average of Equation 5.3, as defined above. The temperature differential on the aquifer side is set similar to the bridge deck side. Thus, the flow rate on both side of the loops connected by the heat exchanger will be the same. This results in an aquifer flow rate of 30 m³/h during summer operation, similar to that set for the bridge deck tubes above.

Additionally, at each side of the heat exchanger, either a loop enters or leaves the side, the loops should remain approximately 2 °C “further away” from each other [21]. A smaller temperature difference indicates better performance of the heat exchanger.

The maximum required power for half the bridge deck is 1.53 MW, assumed on both sides an ATES system. In the schematic overview of the subsurface at KNSM-eiland (South) and Hamerkwartier (North) in Appendix E, the aquifer thickness is taken as 45 m. The remaining parameter inputs for the ATES system are given in the following Table 5.6:

Table 5.6: System 5: Parameter inputs for ATES system supplying 600 meters deck

Parameter	Value	Unit
Specific heat water c_w	4200	J/kgK
Max thermal power $Q_{th,max}$	1.53×10^6	W
Max velocity u_{max}	3	m/h
Aquifer thickness h	45	m
Well radius r_w	0.2	m
Density of water ρ_w	1000	kg/m^3
Density of aquifer ρ_a	2640	kg/m^3
Heat capacity aquifer c_a	710	J/kgK
Viscosity μ	4.67×10^{-4}	Pa·s
Permeability k	1.48×10^{-12}	m^2

5.2.2. Thermal Results

Figure 5.5 presents the temperature differences extracted from half the bridge deck using the parameters in Equation 5.3. Although the average extracted temperature is slightly above 8 °C, a value of 8 °C is defined for the aquifer’s well difference based on the bridge deck heat exchanger average.

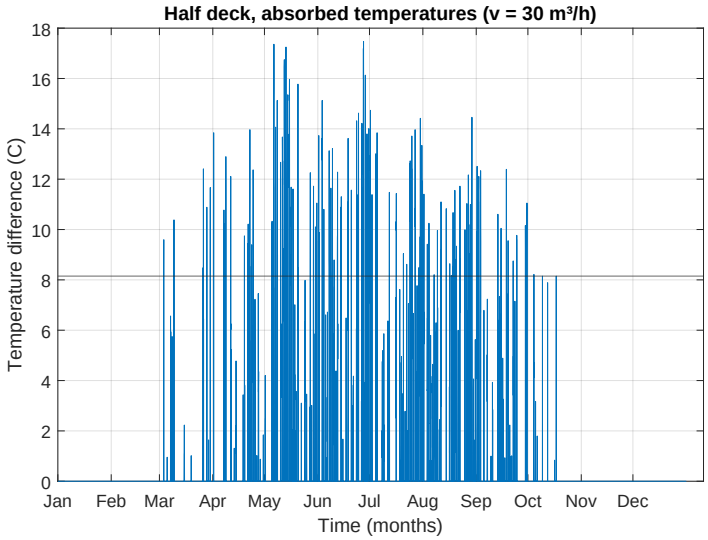

Figure 5.5: System 5: Solar collection temperature variation over 600 meters deck

The total energy theoretically extracted of 635.1 MWh from half of the bridge deck is shown in Figure 5.6, supporting the logic that higher radiation levels result in higher temperature differentials, indicating that thermal energy gain is strongly dependent on solar input. This exceeds the required 111.2 MWh yearly heating demand per half deck, ensuring sufficient capacity for seasonal storage.

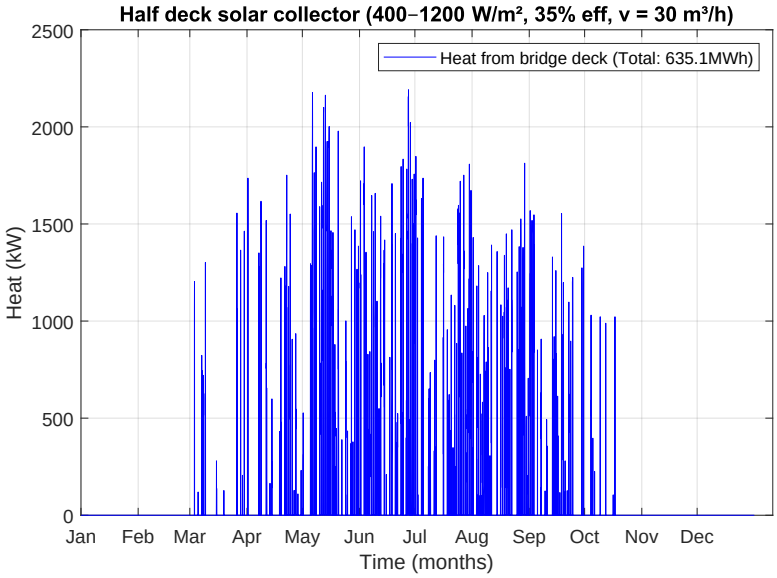

Figure 5.6: System 5: Solar collection over 600 meters deck

The setpoints for the cold and warm wells are set at 13°C and 21°C, respectively. With the temperature differential set to 8°C, the cold well set to the ground temperature will result in an average temperature of 21°C in the warm well.

Serving the demand in wintertime, with an average temperature difference of approximately 8°C between the ATES wells, the required flow rate of 163.8 m3/h is calculated by Equation 5.4 with 1.53 MW required demand per storage system on one side of the river.

Using the 635.1 MWh of energy extracted from half of the bridge, for each storage system on both sides, and the input parameters from Table 5.6, the ATES properties were calculated according to the formulas in subsection 2.2.3, with the results shown in Table 5.7. The required number of doublets per side of the river is one.

Table 5.7: System 5: ATES results for one storage unit supplying 600 meters deck

Calculated	Value	Unit
maximum heat storage Q_{th}	6.35×10^8	Wh/year
Warm well temperature T_w	21	°C
Cold well temperature T_c	13	°C
Volume ATES	18901.8	m^3/year
Required flow rate $\dot{V}_{\text{req}}$	163.8	m^3/h
Maximum flow rate $\dot{V}_{\text{max}}$	169.6	m^3/h
Thermal radius R_{th}	17.3	m
Length L	51.9	m
Surface-to-volume ratio A/V	0.15	m^{-1}
Aspect ratio L/R	2.60	–
Required number of doublets	0.97	–

In Table 5.8, the system parameters for summer and winter seasons are summarized for half of the bridge, with its corresponding in and outlet temperatures from the sides of the heat exchanger. The total flow required on the aquifer side during summertime recharging (30 m^3/h) is below the maximum flow rate of the doublet system (169.6 m^3/h). Thus, the aquifer loop can flow with 30 m^3/h to equally fill the doublet on both sides of the river with 635.1 MWh.

Table 5.8: System 5: System performance for Hydronic tubes and ATES loops at 600 meters deck

Season	Side	T_{in} (°C)	T_{out} (°C)	ΔT (K)	Flow (m^3/h)	Power (MW)	Energy (MWh)	Notes
Summer	Bridge deck	≈ 33.2	≈ 41.2	8	30.0	0.28	635.1	Warm well recharge
	Aquifer	13.0	21.0	8	30.0	0.28	635.1	Cooling bridge
Winter	Bridge Deck	11.0	19	8	163.8	1.53	111.2	Cold well recharge
	Aquifer	21.0	13.0	8	163.8	1.53	111.2	Heating bridge

The total energy captured in summer potentially exceeds the heat demand required in winter, suggesting that the system could meet annual heating needs, as shown in Figure 5.7. This represents the maximum storage capacity for one system with two doublets. Both the north and south sides will each have such a storage system.

However, the storage operation is not fully balanced throughout the year, as the warm well is recharged more than the cold well during winter. During summer, the warm well is replenished by the bridge deck its solar collector until at least the required energy volume is restored.

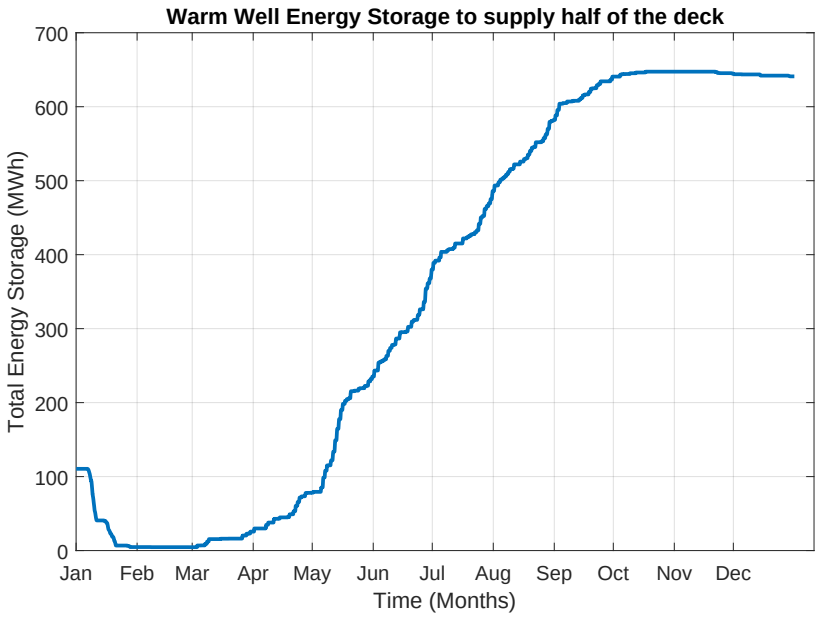

Figure 5.7: System 5: Cumulative aquathermal energy stored in aquifer for 600 meters deck

Verification

The highest peak extraction of approximately 1700 kW from Figure 5.8b corresponds to almost a temperature difference 14 C as shown in Figure 5.8a. The extracted thermal energy can be estimated and verified as

$$Q = \frac{30\,\mathrm{m}^3/\mathrm{h}}{3600} \cdot c_p \cdot \Delta T \cdot t \approx 1700\,\mathrm{kW}, \tag{5.5}$$

where $\Delta T \approx 14\,^{\circ}\mathrm{C}$ is the average temperature difference and $t = 3.5\,\mathrm{h}$ is the extraction duration.

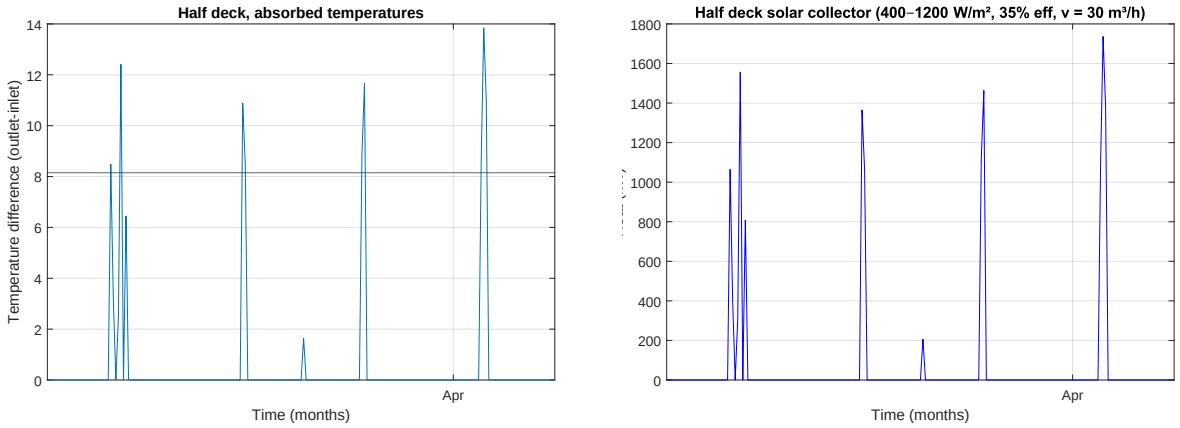

(a) Temperature difference over moments in time.

(b) Power over moments in time.

Figure 5.8: System 5: Solar collection and temperature variation over bridge deck in April

Performance Assessment

Table 5.9 summarizes the energy and peak coverage fractions for System 5, covering the entire bridge deck with ATES.

Table 5.9: System 5: Energy and peak coverage fractions

Deck	System	Energy	Peak
Entire	ATES	5.72	1.00

Embodied CO_2

The embodied CO_2 has also been determined for the case where only an ATES system is required. In this configuration, the storage capacity on one side of the bridge is 635.1 MWh. Using the same life-cycle emission factor of 83 gCO_2/kWh_{th}, with 14% allocated to the construction phase (section 2.4), the embodied emissions amount to 7.4 tons of CO_2 (Table 5.10).

As this system excludes the aquathermal heat exchanger, the embodied emissions are solely attributed to the ATES installation. For both sides of the bridge, this results in a total of 14.8 tons of CO_2.

Table 5.10: System 5: embodied CO_2 emissions for ATES system

Component	Capacity/Design Basis	Embodied CO_2 (tons)
ATES storage system	635.1 MWh	7.36
Total (one side)		**7.36**
Total (both sides)		**14.72**

5.3. Electrical Loads with Battery Storage

For the summer aquathermal loop side, the pumping power was calculated using Equation 3.7 with a fixed pressure drop of 60 kPa, similar to direct heating system 3 [3]. For the aquifer storage (ATES) loop, the pressure drop was determined using Equation 3.6 for a single well and doubled to represent a doublet, based on the flow rate, aquifer thickness, and properties defined in Table 5.1 and Table 5.2.

As shown in Figure 5.9 with corresponding flow rates, the highest pumping power occurs in summer, with 45.1 MWh for warm charge on the aquathermal side and 60.6 MWh for cold discharge on the aquifer loop side, while the winter operation requires only 4.3 MWh and is the same on both cold charging and warm discharge sides of the heat exchanger (bridge deck loop and aquifer loop).

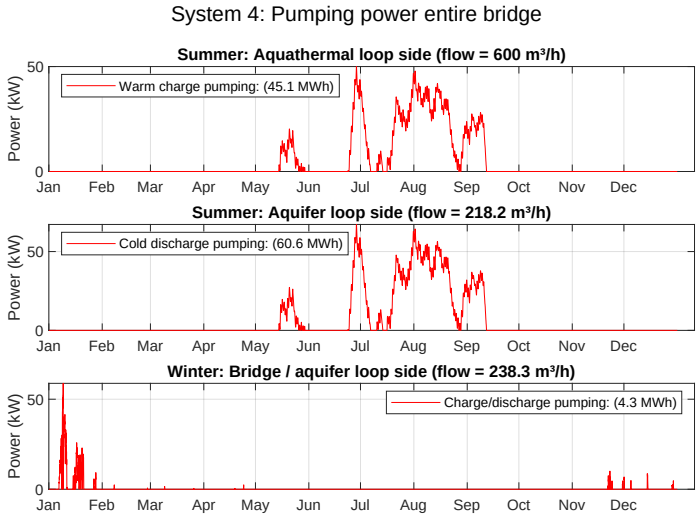

Figure 5.9: System 4: Seasonal pumping power for entire deck length

For System 5, pumping power was calculated using Equation 3.7 and Equation 3.6, with pressure losses doubled to represent a doublet. Based on the parameters in Table 5.6 and Table 5.7, flow rates of 30.0 m³/h (summer) and 163.8 m³/h (winter) result in annual pumping energies of 2.4 MWh and 2.8 MWh, respectively, as shown in Figure 5.10.

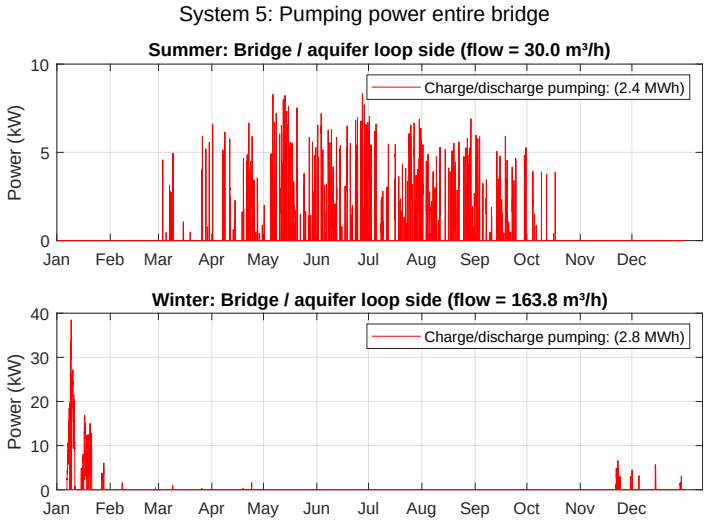

Figure 5.10: System 5: Seasonal pumping power for entire deck length

Table 5.11 summarizes the seasonal pumping power and energy demand for Systems 4 and 5. The results show that the highest energy consumption occurs during summer operation for System 4, with 45.1 MWh for the aquathermal loop and 60.6 MWh for the aquifer loop. In winter, the pumping demand is significantly lower, with 4.3 MWh for System 4 and 2.8 MWh for System 5. Overall, System 5 demonstrates the lowest total pumping energy across both seasons, compared to the aquathermal–aquifer setup of System 4.

Table 5.11: System 4-5: Seasonal power and energy requirements

System & Scope	Winter P (kW)	Winter E (MWh)	Summer P (kW)	Summer E (MWh)
Entire Bridge — pumping				
System 4 (Aquathermal, Summer)	–	–	50	45.1
System 4 (Aquifer, Summer)	–	–	65	60.6
System 4 (Bridge/Aquifer, Winter)	57	4.3	–	–
System 5 (Bridge/Aquifer, Summer)	–	–	7.5	2.4
System 5 (Bridge/Aquifer, Winter)	38	2.8	–	–

Battery System Sizing

Table 5.12 presents the deficit summary for Systems 4 and 5 under solar and wind generation scenarios. The results show that during summer recharging, the aquathermal and aquifer cases of System 4 require the largest battery storage capacities, with 8–11 and 11–15 containers, respectively, reflecting their higher seasonal energy deficits. During winter operation, the required storage decreases significantly to only 2 containers. System 5 shows negligible deficits during summer (≤ 0.7 MWh, equivalent to at most one container).

Additionally, meeting the bridge service load of 33.5 MWh/year for the double-leaf bridge type requires 9.1 containers (rounded to 10), assuming 2.68 MWh per container.

Table 5.12: System 4-5: Renewable deficit and storage at full deck length

	Solar deficit		Wind deficit		Solar / Wind
Case	**kW**	**MWh**	**kW**	**MWh**	**Containers**
System 4 — Aquathermal, summer	48.1	28.2	45.8	37.6	**8 / 11**
System 4 — Aquifer, summer	64.6	38.8	62.3	52.6	**11 / 15**
System 4 — Winter	58.8	4.0	41.6	2.6	**2 / 1**
System 5 — Summer	0.0	0.0	6.6	0.7	**0 / 1**
System 5 — Winter	38.5	2.6	23.0	1.3	**1 / 1**
Bridge service loads					**10**

Part III – Evaluation and Discussion

6

Comparative Analysis and Sensitivity Results

6.1. Cross-System Assessment Comparison

The results evaluate the feasibility of a self-sufficient energy system for the Oostbrug, aiming to supply both de-icing and auxiliary loads using renewable electricity (PV and wind), thermal sources (aquathermal and ground-based systems), and seasonal storage through ATES and batteries. Five system configurations were simulated and assessed, summarized in Table 6.1. Performance was measured by the annual *energy-coverage* (the fraction of yearly demand met) and the *peak-coverage* during the winter design hour. Direct-heating systems were evaluated for a short bridge deck section of 96.5 m and a long section of 468.5 m, while the indirect ATES-based systems were assessed for 600 m deck. Electricity demand was balanced with PV and wind generation supported by containerized Li-ion storage. In addition, embodied CO_2 emissions were estimated for the heat-exchange subsystems and ATES construction. Key results are presented in Table 6.2 and Table 6.3. This part addresses:

- *Sub-question 7: Which system setup and control strategy ensures full energy and peak coverage, and what embodied emissions result from its construction?*

Table 6.1: Summary of heating systems Systems 1–5

System	Name
1	Water-Based Pile
2	Ground-Based Pile Storage
3	Aquathermal Energy
4	Seasonal Storage with Aquathermal Energy
5	Seasonal Storage with Bridge Deck Energy

Overall, the direct heating systems (Systems 1–3) show that several configurations can cover the yearly energy requirement, particularly for the short deck, but only one configuration meets the design peak demand. In all cases, glycol loops outperform water loops for both energy and peak coverage. System 3, designed specifically to meet the required thermal demand, combines aquathermal heat exchange with glycol loops and heat pumps. Representing a different approach from Systems 1 and 2, which depend on the number of bridge piles. It is also the only direct system that achieves peak coverage for both the short and long decks. The indirect heating systems (Systems 4 and 5), which incorporate ATES, consistently meet the peak demand for the full bridge deck and exceed annual energy needs by large margins: System 4 provides roughly 11.7 times the required energy, while System 5 provides about 5.7 times.

Looking in more detail, System 1, based on water submerged pile foundations, meets the annual energy demand for the short deck only when equipped with glycol loops or heat pumps, but fails to achieve

peak-coverage in any variant. The long deck configurations of System 1 do not meet either requirement. System 2, based on ground energy piles, achieves the annual energy target for the short deck (with values ranging between 1.65 and 3.16), but also falls short of peak coverage. Its long deck variants perform poorly on both indicators. By contrast, System 3 with heat pumps succeeds in meeting both annual and peak demand for both short and long decks (short deck: energy coverage 3.82, peak 1.04; long deck: energy 3.73, peak 1.02), confirming that this system is designed adequately to deliver the necessary winter de-icing capacity. Among the indirect systems, System 4, which integrates ATES with open aquathermal recharge, achieves an energy coverage of 11.67 and a peak coverage of 1.00. System 5, where ATES is recharged through the bridge deck itself, achieves an energy coverage of 5.72 with the same peak coverage of 1.00.

The number of battery containers required varies considerably between systems. For the short deck, most configurations require between 7 and 13 containers, depending on the balance of PV and wind. For the long deck, similar values are observed, except for System 3, where the higher heat pump electricity demand results in a need for around 59 containers. For the ATES systems, container requirements vary, with System 4 needing for the total system between 21 and 27 containers, while System 5 requires only one or two containers.

Table 6.2: Summary of coverages with required renewable battery containers per system

System	Deck	Subsystem	Energy	Peak	Containers (Solar/Wind)
1	Short	Water loop	0.64	0.08	
		Glycol loop	1.50	0.41	
		Heat pump	2.25	0.62	8 / 7
	Long	Water loop	0.12	0.01	
		Glycol loop	0.27	0.08	
		Heat pump	0.41	0.11	7 / 6
2	Short	Prefab piles	1.65	0.37	
		Prefab piles + HP	2.47	0.56	8 / 8
		Tubex piles	2.11	0.48	
		Tubex piles + HP	3.16	0.72	10 / 10
	Long	Prefab piles	0.30	0.07	
		Prefab piles + HP	0.45	0.10	7 / 7
		Tubex piles	0.32	0.07	
		Tubex piles + HP	0.48	0.11	8 / 7
3	Short	Water loop	1.10	0.15	
		Glycol loop	2.54	0.70	
		Heat pump	3.82	1.04	13 / 12
	Long	Water loop	1.07	0.15	
		Glycol loop	2.49	0.68	
		Heat pump	3.73	1.02	59 / 59
4	Entire	ATES + aquathermal	11.67	1.00	21 / 27
5	Entire	ATES	5.72	1.00	1 / 2
Bridge service loads					**10**

The embodied CO_2 assessment shows that System 4, which combines open stainless-steel heat exchangers with ATES, embodies the highest emissions at 34.08 t for the full deck. System 5, consisting of ATES only, embodies 14.72 t, roughly half of System 4. Among the direct systems, System 3 with open RVS exchangers embodies 3.18 t, while closed HDPE exchangers reach 10.22 t. System 2's Tubex piles with deep U-loops (70 m) embody 11.74 t, while shallower U-loops (21.2 m) account for 8.04 t, excluding the pile materials (tubex and prefab) from this analysis. System 1 with short U-loops (6.5 m) shows the lowest emissions at 2.84 t. These results confirm that pile depth and material choice of the heat exchangers are the main determinants of embodied CO_2.

Table 6.3: Summary of embodied CO_2 emissions for all heat exchange systems full deck length

System	Subsystem	Embodied CO_2 (tons)
1	U-loops (6.5 m pile)	2.84
2	U-loop (70 m tubex pile)	11.74
	U-loop (21.2 m prefab pile)	8.04
3	Heat exchangers (open RVS)	3.18
	Heat exchangers (closed HDPE)	10.22
4	Open RVS + ATES	34.08
5	ATES only	14.72
	Conventional de-icing ($CaCl_2$ salt, 5.2 t/yr)	**7.9**

For systems 2 and 3, only one option is applied in practice: either Prefab or Tubex piles for system 2, and either open or closed heat exchangers for system 3. Both options are shown to reflect different coverage outcomes (prefab vs. Tubex) or design choices (open vs. closed aquathermal). The distinction in system 3 is only visible in the embodied CO_2 required for the heat exchanger size.

For conventional de-icing, approximately 5.2 tons of salt are required annually for the entire bridge deck. The production of this material results in about 7.9 tons of CO_2 emissions each year, which accumulate over time. In contrast, thermal de-icing systems generate emissions primarily once during their production phase.

6.2. Sensitivity of Outside Air Temperature Offsets

The figure shows a sensitivity analysis of different systems, plotted against outside air temperature offsets. Figure 6.1 presents the peak power coverage for the indirect systems at different bridge lengths, while Figure 6.2 shows the yearly energy coverage.

At a temperature offset of 0 °C, the coverage fraction represents the current performance of the systems, based on Amsterdam's 2024 weather data used in this report. If a system's curve crosses the black dashed line (coverage = 1) to the left of 0 °C, it means the system can still meet demand even at colder outside temperatures. If the intersection occurs to the right of 0 °C, the system only performs adequately under warmer conditions, specifically at the outside temperature where its curve crosses the black dashed line.

For the short bridge deck (Figure 6.1a) compared to the long bridge deck (Figure 6.1b), system 3 with heat pumps operates right at the current outside temperature, without requiring any offset. The glycol loop in this system, supported by the necessary heat pumps, is specifically designed to meet the bridge's de-icing demand.

In contrast, none of the configurations of system 1 or system 2 are able to meet the peak demand. Among these, the prefab foundation with U-loops extending to the second sand layer shows the largest offset in temperature increase needed. For this setup, the short deck only achieves full coverage for all indirect systems with a maximum outside temperature increase of about +4 °C, while the long deck requires a maximum increase of more than +5 °C.

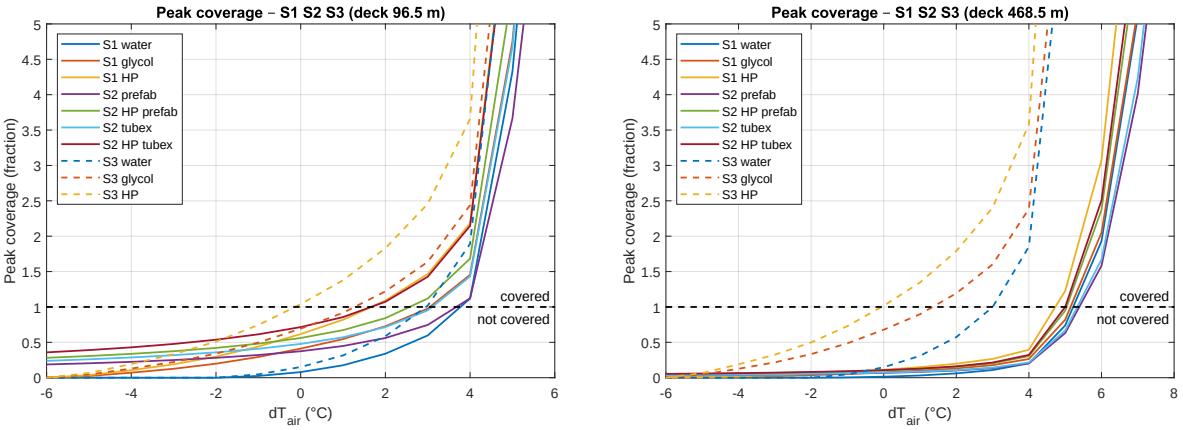

(a) Short deck length **(b)** Long deck length

Figure 6.1: Sensitivity analyses system 1-3: Power coverage vs. air temperature offsets

In Figure 6.2, the yearly energy coverage for the direct systems is shown. For the short deck (Figure 6.2a), only the water loop from system 1 falls short of covering the yearly energy demand. It requires about a +2 °C increase to meet the demand. For the long deck (Figure 6.2b), all configurations of system 3 can cover the yearly energy demand. Systems 1 and 2 each require an increase of around +4 °C to +5 °C to achieve full coverage.

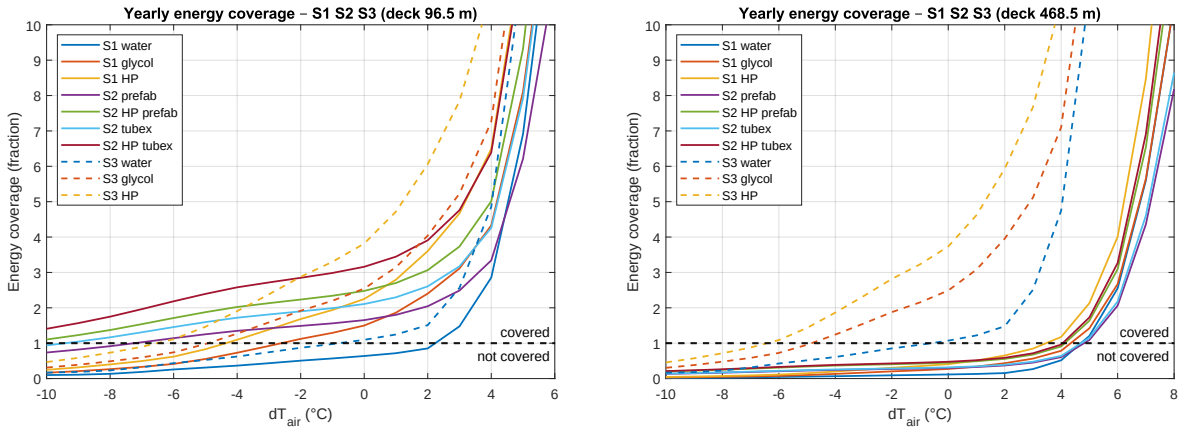

(a) Short deck length **(b)** Long deck length

Figure 6.2: Sensitivity analyses system 1-3: Energy coverage vs. air temperature offsets

The yearly energy coverage for system 4 and system 5, shown in Figure 6.3, indicates that both systems can handle decreases in outside air temperature. System 4 has a steeper slope than system 5. This means, when the temperature increases, system 4 achieves a higher coverage fraction than system 5. When the temperature decreases, however, system 4's coverage drops more quickly than system 5's. At their intersection point, both systems provide the same energy coverage fraction at that specific temperature offset.

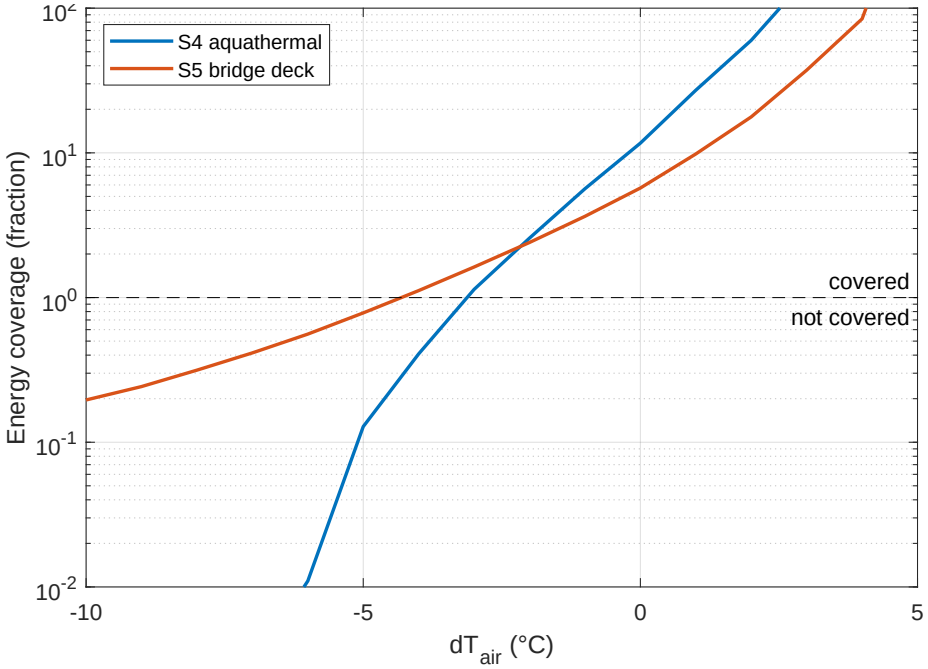

Figure 6.3: Sensitivity analyses system 4-5: Energy coverage vs. air temperature offsets

6.3. Trade-Off Analysis

While both indirect heating systems (4 and 5) cover the yearly energy demand, a trade-off analysis is made to show how flow rate design affects yearly energy coverage and ATES losses in Figure 6.4. Even when the summer recharge flow of the ATES system is reduced, both systems still meet the yearly energy demand. System 5 operates with one doublet per side of the river, using a warm well temperature of 21 °C and a larger temperature difference between the wells. In contrast, System 4 operates with two doublets, a warm well temperature of 17.5 °C, and smaller temperature differences. At the nominal summer flow rate on the heat exchanger side, which charges the warm well, the energy coverage fraction reaches about twelve for system 4 and about six for system 5. As already shown in Figure 6.3, the slope of system 4 is also steeper than that of system 5 in Figure 6.4.

ATES losses are determined by the ratio of screen length (set equal to aquifer thickness) to aquifer thermal radius (subsection 2.2.3). When this ratio roughly exceeds 2, tilting of the aquifer occurs due to buoyancy flow and dispersion. In Figure 6.4, system 4 shows higher energy coverage with lower ATES losses, while system 5 shows lower coverage with higher losses. For system 4, flow rate reductions of up to about 60 % can be reached before tilting occurs. For system 5, by contrast, the nominal flow rate must be increased to more than 140 % of the current flow rate to avoid tilting. With increasing flowrate of the system on the aquifer side, the volume of the aquifer affected by thermal exchange increases, while at lower flowrates the affected volume decreases.

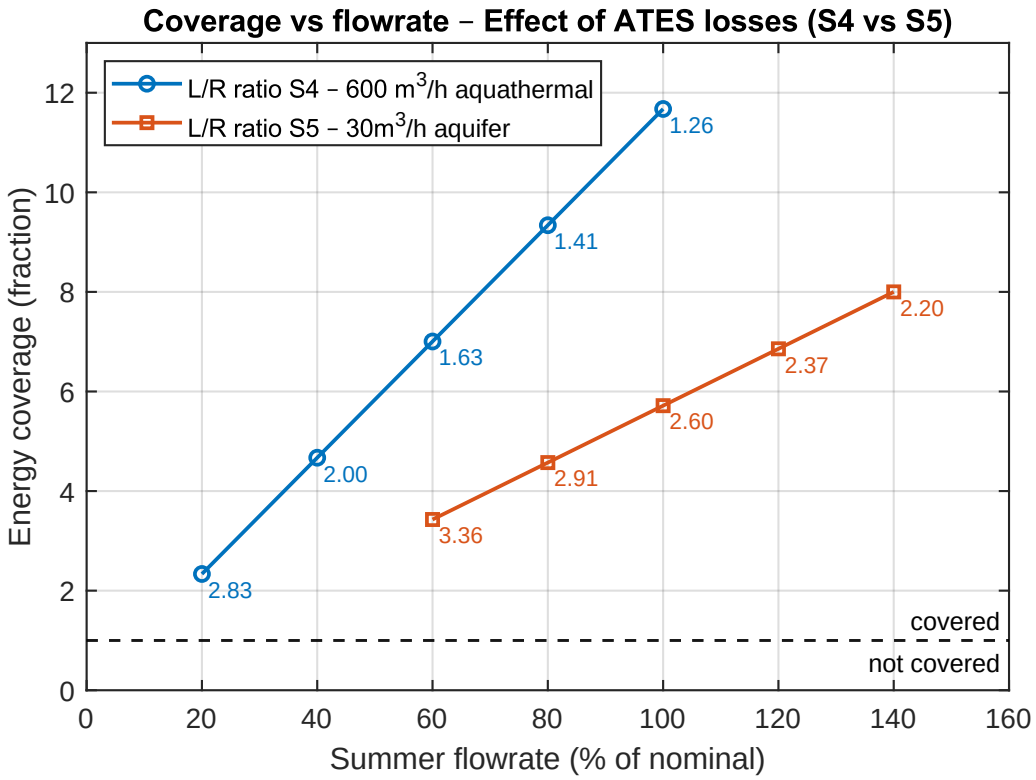

Figure 6.4: Trade-off analyses system 4-5: Energy coverage vs. summer flowrate and ATES losses

6.4. Identification of Optimal Systems

The cross-system assessment highlights clear differences between direct and indirect heating concepts. Among the direct systems, System 3 with heat pumps emerges as the only configuration capable of consistently meeting both annual and peak de-icing demand for short and long bridge decks. Its energy coverage performance is robust, but this comes at the expense of high electricity use and significant battery storage requirements, particularly for the long deck. In contrast to Systems 1 and 2, whose energy supply is constrained by pile configuration, System 3 is designed to meet the specified heat demand.

In contrast, the indirect ATES-based systems (Systems 4 and 5) provide substantial overcapacity, ensuring peak coverage and surplus annual energy. Between these, System 4 achieves higher energy coverage with an overcapacity of 2373 MWh annually and lower ATES losses. On the other hand, System 5 offers a simpler setup with an overcapacity of 1048 MWh annually, lower embodied CO2, and minimal battery requirements. The choice between these two therefore depends on whether minimizing embodied emissions and system complexity (favoring System 5) outweighs maximizing thermal performance (favoring System 4).

Overall, System 3 is optimal for smaller bridge sections where direct heating is preferable, while Systems 4 and 5 represent the most feasible long-term solutions for full-deck coverage due to their scalability, reliability under cold conditions, and strong energy balance.

7

Discussion

7.1. Summary of Key Results

The results indicate that, among direct-heating options (System 1-3), only the aquathermal configuration with glycol and heat pumps (System 3) achieves both annual and peak requirements for *both* deck lengths, whereas ATES-based systems (System 4-5) meet peak power for the full deck and provide substantial annual energy surpluses. Across all direct systems, performance varies systematically with loop fluid: glycol loops outperform water loops in both energy and peak coverage. Seasonal storage concepts confirm their effectiveness in addressing winter peaks, with ATES configurations achieving the highest peak coverage. The data further show that the electric balancing burden depends strongly on system concept: direct, heat-pump-dependent systems require significantly more battery capacity at full length due to aquathermal flow rates, while ATES options remain comparatively modest. Embodied CO2 scales with depth and material intensity, and is higher where open exchangers and additional hardware are required. However, this impact occurs only once during installation, whereas salt-based de-icing entails recurring annual emissions.

7.2. Interpretation of Key Results

The performance differences observed among system types can be explained by their thermodynamic and operational characteristics. In the direct systems, glycol loops sustain higher transferable power at low source temperatures and mitigate freezing risk, explaining their superior coverage relative to water loops. The direct aquathermal with heat pump design (System 3) clears the winter peak because its heat exchanger area and temperature lift were explicitly sized for the design hour, whereas the other direct concepts (Systems 1–2) are power-limited at peak even when annual energy suffices for the short deck. For storage-led concepts (Systems 4-5), the ability to shift summer heat to winter demand through ATES leverages higher source temperatures available in summer, thereby improving the system's robust energy performance

Where the sensitivity results appear counterintuitive, rising coverage in warmer climate conditions or sharp coverage loss in colder climate conditions, this is explained by the coverage definition: as temperature increases, demand drops faster than supply capacity, pushing the ratio up; at colder extremes, demand dominates and the ratio falls. Alternatively, the system's performance may be constrained by supply-side limits on maximum deliverable temperature difference, despite the potential for higher temperature lifts during warmer climate conditions.

7.3. Feasibility and Challenges

Energy-neutral operation of the Oostbrug appears feasible, provided design and operational conditions are carefully managed. Storage-led ATES systems offer the most stable solution by storing heat extracted during warmer summer conditions for use in winter. In contrast, direct heat pump systems remain more exposed to seasonal variability and higher electrical demand. The aquathermal concept

can technically meet both annual and peak loads but requires a large battery footprint, illustrating that thermal sufficiency alone does not guarantee overall feasibility. ATES designs entail higher embodied CO2 due to subsurface construction, yet this reflects durable infrastructure rather than recurring emissions.

Feasibility depends not only on the selected system type but also on how its design limitations are addressed. For direct systems, potential mitigations include hybridisation with small-scale seasonal storage; system 2 can be designed with solar recharging during summer in the energy piles. Furthermore for systems 1 and 2, implementing a spiral or W-shaped configuration in square prefabricated concrete piles would be technically challenging, as these shapes do not align well with the geometry of the pile. Such configurations are likely more suitable for round piles, which are typically steel Tubex piles. Therefore, when prefabricated concrete piles are used, it would be more feasible to apply U-shaped HDPE loops, while W-shaped or spiral designs would require the use of round steel piles.

Although this study did not explicitly analyse thermal interaction between adjacent energy piles (Systems 1 and 2), potential overlap of heat and cold influence zones could, in theory, reduce overall system capacity. However, because bridge de-icing involves short, intermittent heating periods rather than continuous building loads, this interaction is expected to be minimal. The energy is extracted and restored over relatively brief cycles, allowing sufficient recovery between events. Therefore, while spacing between piles should be considered in detailed design, thermal interference is unlikely to be a limiting factor for this application.

For aquathermal-led systems 3 and 4, challenges lie more in planning for embodied emissions and ensuring that recharge capacity is secured without conflict with the water ecological system. Across all systems, space for storage hardware and electrical containers is a practical constraint that must be addressed early through careful siting and layout design.

The renewable electricity mix is another determinant of feasibility. PV generation aligns well with daytime conditions but contributes little in winter, while wind power is more complementary during colder months. This complementarity partly reduces the electrical stress of heat-pump–based systems, although the long-deck configuration of System 3 still exceeds practical storage limits. Additional mitigation could come from operational controls that defer non-essential electrical use during peak cold hours.

A final consideration is methodological: the embodied CO2 estimates reflect only construction-phase impacts, and the performance metrics are based on a single meteorological year. These boundary conditions were intentionally chosen to maintain consistency in the assessment; however, they also limit generalization. Rather than undermining the analysis, acknowledging these constraints underscores where future work, such as multi-year weather data or broader life-cycle boundaries, could refine and validate the conclusions.

7.4. System Integration and Socio-Economic Fit

Integration with the city's infrastructure is strongest when systems ease winter pressure on the electricity grid and use existing utility corridors. ATES-based options fit particularly well with municipal climate goals, since they shift heat from summer to winter and require less visible above-ground equipment than heat-pump–based systems. Reliable operation also depends on coordinating construction and maintenance with bridge and waterway schedules, while simpler designs, such as shallower piles or less material-intensive exchangers, help reduce embodied CO2 and ease integration.

From a socio-economic perspective, the bridge could serve as a visible example of sustainable infrastructure, supporting public acceptance and building local expertise in aquathermal harvesting, ATES, and smart controls. Replacing salt spreading with thermal de-icing would further strengthen this value: in Amsterdam, bridges are salted roughly 30 times per winter, a practice that increases operational disruption, accelerates construction deterioration, and contributes to salination of the water bodies. Avoiding these operations reduces long-term maintenance costs, enhances safety, and eliminates a significant environmental burden.

Policy measures, such as subsidies for seasonal storage, incentives for on-site renewables, or embodied-carbon criteria in procurement, can directly address space constraints, high winter electricity demand,

and material intensity. Considering alternative wind turbine types, such as vertical-axis models suited to urban sites or low-noise horizontal-axis designs, could further improve spatial integration and align renewable generation more closely with seasonal demand. It should be noted that feasibility in terms of visual and spatial integration was assessed only for the PV panels, which are designed to cover the railing structure. For wind turbines, such considerations remain more uncertain due to their larger size and spatial requirements.

7.5. Robustness

Robustness refers to how well the systems perform under atypical years and long-term climate trends. It can be evaluated through the sensitivity analysis of outside air temperature offsets (Section 6.2) and the trade-off analysis of flow rate design in the ATES systems (Section 6.3). A system can be considered robust if its performance remains close to the design target under colder or warmer conditions (low sensitivity). Where performance depends strongly on climate variability, this sensitivity must be addressed in the design.

For the direct heating systems, the sensitivity analysis highlights a clear contrast in robustness. System 1 with heat pumps remains capable of meeting peak demand at current outside air conditions, making it the most resilient among the direct options. By comparison, Systems 1 and 1 are more sensitive to colder years, particularly on the long deck, where they would require design adjustments to achieve reliable performance. This behaviour can be explained by the role of the available temperature difference (ΔT). Systems that transfer heat with water, such as System 1, System 3, and System 4, show sharper declines in coverage as ΔT falls because their ability to deliver heat drops off quickly at low source temperatures. At higher ΔT, supply is constrained by design limits on maximum delivery temperature, so the decrease in demand (denominator) becomes the dominant factor shaping coverage.

For the indirect heating systems, both System 4 and System 5 maintain annual energy coverage even under colder conditions. System 4, however, shows a steeper response curve: it benefits more from warmer conditions but also loses performance more quickly as temperatures drop due to its dependency on the IJ river's temperature. System 5 is less efficient overall but more stable across offsets, which makes it the more robust option when accounting for long-term variability. The required heat gain depends not only on the outside air temperature but also on solar irradiation and the thermal capacity of the asphalt, followed by a concrete deck, which retains heat more effectively than water bodies, where heat dissipates more rapidly. Although both have a high heat capacity.

The trade-off analysis, however, offers a counterpoint to the sensitivity results. While System 5 appears more stable across temperature offsets, System 4 demonstrates greater robustness in terms of ATES performance. System 4 achieves higher nominal coverage and lower storage losses at its design flow rate, and it can tolerate significant flow-rate reductions before instability occurs. System 5, by contrast, requires higher flow rates to avoid losses, which makes its operation less flexible despite its flatter ambient air temperature sensitivity.

8

Conclusion

The aim of year-round self-sufficiency for the Oostbrug is achieved, provided that seasonal thermal storage is integral to the design for a robust system. Indirect, storage-based concepts ensure that both the annual energy balance and the critical winter peak demand can be met across the full deck length. Direct systems remain technically feasible for shorter spans or phased delivery. Still, at full scale their reliance on coincident renewable generation and exposure to cold-hour peaks make them fragile under uncertainty.

The hourly approach, combining KNMI 2024 data, modeled IJ water temperatures, and five system architectures, effectively generated decision-ready metrics, including peak and annual coverage, electrical deficits, electricity storage, and embodied CO2 impacts. This framework highlights both operational performance and heat-exchanging material trade-offs, showing that neutrality is attainable but not without compromises between technical feasibility, storage integration, and environmental footprint.

Systems 1 and 2 (direct pile-based energy) can provide adequate energy performance only for short decks, but they lack power for both short and long decks. Thus, they are not preferred for full-deck operation. For the short deck direct heating, most configurations require only modest ambient air temperature increases to cover peak demand. For the long deck for systems 1 and 2, significantly larger ambient air temperature lifts are needed. Thus, these systems may still be considered where construction simplicity is a primary concern, but their peak and energy coverage are partly met due to their limited pile configuration, and robustness remains limited.

Systems 3, 4 and 5, which integrate aquathermal or seasonal thermal storage, are more reliable and scalable solutions for energy-neutral operation. System 3 (direct aquathermal energy) is designed for the bridge demand and can deliver adequate service with low embodied construction emissions under present conditions for both deck lengths. Yet, their performance deteriorates under atypical winters. Additionally, full-deck operation results in greater electrical deficits. Thus, system 3 is not preferred for full-deck operation but is scalable for short-deck operation. By contrast, ATES-based configurations (systems 4 and 5) scale more effectively, smoothing variability by storing summer heat and ensuring reliable service even during prolonged cold periods, where adaptive flow-rate operation can further enhance their robustness for full-deck applications. System 4 (seasonal storage with aquathermal energy) has a maximum winter resilience through aquathermal heat recovery, but requires larger battery container footprints and more complex hydraulics. System 5 (seasonal storage with bridge deck energy) offers a strong balance between robustness in extreme weather conditions and reduced storage requirements, making it the preferred baseline for full-deck applications.

Reliable operation requires early allocation of solar and wind surfaces, container areas, and clear seasonal control strategies. While PV and small wind turbines can partly meet annual demand, seasonal storage remains essential for full balance. Systems 4 and 5 offer robust year-round autonomy, whereas System 3 provides a simpler alternative without heat storage. The quantified trade-offs highlight that selecting ATES is not merely an engineering choice but a commitment to resilient urban infrastructure in Amsterdam.

9

Recommendations

Future implementation of electrical and thermal de-icing systems for the Oostbrug should build on this study's findings by strengthening policy and financing frameworks, spatial and environmental coordination, and technical system optimization. Recommendations for achieving these goals are provided in this chapter.

For storage-led systems, policy support is crucial. Municipal or regional incentives for seasonal heat storage should be developed, recognizing the ability of ATES systems to reduce winter electricity demand peaks and support Amsterdam's carbon-neutrality objectives. At the same time, financing mechanisms should reflect life-cycle performance rather than initial investment alone. Given the one-time embodied CO_2 of ATES infrastructure, with the largest part occurring during the construction phase, compared with the recurring emissions from salt-based de-icing, circular or performance-based financing could reward up-front sustainable investment through carbon-linked procurement or green bond frameworks.

Early spatial coordination is essential to reserve sufficient bridge-adjacent areas for technical components such as battery containers, heat exchangers, and control units, particularly for Systems 3 and 4 with their larger storage and hydraulic layouts. Integrating these spaces into the bridge's civil design phase avoids later conflicts and supports modular, maintainable system architecture. For ATES applications, regulatory compliance must be secured through early coordination with water authorities to prevent interference with subsurface rights or ecological limits of the IJ river. Such engagement allows thermal recharge strategies to be adapted to environmental requirements while preserving efficiency. Visual and acoustic integration should also be considered, with low-noise, small-scale vertical-axis wind turbines offering a practical option for renewable electricity generation in dense urban contexts where spatial and aesthetic sensitivity is high.

In parallel, attention should be given to the design and selection of U-loop configurations within the energy piles of Systems 1 and 2. The performance of these loops is closely linked to pile geometry and construction type. For prefabricated concrete piles, U-shaped HDPE loops remain the most practical and robust option, whereas more complex geometries, such as W-shaped or spiral loops, are better suited to circular steel Tubex piles. Further investigation into the thermal efficiency, constructability, and mechanical compatibility of these loop shapes under local soil conditions would refine performance predictions and improve the integration of pile-based systems into the overall bridge foundation design. Whereas now, only an average number is picked for the clay and sand layers.

To ensure durability under future conditions, model validation should extend beyond the 2024 meteorological year to include multi-year historical and projected climate data. This will improve confidence in system robustness under varying cold extremes and long-term warming trends. Finally, integrating the bridge with Amsterdam's district heating network could enable mutual balancing between bridge storage and city infrastructure. Utilizing the ATES overcapacity in Systems 4 and 5 would enhance energy exchange, efficiency, and resilience, turning the bridge into an active element of the city's renewable energy system.

References

[1] Florida Department of Transportation (FDOT). *Bridge Maintenance Reference Manual*. en. URL: https://www.fdot.gov/maintenance/divisions.shtm/structures/bmrm.shtm (visited on 09/19/2025).

[2] AD. *3 bruggen, een voetgangerstunnel en nieuwe ponten: zo moet Amsterdam groei opvangen | Foto*. nl. URL: https://www.ad.nl/amsterdam/3-bruggen-een-voetgangerstunnel-en-nieuwe-ponten-zo-moet-amsterdam-groei-opvangen~a1e8f0aa/172467771/ (visited on 07/25/2025).

[3] Alfa Laval. *Maximum and operational pressure drop with plate heat exchangers*. Advanced Cooling Solutions. URL: https://www.acsolutions.pt/uploads/produtos/ficha_tecnica/max_and_operational_pressure_drop_with_gphes_1.pdf?utm.

[4] Gemeente Amsterdam. *Duurzame bronnen van warmtenetten*. nl. URL: https://www.amsterdam.nl/wonen-bouwen-verbouwen/duurzaam-amsterdam/aardgasvrij/alternatieven/duurzame-bronnen-warmtenetten/ (visited on 07/25/2025).

[5] Gemeente Amsterdam. *Onderzoeksboring naar aardwarmte op Strandeiland: stap richting duurzame warmte*. nl. Last Modified: 2025-06-24 Publisher: Gemeente Amsterdam. June 2025. URL: https://www.amsterdam.nl/wonen-bouwen-verbouwen/duurzaam-amsterdam/nieuws/onderzoeksboring-aardwarmte-strandeiland/ (visited on 07/25/2025).

[6] Ballyhoura Development CLG. *Aquathermal Energy 101: A Beginners Guide*. July 2024. URL: https://www.youtube.com/watch?v=D97wWvAw544 (visited on 08/28/2025).

[7] Stijn Beernink et al. "Heat losses in ATES systems: The impact of processes, storage geometry and temperature". en. In: *Geothermics* 117 (Feb. 2024), p. 102889. ISSN: 03756505. DOI: 10.1016/j.geothermics.2023.102889. URL: https://linkinghub.elsevier.com/retrieve/pii/S0375650523002444 (visited on 09/19/2025).

[8] Cableizer. *Thermal conductivity soil - Parameter*. URL: https://www.cableizer.com/documentation/k_4/ (visited on 07/30/2025).

[9] CarbonCloud. *Calcium chloride (CaCl2). E509 · 1.53 kg CO2e/kg*. URL: https://apps.carboncloud.com/climatehub/product-reports/id/146255465878?utm_source=chatgpt.com (visited on 10/25/2025).

[10] Shijing Chen et al. "A Review on the Technologies and Efficiency of Harvesting Energy from Pavements". en. In: *Energies* 18.15 (July 2025), p. 3959. ISSN: 1996-1073. DOI: 10.3390/en18153959. URL: https://www.mdpi.com/1996-1073/18/15/3959 (visited on 09/19/2025).

[11] Circular Ecology. *EN15804 Modules Explained*. en-US. URL: https://circularecology.com/en15804-modules-explained.html (visited on 09/20/2025).

[12] Communication BK. *Renovating Amsterdam's quay walls and tackling energy ambitions*. en. 2021. URL: https://www.tudelft.nl/en/2021/bk/renovating-amsterdams-quay-walls-and-tackling-energy-ambitions (visited on 07/29/2025).

[13] Vic A Cundy, John E Nydahl, and Kynric U Pell. "GEOTHERMAL HEATING OF BRIDGE DECKS". en. In: (). URL: https://onlinepubs.trb.org/Onlinepubs/sr/sr185/185-029.pdf.

[14] De Graaf et al. "Exploring the technical and economic feasibility of using the urban water system as a sustainable energy source". en. In: *Thermal Science* 12.4 (2008), pp. 35–50. ISSN: 0354-9836, 2334-7163. DOI: 10.2298/TSCI0804035d. URL: https://doiserbia.nb.rs/Article.aspx?ID=0354-98360804035d (visited on 07/30/2025).

[15] Dhr. H. de Jonge and Dhr. S. Verplak. *Bodemenergieplan Hamerkwartier Amsterdam*. Tech. rep. 68482/SV/20190702. July 2019.

[16] DINOloket. *Appelboor*. URL: https://www.dinoloket.nl/appelboor (visited on 10/23/2025).

[17] F. Dupray, C. Li, and L. Laloui. “Heat-exchanger piles for the de-icing of bridges”. en. In: *Acta Geotechnica* 9.3 (June 2014). Publisher: Springer Science and Business Media LLC, pp. 413–423. ISSN: 1861-1125, 1861-1133. DOI: 10.1007/s11440-014-0307-2. URL: http://link.springer.com/10.1007/s11440-014-0307-2 (visited on 07/24/2025).

[18] Eduard Enasel and Gheorghe Dumitrascu. “Storage solutions for renewable energy: A review”. en. In: *Energy Nexus* 17 (Mar. 2025), p. 100391. ISSN: 27724271. DOI: 10.1016/j.nexus.2025.100391. URL: https://linkinghub.elsevier.com/retrieve/pii/S2772427125000324 (visited on 09/20/2025).

[19] Energy Community Platform. *How aquathermal energy works*. en-US. URL: https://energycommunityplatform.eu/aquathermal-energy/how-aquathermal-energy-works/ (visited on 08/28/2025).

[20] M. van Engelen. *De stad: het verhaal van Amsterdam van 1980 tot vandaag*. Amsterdam: De Bezige Bij, 2024. ISBN: 978-94-031-6701-5.

[21] EnggCyclopedia. *Heat exchanger approach temperature*. en-US. May 2019. URL: https://enggcyclopedia.com/2019/05/heat-exchanger-approach-temperature/ (visited on 08/24/2025).

[22] European Steel Design Education Programme. *Lecture 1B.6.2: Introduction to the Design of Steel and Composite Bridges: Part 2*. URL: https://fgg-web.fgg.uni-lj.si/~/pmoze/esdep/master/wg01b/l0620.htm (visited on 10/20/2025).

[23] Ahmad Fakheri. “Efficiency analysis of heat exchangers and heat exchanger networks”. en. In: *International Journal of Heat and Mass Transfer* 76 (Sept. 2014), pp. 99–104. ISSN: 00179310. DOI: 10.1016/j.ijheatmasstransfer.2014.04.027. URL: https://linkinghub.elsevier.com/retrieve/pii/S0017931014003329 (visited on 08/20/2025).

[24] Omid Ghasemi Fare et al. *A Feasibility Study of Bridge Deck Deicing Using Geothermal Energy*. 2015. DOI: 10.13140/RG.2.2.30832.25607. URL: http://rgdoi.net/10.13140/RG.2.2.30832.25607 (visited on 07/31/2025).

[25] G. Filippini. *Warmteoverdracht frequentietabel*. Excel-bestand met ruwe data. July 2025.

[26] Anton de Fockert and Valesca Harezlak. “Ontwerphandreiking Aquathermie-TEO (versie 2)”. nl. In: *Deltares* WarmingUp werkpakket 3C (2022), p. 68. URL: https://www.warmingup.info/documenten/2022_ontwerphandreiking-aquathermie-teo.pdf.

[27] Anton de Fockert et al. “Aquathermie configuraties”. nl. In: *Deltares* Overzicht TEO, TED en TEA door middel van factsheets, kostenkentallen en beslisbomen (May 2021), p. 88. URL: https://www.deltares.nl/expertise/publicaties/aquathermie-configuraties-overzicht-teo-ted-en-tea-door-middel-van-factsheets-kostenkentallen-en-beslisbomen.

[28] M.A. Fremouw. “MUSIC: GIS based EPM and residual heat potential”. English. 2012. URL: http://resolver.tudelft.nl/uuid:93f640ee-fcb9-4467-b9aa-c9ac46ec7d4c (visited on 08/20/2025).

[29] Jun Gao et al. “Numerical and experimental assessment of thermal performance of vertical energy piles: An application”. en. In: *Applied Energy* 85.10 (Oct. 2008), pp. 901–910. ISSN: 03062619. DOI: 10.1016/j.apenergy.2008.02.010. URL: https://linkinghub.elsevier.com/retrieve/pii/S0306261908000342 (visited on 08/01/2025).

[30] Shipeng Gao, Yongxin Yang, and Zhimin Chai. *Evaluation of Bridge-Integrated Wind Turbine System: A Hybrid Wind-Induced Vibration Control and Wind Energy Harvesting Strategy*. 2024. DOI: 10.2139/ssrn.5068968. URL: https://www.ssrn.com/abstract=5068968 (visited on 09/19/2025).

[31] Gemeente Amsterdam. *WG-terrein aardgasvrij*. nl. webpagina. Last Modified: 2025-07-29. URL: https://www.amsterdam.nl/wonen-bouwen-verbouwen/duurzaam-amsterdam/aardgasvrij/aardgasvrije-buurten/wg-terrein-aardgasvrij/ (visited on 07/29/2025).

[32] Peng Guo et al. “Mutually reinforcing performance of energy harvest and wind environment via wind turbine-solar integrated system over a bridge”. en. In: *Energy* 328 (Aug. 2025), p. 136588. ISSN: 03605442. DOI: 10.1016/j.energy.2025.136588. URL: https://linkinghub.elsevier.com/retrieve/pii/S0360544225022303 (visited on 09/19/2025).

[33] Chanjuan Han and Xiong (Bill) Yu. “Feasibility of geothermal heat exchanger pile-based bridge deck snow melting system: A simulation based analysis”. en. In: *Renewable Energy* 101 (Feb. 2017), pp. 214–224. ISSN: 09601481. DOI: 10.1016/j.renene.2016.08.062. URL: https://linkinghub.elsevier.com/retrieve/pii/S0960148116307728 (visited on 08/01/2025).

[34] Royal Haskoning. *Draft SO Phase II Report*. Tech. rep. Confidential internal report. Gemeente Amsterdam, July 2025.

[35] K. Heinloth, ed. *Renewable Energy*. en. Vol. 3C. Landolt-Börnstein - Group VIII Advanced Materials and Technologies. Springer Berlin Heidelberg, 2006. ISBN: 978-3-540-42962-3. DOI: 10.1007/b83039. URL: http://materials.springer.com/bp/docs/978-3-540-45662-9 (visited on 10/16/2025).

[36] Hosung Song et al. “Wind energy harvesting at elevated bridges”. en. In: *The Seventh International Colloquium on Bluff Body Aerodynamics and Applications (BBAA7)* (Sept. 2012), p. 10. URL: https://iawe.org/Proceedings/BBAA7/H.Song.pdf (visited on 09/19/2025).

[37] ir. J.K. Haasnoot. *Amsterdamse Kademuur als Energiefabriek*. nl. Tech. rep. RA20241a3. CRUX, 2021, p. 42.

[38] Saqib Javed and Jeffrey D. Spitler. “Vertical ground heat exchanger pressure loss – Experimental comparisons and calculation procedures”. en. In: *Geothermics* 105 (Nov. 2022), p. 102546. ISSN: 03756505. DOI: 10.1016/j.geothermics.2022.102546. URL: https://linkinghub.elsevier.com/retrieve/pii/S0375650522001924 (visited on 10/25/2025).

[39] A Kleyböcker and M Bloemendal. “Factsheet – Aquifer thermal energy storage (ATES)”. en. In: (2020). URL: https://mp.watereurope.eu/media/factsheets/Factsheet_ATES_V5_ypLKKy4.pdf.

[40] Piotr Klimaszewski et al. “Design and performance analysis of ORC centrifugal pumps”. pl. In: *Archives of Thermodynamics* (Dec. 2020), pp. 203–222. ISSN: 1231-0956, 2083-6023. DOI: 10.24425/ather.2020.135860. URL: https://journals.pan.pl/dlibra/publication/135860/edition/118782/content (visited on 10/25/2025).

[41] KNMI. *Uurgegevens van het weer in Nederland*. 2025. URL: https://www.knmi.nl/nederland-nu/klimatologie/uurgegevens (visited on 07/29/2025).

[42] S.-D. Kwon, S.-H. Lee, and H.K. Lee. “Aerodynamic Performance of Bridges Equipped Small Wind Turbines”. en. In: *Dynamics of Bridges, Volume 5*. 1st ed. New York: River Publishers, Aug. 2025, pp. 85–92. ISBN: 978-87-438-0208-2. DOI: 10.1007/978-1-4419-9825-5_9. URL: https://www.taylorfrancis.com/books/9788743802082/chapters/10.1007/978-1-4419-9825-5_9 (visited on 09/20/2025).

[43] Weidong Lyu et al. “Numerical Study on Optimal Scheme of the Geothermally Heated Bridge Deck System”. en. In: *Energies* 13.24 (Dec. 2020), p. 6633. ISSN: 1996-1073. DOI: 10.3390/en13246633. URL: https://www.mdpi.com/1996-1073/13/24/6633 (visited on 07/31/2025).

[44] M. van Meerkerk. *Warmtewisselaars voor aquathermie : warmteoverdracht en benodigde filtering | Deltares*. nl. Jan. 2022. URL: https://www.deltares.nl/expertise/publicaties/warmtewisselaars-voor-aquathermie-warmteoverdracht-en-benodigde-filtering (visited on 08/25/2025).

[45] Wenting Ma, Moon Keun Kim, and Jianli Hao. “Numerical Simulation Modeling of a GSHP and WSHP System for an Office Building in the Hot Summer and Cold Winter Region of China: A Case Study in Suzhou”. en. In: *Sustainability* 11.12 (June 2019), p. 3282. ISSN: 2071-1050. DOI: 10.3390/su11123282. URL: https://www.mdpi.com/2071-1050/11/12/3282 (visited on 09/20/2025).

[46] Khristina Maksudovna Vafaeva and P. Sanjeeva. “Comparative analysis of lithium-ion and flow batteries for advanced energy storage technologies”. In: *MATEC Web of Conferences* 392 (2024). Ed. by K. Satyanarayana et al., p. 01176. ISSN: 2261-236X. DOI: 10.1051/matecconf/202439201176. URL: https://www.matec-conferences.org/10.1051/matecconf/202439201176 (visited on 09/20/2025).

[47] Anthony F. Mills. *Basic heat and mass transfer*. eng. 2nd ed. Upper Saddler River, NJ: Prentice Hall, 1999. ISBN: 978-0-13-096247-8.

[48] L. D. Minsk, United States. Federal Highway Administration. Office of Technology Applications, and United States. Federal Highway Administration. Office of Engineering. *Heated Bridge Technology - Report on ISTEA Sec. 6005 Program*. English. Tech. rep. FHWA-RD-99-158. July 1999. URL: /view/dot/40560 (visited on 08/13/2025).

[49] D.J. Molenaar. "Oppervlaktewater, een verbetering bij warmtepompsystemen met warmte-/koudeopslag?" nl. PhD thesis. TU Eindhoven, Aug. 2011. URL: https://research.tue.nl/nl/studentTheses/oppervlaktewater-een-verbetering-bij-warmtepompsystemen-met-warmt (visited on 07/29/2025).

[50] MPINarada. *Energy Storage - NESP (LFP) Liquid Cooling Container Solutions*. en-US. 2020. URL: https://mpinarada.com/container-rack-solutions/ (visited on 09/14/2025).

[51] Narada Power. *Technological innovation*. URL: https://en.naradapower.com/ (visited on 09/20/2025).

[52] NL Times. *Nederland nu veilig tegen zeespiegelstijging; verzilting urgenter probleem*. nl. Nov. 2023. URL: https://nltimes.nl/2023/11/09/netherlands-currently-safe-rising-sea-levels-salinization-urgent-problem (visited on 10/14/2025).

[53] openresearch.amsterdam. *Potentieonderzoek geothermie Noord-Holland en Flevoland*. nl. May 2023. URL: https://openresearch.amsterdam/nl/page/92984/potentieonderzoek-geothermie-noord-holland-en-flevoland (visited on 07/25/2025).

[54] Jong-Woong Park et al. "Feasibility Study of Micro-Wind Turbines for Powering Wireless Sensors on a Cable-Stayed Bridge". en. In: *Energies* 5.9 (Sept. 2012), pp. 3450–3464. ISSN: 1996-1073. DOI: 10.3390/en5093450. URL: https://www.mdpi.com/1996-1073/5/9/3450 (visited on 09/20/2025).

[55] Yaoyao Pei et al. "Experimental research on power generation performance of under-bridge photovoltaic structure". en. In: *Renewable Energy* 240 (Feb. 2025), p. 122253. ISSN: 09601481. DOI: 10.1016/j.renene.2024.122253. URL: https://linkinghub.elsevier.com/retrieve/pii/S0960148124023218 (visited on 09/19/2025).

[56] Provincie Noord-Holland. *Over het project*. nl-NL. Last Modified: 2025-06-27. Aug. 2024. URL: https://www.noord-holland.nl/Onderwerpen/Verkeer_vervoer/Projecten_Verkeer_en_Vervoer/Cruquiusbrug/Over_het_project (visited on 07/29/2025).

[57] David Reber, Sam R. Jarvis, and Michael P. Marshak. "Beyond energy density: flow battery design driven by safety and location". en. In: *Energy Advances* 2.9 (2023), pp. 1357–1365. ISSN: 2753-1457. DOI: 10.1039/D3YA00208J. URL: https://xlink.rsc.org/?DOI=D3YA00208J (visited on 09/20/2025).

[58] Noord-Hollandse energie regio. *Draft RES Amsterdam*. Tech. rep. 2020, pp. 1–29.

[59] M. Revels. *How One Texas Bridge Stayed Ice-Free During Arctic Blast*. en. 2024. URL: https://engineering.tamu.edu/news/2024/03/how-one-texas-bridge-stayed-ice-free-during-arctic-blast.html (visited on 07/29/2025).

[60] D. Salciarini, A. Lupattelli, and G. Capati. "Exploring the Potential of Energy Geostructures for Road and Bridge Pavement Heating and Cooling". eng. In: *ISSMGE* (July 2022). DOI: 10.53243/ACPMG2024-17. URL: https://doi.org/10.53243/ACPMG2024-17 (visited on 07/25/2025).

[61] SeaTemperature.org. *Amsterdam Water Temperature | Netherlands*. en. URL: https://www.seatemperature.org/europe/netherlands/amsterdam.htm (visited on 07/30/2025).

[62] Laura Soares and Hao Wang. "Sustainability impact of photovoltaic noise barriers with different design configurations". en. In: *Transportation Research Part D: Transport and Environment* 116 (Mar. 2023), p. 103624. ISSN: 13619209. DOI: 10.1016/j.trd.2023.103624. URL: https://linkinghub.elsevier.com/retrieve/pii/S1361920923000214 (visited on 09/19/2025).

[63] J. D. Spitler and M. Ramamoorthy. "Bridge Deck Deicing using Geothermal Heat Pumps". In: *Oklahoma State University Stillwater, OK, U.S.A.* (). URL: https://citeseerx.ist.psu.edu/document?repid=rep1&type=pdf&doi=080652a5bd4ffe052e1c233edff0f46d9bb00c38.

[64] Nationale staalprijs. *Fiets- en voetgangersbrug Lille Langebro*. nl. URL: https://www.nationalestaalprijs.nl/project/fiets-en-voetgangersbrug-lille-langebro (visited on 07/25/2025).

[65] Ruben Stemmle et al. “Environmental impacts of aquifer thermal energy storage (ATES)”. en. In: *Renewable and Sustainable Energy Reviews* 151 (Nov. 2021), p. 111560. ISSN: 13640321. DOI: 10.1016/j.rser.2021.111560. URL: https://linkinghub.elsevier.com/retrieve/pii/S1364032121008388 (visited on 09/10/2025).

[66] Lettow Studios. *asphalt collector*. en-US. URL: https://www.cyclifier.org/project/asphalt-collector/ (visited on 09/14/2025).

[67] Bradley J. Taylor. “Fiber-Reinforced Polymer Honeycomb Bridge Deck Heating Evaluation”. en. PhD thesis. University of Toledo, 2009. URL: https://etd.ohiolink.edu/acprod/odb_etd/r/etd/search/10?clear=10&p10_accession_num=toledo1260205596&session=115548043314028&utm_source=chatgpt.com (visited on 10/25/2025).

[68] TRANE technologies. *City™ RTSF Water-to-Water Heat Pump*. URL: https://trane.eu/uk/equipment/product-details.html?prodId=222 (visited on 10/29/2025).

[69] TU Delft. *Topic 8: Hydroelectricity and Wind Energy - SET3014 Renewable Energy (2024/25 Q1)*. Lecture PowerPoint Slides. URL: https://brightspace.tudelft.nl/d2l/le/content/683517/Home (visited on 07/29/2025).

[70] TU Delft. *Topic 9: Solar Energy and Biomass - SET3014 Renewable Energy (2024/25 Q1)*. Lecture PowerPoint Slides. URL: https://brightspace.tudelft.nl/d2l/le/content/683517/Home (visited on 07/29/2025).

[71] Christopher Tuan and Sherif Yehia. “Implementation of Conductive Concrete Overlay for Bridge Deck Deicing at Roca, Nebraska”. In: *Civil Engineering Faculty Proceedings & Presentations* (June 2004). URL: https://digitalcommons.unomaha.edu/civilengfacproc/3.

[72] Vattenfall. *Vattenfall aan de slag voor Amsterdamse warmte*. nl. 2019. URL: https://group.vattenfall.com/nl/newsroom/persbericht/2019/vattenfall-aan-de-slag-voor-amsterdamse-warmte (visited on 07/25/2025).

[73] Whole Building Design Guide. *Geothermal Heat Pumps*. URL: https://www.wbdg.org/resources/geothermal-heat-pumps?utm_source=chatgpt.com (visited on 09/20/2025).

[74] Di Wu et al. “Performance of a bridge deck as solar collector in a thermal energy storage system”. In: *E3S Web of Conferences* 205 (2020). Ed. by J.S. McCartney and I. Tomac, p. 07009. ISSN: 2267-1242. DOI: 10.1051/e3sconf/202020507009. URL: https://www.e3s-conferences.org/10.1051/e3sconf/202020507009 (visited on 08/22/2025).

[75] Sherif Yehia and Christopher Tuan. “Bridge Deck Deicing”. In: *Civil Engineering Faculty Proceedings & Presentations* (Aug. 1998), p. 8. URL: https://digitalcommons.unomaha.edu/civilengfacproc/1.

[76] Xinbao Yu. “Use of Geothermal Energy for De-Icing Approach Pavement Slabs and Bridge Decks – Phase II”. en. In: (2024). URL: https://library.ctr.utexas.edu/hostedpdfs/uta/0-6872-01-1.pdf.

[77] Muhammad Zeeshan. *Bascule Bridge Definition in Construction in the Netherlands*. en-US. Section: Blogs. Mar. 2025. URL: https://alsyedconstruction.com/bascule-bridge-definition-in-construction-in-the-netherlands/ (visited on 09/19/2025).

[78] Peng Zhang et al. “Holistic Design of Energy Pile Bridge Deicing System With Ontology-Based Multiobjective Decision Making”. In: *Frontiers in Materials* 8 (Aug. 2021), p. 710404. ISSN: 2296-8016. DOI: 10.3389/fmats.2021.710404. URL: https://www.frontiersin.org/articles/10.3389/fmats.2021.710404/full (visited on 08/22/2025).

A

Amsterdam's District Heating Network

Amsterdam's district heating network already demonstrates a strong foundation for large-scale sustainable energy integration. This refers to the coordinated use of renewable energy sources, such as geothermal heat and waste heat recovery, which distributes this centrally generated heat to buildings for space heating and hot water. Currently, several parts of the city are supplied by district heating networks [72], as shown in Figure A.1. The southeastern network, marked in red, is powered by Vattenfall's Diemen power station, which serves the Amstelland sub-region [58]. In contrast, the northwestern area, shown in orange, relies on the Westpoort Heat network, primarily sourcing its heat from the Afval Energie Bedrijf (AEB). The blue section indicates a newly developed heating pipeline and an auxiliary heating plant (HWC), reflecting the city's continued expansion of its heat distribution capacity.

Beyond these existing systems, geothermal and aquathermal energy are being explored as potential additions to the city's renewable heat portfolio. Ongoing research in Strandeiland (Figure A.1) is assessing the geothermal potential in the range of 2.5–8 MW_t [53, 5]. Moreover, residual heat from data centers and wastewater streams offers further opportunities to diversify and decarbonize urban heat sources [4]. Together, these developments illustrate Amsterdam's broader commitment to transitioning toward a resilient and low-carbon heat network.

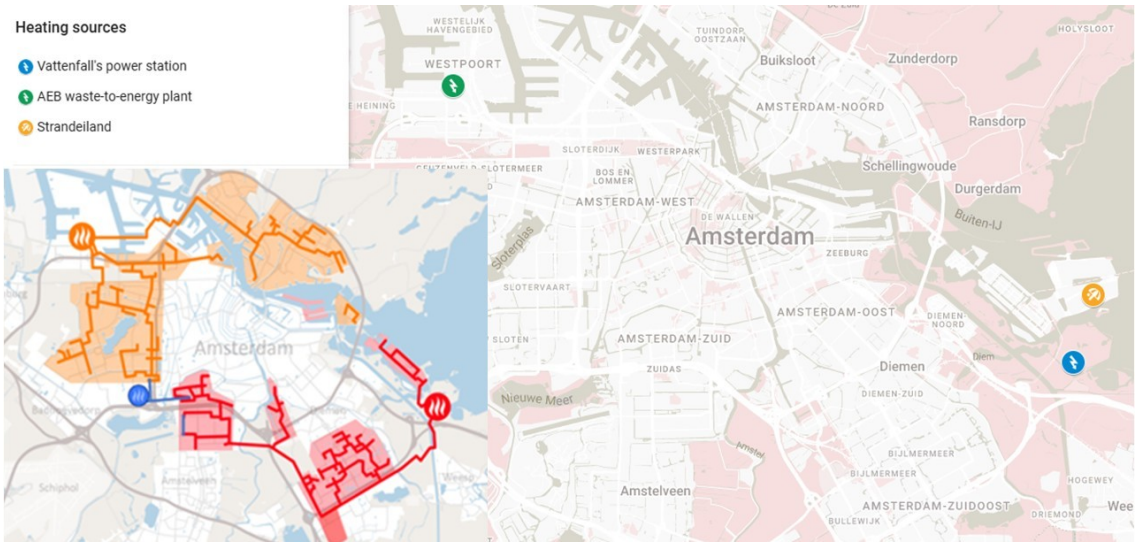

Figure A.1: Amsterdam district heating network (left) [72] and power stations (right)

B

Fiber-Reinforced Polymer Honeycomb (FRPH)

Figure B.1 shows the composition of the fiber-reinforced polymer honeycomb (FRPH) deck. In Figure B.1a, the FRPH core with triangular cells and a polymer-concrete top layer is shown in cross-section, illustrating the internal honeycomb structure and the bonding flange between layers. In Figure B.1b, a close-up of the interface between the polymer-concrete layer and the FRPH flange is presented, highlighting the connection and surface texture at the joint.

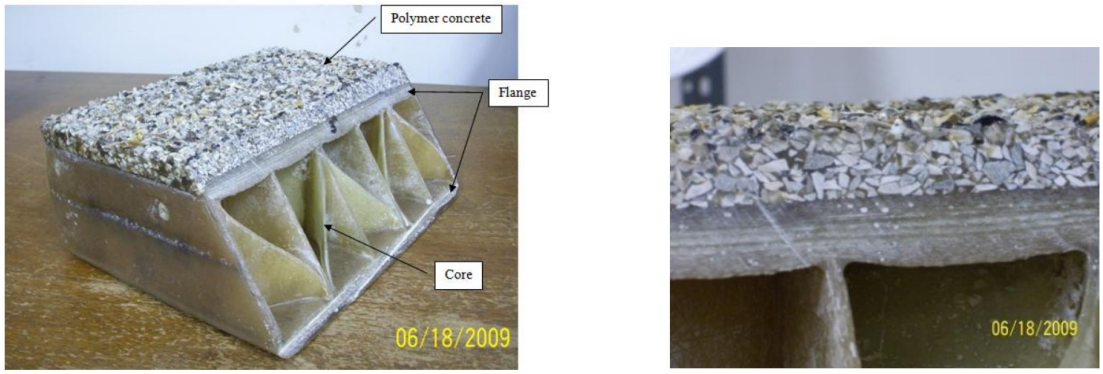

(a) FRPH core with polymer concrete top layer cross-section

(b) Interface flange with polymer concrete

Figure B.1: FRPH composition structures [67]

C

Annual Heat Demand of Bridge Deck Sections

Figure C.1 shows the heat demand for a 96.5-meter bridge section. The heating requirement peaks during the winter months, with the highest demand occurring in January, reaching instantaneous values of almost 250 kW. This reflects periods of freezing conditions when the bridge surface must be heated to prevent icing. The demand remains negligible throughout spring and summer, indicating limited or no heating operation during warmer periods. A smaller secondary peak appears in late autumn (November–December), corresponding to the onset of lower ambient temperatures. The total annual heat demand for this bridge length is approximately 17.9 MWh.

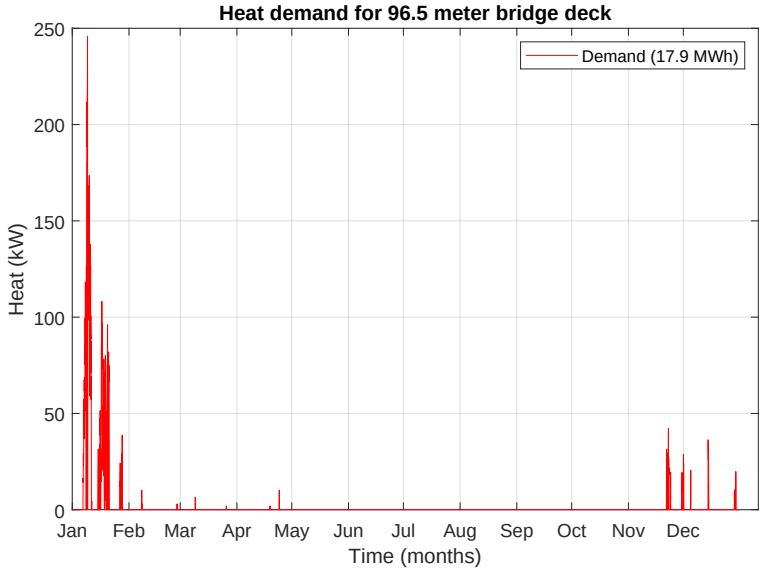

Figure C.1: Annual heat demand for 96.5 meters deck

Figure C.2 displays results for a 468.5-meter section. Similar to the shorter deck, the demand is concentrated in the winter months, with the highest peaks in January reaching values of 1,200 kW. These sharp peaks correspond to intensive de-icing requirements during the coldest periods. Minimal demand is observed from March through October, when ambient temperatures remain above freezing. A smaller increase in demand appears in November and December as temperatures begin to drop again. The total annual heat demand for this longer bridge section is approximately 86.8 MWh, reflecting the greater surface area and thermal load compared to the 96.5-meter section.

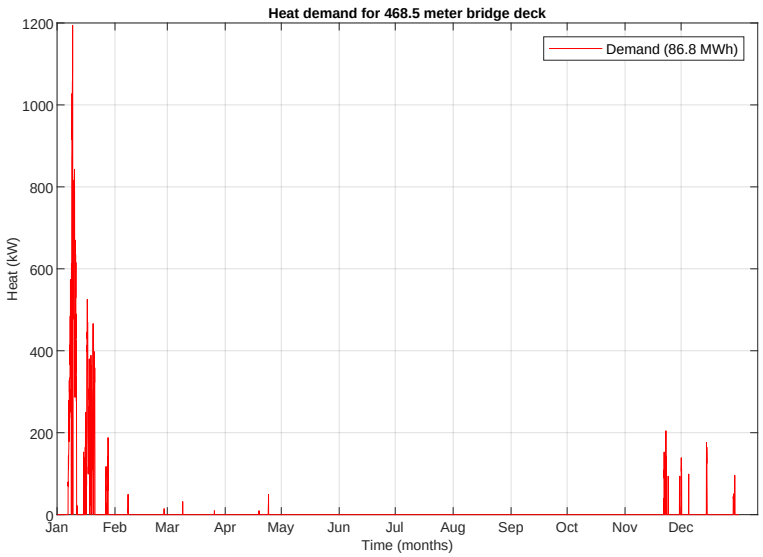

Figure C.2: Annual heat demand for 468.5 meters deck

Figure C.3 illustrates the combined annual heat demand for the entire bridge length. The demand pattern mirrors that of the shorter sections, with the highest heating requirement occurring during January, reaching instantaneous values exceeding 3,000 kW. This peak corresponds to the most severe winter conditions, when continuous surface heating is required to prevent ice formation. Virtually no heating is needed between March and October, reflecting periods of favorable ambient temperatures. A smaller increase in demand appears again in late autumn. The total annual energy demand for the entire bridge deck amounts to approximately 222.3 MWh, demonstrating the proportional scaling of energy requirements with bridge length.

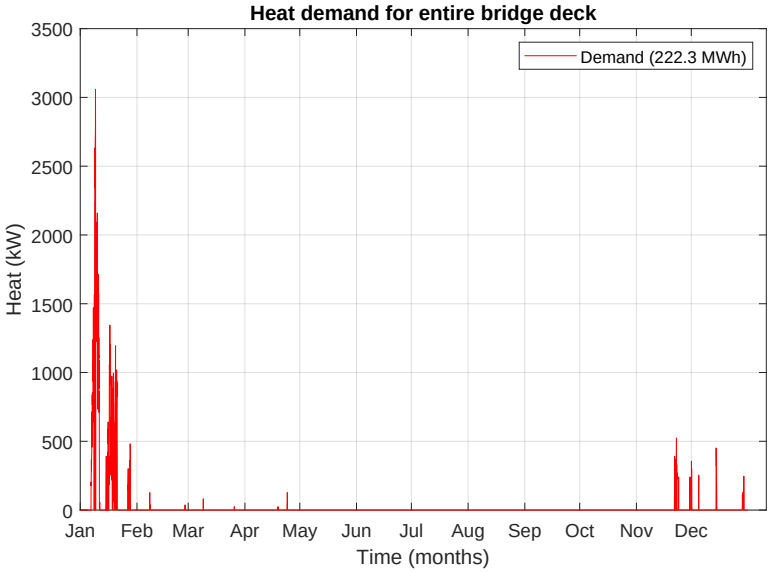

Figure C.3: Annual heat demand for entire bridge length

D

Heat Flux Equations

Atmospheric and Saturation Vapour Pressure

Equations D.1 and D.2 define the atmospheric vapour pressure based on air temperature and the saturation vapour pressure as a function of water temperature. These parameters describe the moisture content in air and at the water surface, which influence evaporation and heat exchange processes.

$$P_{[a]} = 6.112 * 10^{(7.5*T_{air})/(273.7+T_{air})} \tag{D.1}$$

$$P_{[s]} = 23.4 * 1.062^{(T_{water}-20)} \tag{D.2}$$

Wind and Emission Parameters

Equations D.3 and D.4 represent the empirical wind function and the surface emissivity factor. The wind function relates heat transfer intensity to wind speed, while the emissivity accounts for radiative properties depending on cloud cover and vapour pressure.

$$f(\nu_{wind}) = 3.68 + 2.65 * \nu_{wind} \tag{D.3}$$

$$\varepsilon = 0.74 * (1 + 0.17(C_c) + 0.045(1 - (C_c)) * P_a \tag{D.4}$$

Heat Fluxes

The heat flux components in Equations D.5–D.9 represent the main energy exchanges at the water surface. These include atmospheric radiation ($H_{[a]}$), back radiation ($H_{[l]}$), evaporative heat flux (H_e), convective heat flux (H_c), and conductive heat transfer from the ground (H_{ground}). Together, these terms define the overall thermal balance of the system.

$$H_{[a]} = \varepsilon * \sigma_{SB} * (T_{air} + 273)^4 \tag{D.5}$$

$$H_{[l]} = -\varepsilon * \sigma_{SB} * (T_{water} + 273)^4 \tag{D.6}$$

$$H_e = -f(\nu_{wind}) * (P_s - P_a) \tag{D.7}$$

$$H_c = (2.02 + 1.46 * f(\nu_{wind})) * (T_{air} - T_{water}) \tag{D.8}$$

$$H_{ground} = (k_{mud}/depth) * (T_{ground} - T_{water}) \tag{D.9}$$

E

Subsurface KNSM-eiland and Hamerkwartier

Subsurface Characteristics

Figures E.1 and E.2 illustrate the geological composition and hydrological properties of the subsurface at the study sites. Figure E.1 shows the subsurface profile at KNSM-eiland based on BRO REGIS II data, indicating a total depth of 110 m and an aquifer thickness (H) of 50 m, with a horizontal hydraulic conductivity (K_h) of 50 m/d and a vertical hydraulic diffusivity (K_d) of 1000 m^2/d. The highlighted zone marks the main water-bearing layer suitable for thermal energy storage applications in this report.

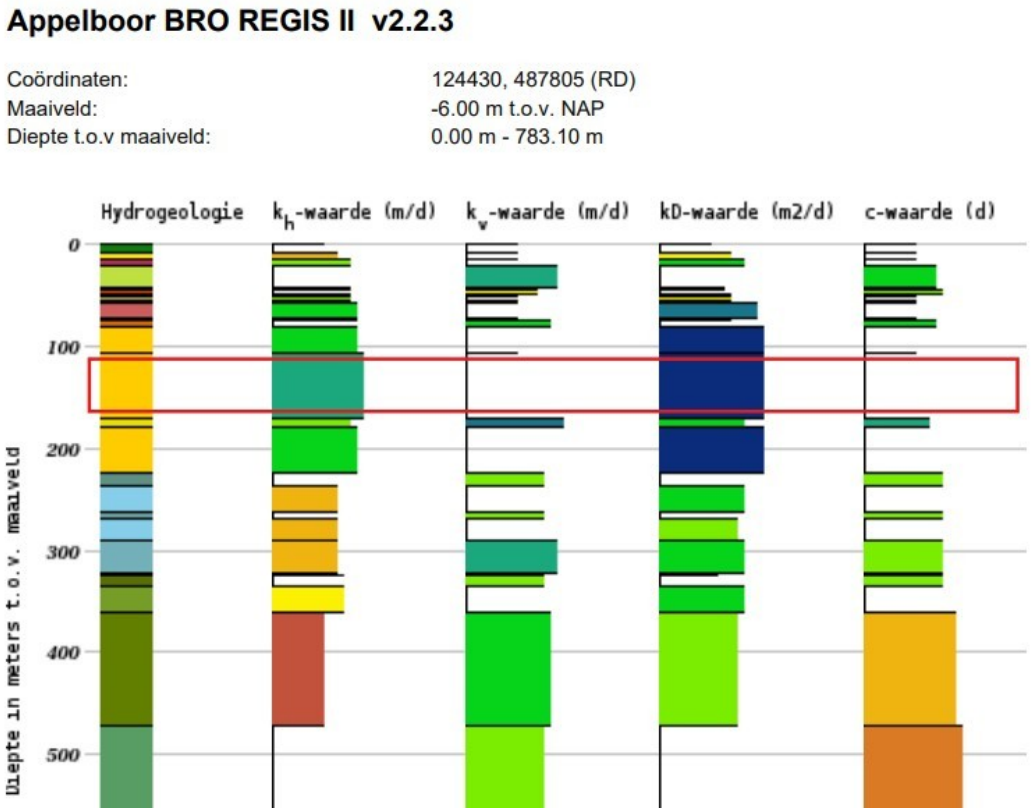

Figure E.1: Subsurface KNSM-eiland with depth 110 m, H = 50 m, Kh = 50 m/d, Kd = 1000 m²/d [16]

Figure E.2 presents the layered subsurface at Hamerkwartier, approximately 1 m above NAP, showing alternating layers of clay, sand, and peat. The identified sand layers form potential zones for aquifer thermal energy storage (ATES) integration.

diepte [m-mv]*	lithologie	geohydrologische benaming
0 - 15	klei en fijn zand	deklaag
15 - 35	matig fijn tot zeer grof zand, mogelijk met kleilaagjes	1e watervoerend pakket
35 - 65	klei, zand en veensporen	2e scheidende laag
65 - 100	matig fijn tot matig grof zand met kleilagen	2e/3e watervoerende pakket
100 - 190	matig grof tot zeer grof zand met enkele kleilagen	2e/3e watervoerende pakket
190 - 230	fijn tot matig fijn zand	2e/3e watervoerende pakket
> 230	klei en fijn zand	hydrologische basis

Figure E.2: Layered subsurface at Hamerkwartier at ≈ 1 m + NAP [15]